

# Cobalt oxide catalysts for the total oxidation of propane

Rebecca Kate Pinnell

Thesis submitted in accordance with the requirements  
for the degree of Doctor of Philosophy

November 2014

Cardiff University  
School of Chemistry

## Declaration

This work has not been submitted in substance for any other degree or award at this or any other university or place of learning, nor is being submitted concurrently in candidature for any degree or other award.

Signed ..... (candidate)      Date .....

### STATEMENT 1

This thesis is being submitted in partial fulfilment of the requirements for the degree of PhD.

Signed ..... (candidate)      Date .....

### STATEMENT 2

This thesis is the result of my own independent work/investigation, except where otherwise stated.

Other sources are acknowledged by explicit references. The views expressed are my own.

Signed ..... (candidate)      Date .....

### STATEMENT 3

I hereby give consent for my thesis, if accepted, to be available online in the University's Open Access repository and for inter-library loan, and for the title and summary to be made available to outside organisations.

Signed ..... (candidate)      Date .....

### STATEMENT 4: PREVIOUSLY APPROVED BAR ON ACCESS

I hereby give consent for my thesis, if accepted, to be available online in the University's Open Access repository and for inter-library loans **after expiry of a bar on access previously approved by the Academic Standards & Quality Committee.**

Signed ..... (candidate)      Date .....

## Abstract

The three-way catalyst (TWC) greatly reduces emissions of hydrocarbons, carbon monoxide and nitrogen oxides from gasoline powered vehicles. However up to 80% of all hydrocarbons are emitted in the first 120 seconds after the engine is started, before the TWC achieves light-off. Catalysts which are active at lower temperatures offer a potential solution to this 'cold-start' problem.

$\text{Co}_3\text{O}_4$  is one of the most active transition metal oxide catalysts for the total oxidation of hydrocarbons. In this work the synthesis of bulk and supported cobalt oxide catalysts has been investigated. The catalysts were thoroughly characterised and tested for the total oxidation of propane, a model hydrocarbon.

Variables in the mechanochemical synthesis and precipitation of bulk  $\text{Co}_3\text{O}_4$  were studied. Cobalt hydroxycarbonate hydrate synthesised by both techniques was found to give rise to active and stable  $\text{Co}_3\text{O}_4$  catalysts upon calcination. Small  $\text{Co}_3\text{O}_4$  crystallites, high surface areas, weak  $\text{Co}^{3+}$ -O bonds, and the absence of contaminants were found to be required for high propane oxidation activity.

Deposition precipitation, wet impregnation and powder blending methods were investigated for supporting  $\text{Co}_3\text{O}_4$  on a high surface area, non-porous silica. Wet impregnation from cobalt nitrate was found to be the most effective method of synthesising supported  $\text{Co}_3\text{O}_4$  with minimal formation of undesired cobalt silicates. Activity increased with increased cobalt weight loading but supported catalysts displayed lower activity than bulk catalysts.

## Acknowledgements

I would like to thank my supervisors Professors Stan Golunski and Stuart Taylor for giving me the opportunity to undertake this research, and the support and freedom they provided throughout my PhD. I am grateful to Jaguar Land Rover and the EPSRC for funding the project and I wish to thank Ken Hansen, Jamil Khan, Dave Richardson and Lia Beddow at JLR.

Thank you to Dr Raimon Perea Marín for guiding me through all aspects of my PhD, Dr Tom Davies for many useful discussions and always finding time to help, Dr Dave Morgan for XPS analysis, and Dr Marco Conte for running in-situ XRD experiments. I am grateful for the professionalism, skills and friendliness of the staff in the School of Chemistry: Steve Morris, Alun Davies, Chris Morgan, Simon James, Sham Ali, Gaz Coleman, Dr Rob Jenkins, Robin Hicks, Tricia Wilson, Steve Rogers and Moira Northam.

Special thanks go to Ragini Ramdas and Sara Vieitez Calo for their camaraderie. I am grateful for the assistance and motivation from my colleagues in labs 1.86, 1.88 and 1.94.

Thank you to my family for supporting and encouraging me throughout my studies and always providing the security of home.

*In memory of Patrick O'Leary (1920–2010) and Mary Denbury (1921–2014).*

# Contents

<b>Declaration</b>	<b>i</b>
<b>Abstract</b>	<b>ii</b>
<b>Acknowledgements</b>	<b>iii</b>
<b>Contents</b>	<b>iv</b>
<b>Chapter 1 – Introduction</b>	<b>1</b>
1.1 Catalysis	1
1.2 Abatement of gasoline exhaust emissions	3
1.3 Co <sub>3</sub> O <sub>4</sub> catalysts for propane total oxidation	6
1.3.1 <i>Structure of Co<sub>3</sub>O<sub>4</sub></i>	7
1.3.2 <i>Mechanism of propane total oxidation over Co<sub>3</sub>O<sub>4</sub></i>	7
1.3.3 <i>Synthesis of Co<sub>3</sub>O<sub>4</sub></i>	8
1.4 Supported Co <sub>3</sub> O <sub>4</sub> catalysts for propane total oxidation	11
1.5 Project aims	12
1.6 References	13
<b>Chapter 2 – Experimental</b>	<b>15</b>
2.1 Catalyst preparation	15
2.1.1 <i>Bulk cobalt oxide</i>	15
2.1.1.1 Mechanochemical synthesis	16
2.1.1.2 Precipitation	16
2.1.2 <i>Silica supported cobalt oxide</i>	17
2.1.2.1 Deposition precipitation	18
2.1.2.2 Wet impregnation	18
2.1.2.3 Powder blending	19
2.2 Characterisation techniques	20
2.2.1 <i>Thermogravimetric Analysis-Differential Thermal Analysis</i>	20
2.2.2 <i>Scanning Electron Microscopy-Energy Dispersive X-ray Analysis</i>	21
2.2.3 <i>Powder X-ray Diffraction</i>	23
2.2.4 <i>Nitrogen Physisorption</i>	25
2.2.5 <i>Ultraviolet-visible Spectroscopy</i>	26
2.2.6 <i>Fourier Transform-Infrared Spectroscopy</i>	27
2.2.7 <i>Temperature Programmed Reduction</i>	28
2.2.8 <i>X-ray Photoelectron Spectroscopy</i>	28
2.3 Catalytic activity testing	29

2.3.1	<i>Propane total oxidation reactor</i>	29
2.3.2	<i>Product analysis</i>	31
2.4	References	33
<b>Chapter 3 – Preparation of Co<sub>3</sub>O<sub>4</sub> via mechanochemical reaction</b>		<b>34</b>
3.1	Introduction	34
3.2	Reaction of cobalt nitrate and ammonium hydrogen carbonate	34
3.2.1	<i>Investigation of grinding time and calcination temperature</i>	34
3.2.1.1	<i>Preparation</i>	34
3.2.1.2	<i>Results and Discussion</i>	35
3.2.1.3	<i>Conclusions</i>	57
3.2.2	<i>Investigation of calcination atmosphere</i>	58
3.2.2.1	<i>Preparation</i>	58
3.2.2.2	<i>Results and Discussion</i>	58
3.2.2.3	<i>Conclusions</i>	64
3.2.3	<i>Ball milling</i>	65
3.3	Reaction of cobalt nitrate and alternative bases	66
3.3.1	<i>Preparation</i>	66
3.3.2	<i>Results and Discussion</i>	68
3.3.3	<i>Conclusions</i>	79
3.4	An alternative cobalt oxide precursor: reaction of cobalt acetate and oxalic acid	79
3.4.1	<i>Preparation</i>	79
3.4.2	<i>Results and Discussion</i>	80
3.4.3	<i>Conclusions</i>	91
3.5	Chapter conclusions	92
3.6	References	92
<b>Chapter 4 – Preparation of Co<sub>3</sub>O<sub>4</sub> via precipitation</b>		<b>95</b>
4.1	Introduction	95
4.2	Investigation of starting materials and order of addition in the precipitation of Co <sub>3</sub> O <sub>4</sub> precursors	95
4.2.1	<i>Preparation</i>	95
4.2.2	<i>Results and Discussion</i>	99
4.2.3	<i>Conclusions</i>	113

4.3	Investigation of variables in the precipitation of cobalt hydroxycarbonate hydrate from cobalt acetate	113
	4.3.1 <i>Preparation</i>	114
	4.3.2 <i>Results and Discussion</i>	117
	4.3.3 <i>Conclusions</i>	128
4.4	Chapter conclusions	128
4.5	References	129
 <b>Chapter 5 – Silica supported cobalt catalysts for the total oxidation of propane</b>		<b>131</b>
5.1	Introduction	131
5.2	Investigation of preparation methods for supporting Co <sub>3</sub> O <sub>4</sub> on silica	131
	5.2.1 <i>Preparation</i>	131
	5.2.2 <i>Results and Discussion</i>	133
	5.2.3 <i>Conclusions</i>	156
5.3	Wet impregnation from cobalt nitrate: investigation of Co <sub>3</sub> O <sub>4</sub> loading	156
	5.3.1 <i>Preparation</i>	156
	5.3.2 <i>Results and Discussion</i>	157
	5.3.3 <i>Conclusions</i>	168
5.4	Chapter conclusions	169
5.5	References	169
 <b>Chapter 6 – Conclusions and future work</b>		<b>171</b>
6.1	Conclusions	171
6.2	Future work	173
6.3	References	174
 <b>Chapter 7 – Appendix</b>		<b>175</b>

# Chapter 1

## Introduction

### 1.1 Catalysis

A catalyst increases the rate of conversion of reactants to products during a chemical reaction without itself being consumed<sup>1</sup>. An alternative pathway for the reaction, with a lower activation energy compared to the uncatalysed reaction (Figure 1.1), is provided by a catalyst. The rate of attainment of chemical equilibrium is increased for the catalysed reaction, however the position of the equilibrium (i.e. the final equilibrium composition) and the thermodynamics of the reaction are unaltered.

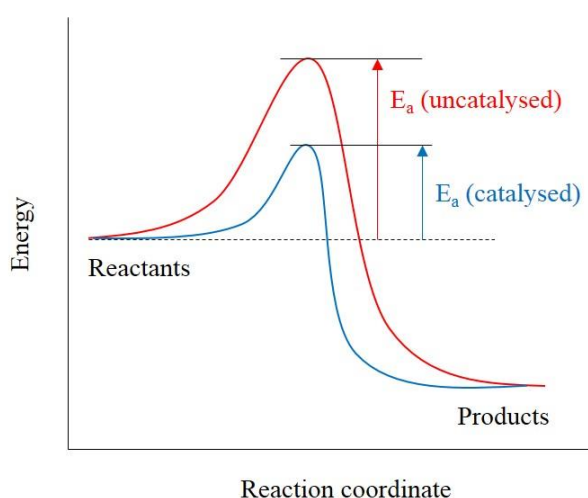
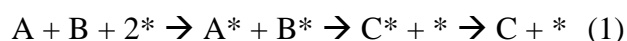


Figure 1.1 – Energy profiles for catalysed (blue line) and uncatalysed (red line) reactions. Reproduced from reference<sup>2</sup>.

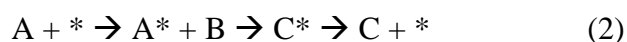
Catalysts can be divided into two categories: homogeneous catalysts function in the same phase as reactants, whilst heterogeneous catalysts are present in a separate phase to their reactants<sup>2</sup>. Homogeneous catalysts, which are typically soluble metal complexes in liquid phase reactions, generally operate under mild conditions and

demonstrate high selectivity due to the presence of one type of active site. Nonetheless, synthesis of homogeneous catalysts may involve multiple steps and reagents and their separation from reaction mixtures for reuse can be difficult and expensive, so large scale use of these catalysts may not be environmentally and economically justifiable<sup>3</sup>.  
<sup>4</sup>. Heterogeneous catalysts, which are typically solid catalysts with liquid or gas phase reactants, can be prepared more simply and are more easily separated and reused than homogeneous catalysts. However the heterogeneity of the surface of a heterogeneous catalyst can result in low selectivity and limited understanding of the active sites, especially under operating conditions<sup>5</sup>.

Heterogeneous catalytic reactions involve a number of distinct steps: reactants diffuse to then adsorb to the solid catalyst surface, adsorbed species react to form products and finally the products desorb from the surface and diffusion away from the catalyst occurs. For heterogeneously catalysed oxidation reactions, three main reaction mechanisms are reported<sup>2</sup>. In the Langmuir-Hinshelwood mechanism both reactant species adsorb to the catalyst surface before reaction occurs (where \* = catalyst surface site):



In the Eley-Rideal mechanism a reactant adsorbed to the catalyst surface reacts directly with a gas phase species:



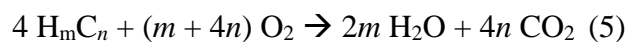
In the Mars-van Krevelen mechanism an adsorbed species reacts with lattice oxygen ( $O_l$ ), which, following desorption of the product, is replenished by oxygen from the gas phase ( $O_g$ ):



Heterogeneous catalysts are applied in a number of important industrial processes: the Haber-Bosch process utilises an iron catalyst in the production of ammonia<sup>6</sup>; zeolites are active in the catalytic cracking of high molecular weight hydrocarbons to more valuable products<sup>7</sup>; and, of greatest relevance here, the three-way catalyst employs precious metals for the abatement of harmful emissions from gasoline powered vehicles<sup>8</sup>.

## 1.2 Abatement of gasoline exhaust emissions

The combustion of gasoline fuel in a spark ignition engine would ideally yield only carbon dioxide and water, as shown in the following equation:



However, incomplete oxidation results in the emission of carbon monoxide (CO) and unburnt and partially combusted hydrocarbons (HCs), as well as oxides of nitrogen ( $NO_x$ )<sup>9</sup>. Reaction of emitted HCs and  $NO_x$  in the presence of sunlight leads to the formation of ground level ozone, a potent pollutant which causes respiratory and eye irritation and, along with particulate matter, constitutes photochemical smog<sup>9</sup>.

Legislation to reduce vehicle exhaust emissions was introduced in the USA during the 1970s as the frequent occurrence of smog in cities such as Los Angeles was a major

health concern<sup>10</sup>. European emission limits were first prescribed in 1993 (Euro 1), when the level for combined HCs and NO<sub>x</sub> emissions from gasoline powered vehicles was set to 0.97 g km<sup>-1</sup>. Legislation has become increasingly stringent, with HC emission limits set to 0.10 g km<sup>-1</sup> as of 2014 (Euro 6). The three-way catalyst (TWC), consisting of platinum, palladium and rhodium on an alumina washcoat, was developed to simultaneously reduce all three major pollutants: Pt and Pd are active for the oxidation of HCs and CO whilst Rh is active for the reduction of NO<sub>x</sub><sup>9</sup>. The catalyst is coated onto a ceramic or metallic monolith (Figure 1.2), which provides a high surface area for interaction of the exhaust gases with the catalyst without creating an undesirable pressure drop<sup>8</sup>.

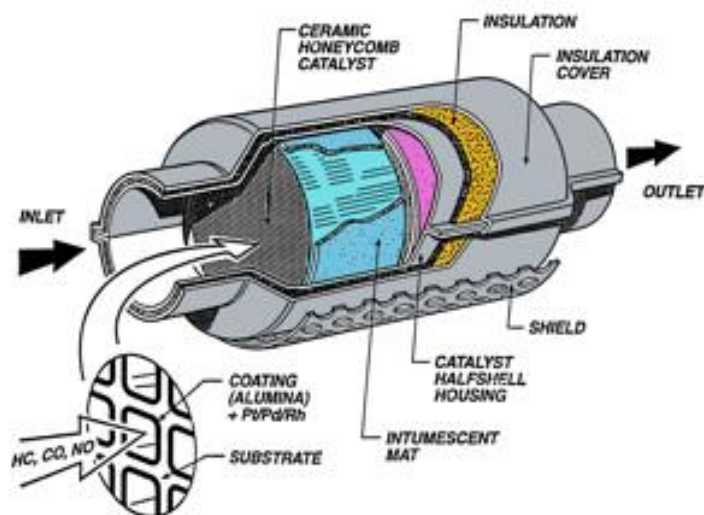
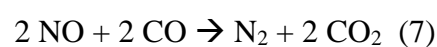
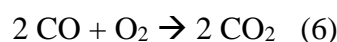


Figure 1.2 – Schematic of a three-way catalytic converter. Reproduced from reference<sup>8</sup>.

The main reactions which occur over a TWC are described by Equations 5 - 6 (oxidation reactions) and 7 - 8 (reduction reactions):



Several side-reactions may also occur, some of which give rise to undesirable products such as ammonia or nitrous oxide<sup>9</sup>.

The TWC is very efficient, reducing CO, HCs and NO<sub>x</sub> emissions by *ca.* 90%<sup>11</sup>. Despite the efficiency of the TWC, up to 80% of all emitted HCs are released during the first 120 seconds after the engine is started, before the TWC achieves light-off at *ca.* 300°C<sup>8</sup>. In order to meet the demands of future legislation limits and to minimise impacts on health, a requirement exists to reduce the ‘cold-start’ HC emissions which are released before the TWC reaches temperatures necessary for reaction light-off<sup>8</sup>. A number of methods have been investigated for reducing cold-start HC emissions such as close-coupled catalysts, electrically heated catalysts and hydrocarbon traps<sup>8</sup>. The drawbacks of these methods include reliance on expensive precious metals, the requirement of the materials to be stable at temperatures as high as 1050°C or issues with durability<sup>8</sup>. Exposure to excessively high temperatures may lead to premature catalyst deactivation through a number of mechanisms: crystallite growth of the active phase or collapse of a support – termed “sintering” – lead to a reduction in surface area, whilst transformation of the active phase, potentially due to interactions between the active phase and the support, can give a less active or inactive phase<sup>12</sup>. Catalysts which light-off at lower temperatures than the TWC offer an alternative cold-start solution<sup>13</sup>, and to avoid thermal deactivation these catalysts could be located away from the engine<sup>14</sup>.

Gasoline exhaust comprises a complex mixture of over 30 HCs<sup>15</sup>. The main components are short-chain alkanes and alkenes, oxygenates and aromatic species. Throughout this thesis propane will be used as a model short-chain saturated HC and

the activity of prepared catalysts will be evaluated for the total oxidation of propane, as linear short-chain alkanes are amongst the most difficult HCs to destroy<sup>16</sup>.

### 1.3 $\text{Co}_3\text{O}_4$ catalysts for propane total oxidation

Platinum and palladium are employed as the active components for HC oxidation in the commercial TWC as higher catalytic activity per site has traditionally been observed for precious metals compared to transition metal oxides (TMOs), and Pt and Pd in particular are less volatile than other precious metals<sup>16</sup>. Nonetheless, due to the scarcity and high cost of precious metals, TMOs present an economic alternative as HC total oxidation catalysts. Oxides of manganese<sup>17</sup>, iron<sup>18</sup> and copper<sup>19</sup> display good HC total oxidation activity but cobalt oxide is frequently found to be the most active TMO catalyst, especially the spinel  $\text{Co}_3\text{O}_4$  crystalline phase<sup>18, 20</sup>. Enhanced low temperature total oxidation activity, comparable to that of precious metal catalysts, has been reported for nanocrystalline  $\text{Co}_3\text{O}_4$ <sup>21</sup>.

The main disadvantage of cobalt oxide is the instability of the spinel phase at high temperatures: sintering and agglomeration of the  $\text{Co}_3\text{O}_4$  phase can occur from 500°C, leading to a decrease in surface area<sup>22</sup>, whilst at temperatures of 700°C and above transformation of  $\text{Co}_3\text{O}_4$  to the less active rock-salt structured CoO phase can occur<sup>23</sup>, with both phenomena resulting in reduced catalytic activity. Nevertheless, the spinel phase demonstrates good stability for total oxidation with time on line at reaction temperatures below 500°C<sup>21</sup>.

### 1.3.1 Structure of $\text{Co}_3\text{O}_4$

$\text{Co}_3\text{O}_4$ , which can also be written as  $\text{Co}^{2+}\text{Co}_2^{3+}\text{O}_4^{2-}$ , is the thermodynamically most stable phase of cobalt oxide under the typical conditions of catalytic oxidation<sup>24</sup>. In the spinel structure, oxide  $\text{O}^{2-}$  anions are arranged in a cubic close-packed lattice with  $\text{Co}^{2+}$  cations filling one eighth of the interstitial tetrahedral sites and  $\text{Co}^{3+}$  cations filling half of the interstitial octahedral sites<sup>25</sup>, as shown in Figure 1.3.

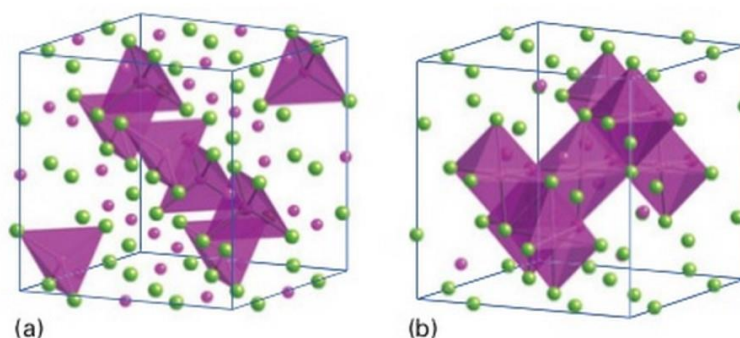


Figure 1.3 – The spinel structure of  $\text{Co}_3\text{O}_4$ : (a) tetrahedral environment of  $\text{Co}^{2+}$  ions and (b) octahedral environment of  $\text{Co}^{3+}$  ions. Green spheres =  $\text{O}^{2-}$ , purple spheres =  $\text{Co}^{2+}$  and  $\text{Co}^{3+}$ . Reproduced from reference<sup>26</sup>.

### 1.3.2 Mechanism of propane total oxidation over $\text{Co}_3\text{O}_4$

The mechanism by which the total oxidation of propane proceeds over  $\text{Co}_3\text{O}_4$  has been the subject of several studies. Liu *et al.*<sup>27</sup> indicated that electrophilic oxygen species ( $\text{O}^-$ ) weakly bound to the catalyst surface are active in propane total oxidation *via* a suprafacial mechanism. In this mechanism, surface oxygen vacancies provide electronic orbitals of appropriate symmetry and energy to enable bonding of the electrophilic  $\text{O}^-$ , which in turn activate the C-H bond of the propane molecule by homolytic abstraction of hydrogen<sup>28</sup>. Catalytic activity was found to correlate with the concentration of surface  $\text{O}^-$  species detected by  $\text{O}_2$ -TPD<sup>27</sup>.

In contrast, Finocchio *et al.*<sup>18,29,30</sup> followed the reaction using FT-IR spectroscopy and suggested that both partial and total oxidation proceed by a Mars-van Krevelen

mechanism: nucleophilic lattice oxide species ( $O^{2-}$ ) are utilised to oxidise the HC and the reduced catalyst surface is subsequently re-oxidised by molecular oxygen. Total oxidation is thought to occur *via* over-oxidation of adsorbed partial oxidation products, as shown in the scheme in Figure 1.4, with isopropoxide, acetates and acetone acting as intermediates in the combustion reaction<sup>30</sup>.

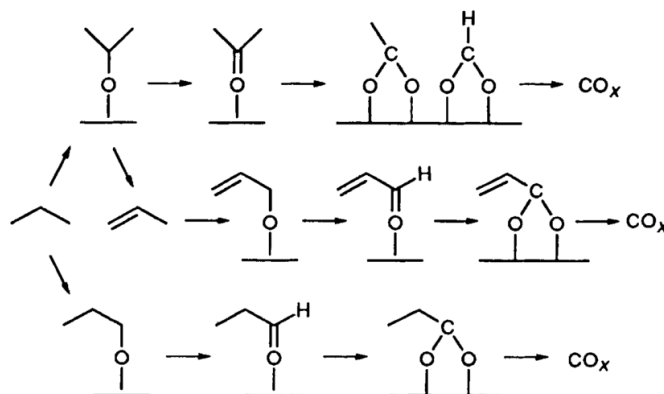


Figure 1.4 – Proposed scheme for the oxidation of propane over  $Co_3O_4$ . Reproduced from reference<sup>29</sup>

A further study employing the temporal analysis of products also concluded that the total oxidation of propane over cobalt oxide occurs by a Mars-van Krevelen mechanism<sup>22</sup>. When labelled  $^{18}O_2$  was utilised as a reactant with propane, only  $C^{16}O_2$  was initially obtained, confirming that lattice oxygen was the active oxygen species.

### 1.3.3 Synthesis of $Co_3O_4$

A variety of novel methods for the synthesis of  $Co_3O_4$  catalysts have been reported. Puertolas *et al.*<sup>31</sup> attempted to improve activity by mixing cobalt nitrate with solutions of organic acids which are thermally unstable. The formed mixture was calcined then tested for propane oxidation. The wet combustion procedure greatly improved the activity of manganese oxide catalysts due to the formation of a more active phase with a higher surface area, but a decrease in activity was observed for cobalt oxide due to a reduction in surface area compared to the acid-free catalyst. Iterations of a

supercritical anti-solvent (SAS) precipitation process combined with calcination were found to give very active  $\text{Co}_3\text{O}_4$  catalysts which achieved complete propane oxidation by  $250^\circ\text{C}$ <sup>32</sup>. The SAS precipitation is labelled as a ‘green chemistry’ process as a cobalt acetate salt is used to avoid nitrate effluent, which can damage the environment, and the supercritical  $\text{CO}_2$  can easily be recycled. Garcia *et al.*<sup>20</sup> synthesised ordered cobalt oxides with high surface areas *via* a nanocasting method. The catalysts exhibited good propane total oxidation activity, with complete conversion at  $225^\circ\text{C}$ , and high stability with time-on-stream at the elevated temperature of  $212^\circ\text{C}$ . Nonetheless, the multistep synthesis of the mesoporous silica template took approximately one week to complete and concentrated sodium hydroxide was required to remove the hard template before the  $\text{Co}_3\text{O}_4$  catalyst could be recovered. These novel synthesis methods do not always result in improved catalytic activity, and where improvements are made, the cost and complexity of the procedures may provide a hurdle for industrial implementation<sup>1</sup>.

Precipitation is often used to prepare industrially relevant catalysts, such as  $\text{Fe}_2\text{O}_3$  for Fischer-Tropsch reactions or  $\text{Cu}/\text{ZnO}$  for methanol synthesis<sup>1</sup>, yet only two routes for the precipitation of  $\text{Co}_3\text{O}_4$  for propane total oxidation have been reported. Reaction of cobalt nitrate or cobalt sulfate with lithium hydroxide gave  $\text{Co}(\text{OH})_2$ , which converted to  $\text{CoOOH}$  when the precipitate was dried<sup>33</sup>. The sulfate-derived  $\text{Co}_3\text{O}_4$  formed upon calcination of the dried precursor achieved complete propane conversion by  $230^\circ\text{C}$  and the high activity was attributed to the high porosity of the catalyst, which improved the accessibility of reactants to the surface.  $\text{Co}_3\text{O}_4$  has also been prepared from cobalt nitrate by precipitation with sodium carbonate, with the starting materials reacted at  $80^\circ\text{C}$  and pH 8.5 and the precipitates calcined at  $350^\circ\text{C}$  or  $425^\circ\text{C}$ <sup>27, 34</sup>. These catalysts

required temperatures of greater than 300°C for total propane conversion. Many synthesis variables may influence the nature of the precipitate formed during a precipitation reaction, as summarised in Figure 1.5, but the exact outcome can only be found empirically<sup>1</sup>. The potential exists for preparing a modified precipitate which, upon calcination, would give a Co<sub>3</sub>O<sub>4</sub> catalyst with superior propane oxidation activity.

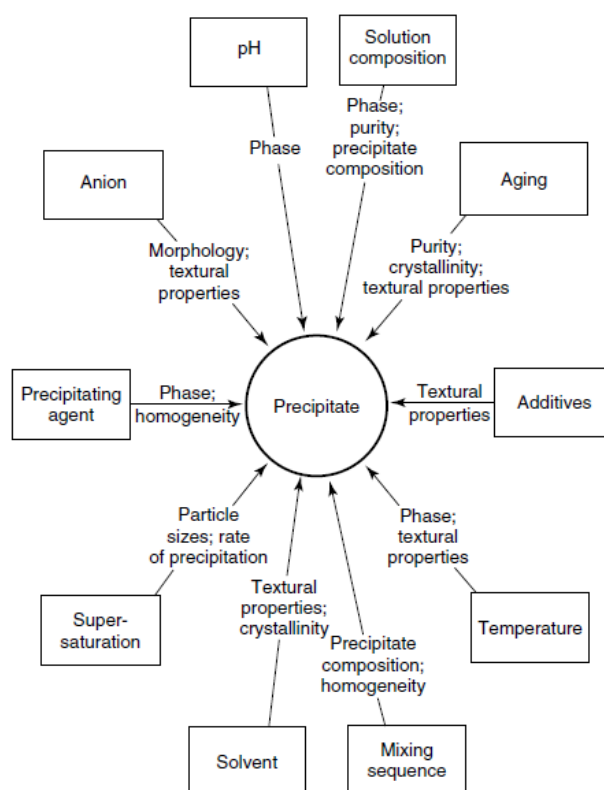


Figure 1.5 – Precipitation variables and the properties of the precipitate which may be altered. Reproduced from reference<sup>1</sup>.

Mechanochemistry has been reported as a route to catalysts with good low temperature activity. Davies *et al.*<sup>21, 22</sup> reported the first preparation of nanocrystalline Co<sub>3</sub>O<sub>4</sub> for propane oxidation by grinding together cobalt nitrate and ammonium hydrogen carbonate in a pestle and mortar in the absence of a solvent or any other additives. Calcination of the hydroxycarbonate precursor gave rise to a catalyst which could completely convert propane to CO<sub>2</sub> at a reaction temperature of just 200°C. Improved

activity was observed for the catalyst prepared with 30 minutes of grinding compared to shorter grinding. Active catalysts have also been prepared by the mechanochemical reaction of a cobalt hydroxycarbonate with citric acid, forming a cobalt citrate precursor<sup>27</sup>. The starting materials were ground in a planetary ball mill for durations of up to 6 hours and the final catalysts achieved total propane conversion by 240°C. Activity was found to increase with increased duration of grinding. Mechanochemical reactions offer the advantage of limiting the volume of solvent required – water or other solvents for washing are necessary in many reactions – which minimises their environmental impact<sup>35</sup>. As discussed for precipitation, a variety of reaction parameters may influence the products of mechanochemical reactions and investigation of further variables may yield catalysts with enhanced activity.

#### **1.4 Supported Co<sub>3</sub>O<sub>4</sub> catalysts for propane total oxidation**

As mentioned in *Section 1.3*, the high activity displayed by cobalt oxide at low temperatures is offset by the poor stability of the spinel phase at temperatures above 500°C<sup>22, 23</sup>. Sintering of the active phase may be prevented by supporting the Co<sub>3</sub>O<sub>4</sub> on oxides such as alumina, titania or silica<sup>12</sup>. Supported cobalt catalysts are utilised in a variety of applications, including Fischer-Tropsch synthesis<sup>36</sup> and methane total oxidation<sup>37</sup>, with the improved activity of the supported cobalt oxides compared to bulk catalysts attributed to high dispersion of the active species over the support, enabling more effective interaction with reactants<sup>38</sup>. The formation of compounds such as cobalt aluminates, Co-Al-O, or cobalt silicates, Co-Si-O, by interactions between Co<sub>3</sub>O<sub>4</sub> and the support should be avoided as cobalt in these compounds does not contribute to the activity of the catalyst<sup>39</sup>.

The most thermally stable supports under oxidising conditions are  $\gamma$ -alumina and silica<sup>40</sup>. Relatively few studies of supported  $\text{Co}_3\text{O}_4$  for the total oxidation of propane have been performed. Solsona *et al.*<sup>22</sup> investigated  $\text{Co}_3\text{O}_4$  catalysts supported on a range of aluminas and found fewer inactive cobalt aluminate species formed with lower surface area supports, which lead to greater catalytic activity. Different methods of supporting  $\text{Co}_3\text{O}_4$  on a high surface area silica have been investigated, and the catalysts tested for the total oxidation of propane<sup>41</sup>. A hydrothermal route was found to be most effective for the synthesis of high activity, stable catalysts with a Co loading of approximately 24wt%, with complete conversion of propane achieved at temperatures below 300°C *via* a Mars-van Krevelen mechanism.

## 1.5 Project aims

The aim of this research is to synthesize catalysts which display high activity for HC oxidation at low temperatures. Propane will be used as a model short-chain saturated HC and the preparation of cobalt oxide catalysts will be investigated. Limited variables have been examined in the synthesis of  $\text{Co}_3\text{O}_4$  *via* precipitation and mechanochemical reaction, hence a systematic study will be performed to establish optimal conditions to give high activity catalysts for propane total oxidation. Finally the  $\text{Co}_3\text{O}_4$  catalysts will be supported on a fumed silica support. The influence of parameters such as starting materials, reaction time and calcination conditions will be investigated. The characteristics of the prepared precursors and catalysts will be linked to the activity of the catalysts in the oxidation reaction. Precipitation and mechanochemical synthesis can be performed with minimal reagents and energy input to reduce the environmental and economic impact of the catalysts, and a variety of straightforward methods will be investigated to produce supported catalysts.

## 1.6 References

1. *Handbook of Heterogeneous Catalysis*, Wiley-VCH, Weinheim, 2008.
2. P. Atkins and J. De Paula, *Atkins' Physical Chemistry*, OUP, Oxford, 2006.
3. G. J. Hutchings, *J. Mater. Chem.*, 2009, **19**, 1222-1235.
4. J. H. Clark and D. J. Macquarrie, *Chem. Soc. Rev.*, 1996, **25**, 303-310.
5. I. Lopes, A. Davidson and C. Thomas, *Catal. Commun.*, 2007, **8**, 2105-2109.
6. M. G. Scheibel and S. Schneider, *Angew. Chem.-Int. Edit.*, 2012, **51**, 4529-4531.
7. *Catalysis: An Integrated Approach*, Elsevier, Amsterdam, 2000.
8. R. M. Heck and R. J. Farrauto, *Appl. Catal. A-Gen.*, 2001, **221**, 443-457.
9. R. Stone, *Introduction to Internal Combustion Engines*, Society of Automotive Engineers, 1999.
10. M. V. Twigg, *Applied Catalysis B: Environmental*, 2007, **70**, 2-15.
11. S. H. Chan, *Proc. Inst. Mech. Eng. Part D-J. Automob. Eng.*, 2001, **215**, 545-555.
12. C. H. Bartholomew, *Applied Catalysis A: General*, 2001, **212**, 17-60.
13. J. R. Mellor, A. Palazov, B. S. Grigorova, J. F. Greyling, K. Reddy, M. P. Letsoalo and J. H. Marsh, *Catal. Today*, 2002, **72**, 145-156.
14. *Structured Catalysts and Reactors*, CRC Press, Florida, 2006.
15. J. K. Pearson, *Improving Air Quality: Progress and Challenges for the Auto Industry*, SAE International, 2001.
16. T. V. Choudhary, S. Banerjee and V. R. Choudhary, *Applied Catalysis A: General*, 2002, **234**, 1-23.
17. M. Baldi, E. Finocchio, F. Milella and G. Busca, *Appl. Catal. B-Environ.*, 1998, **16**, 43-51.
18. G. Busca, M. Daturi, E. Finocchio, V. Lorenzelli, G. Ramis and R. J. Willey, *Catal. Today*, 1997, **33**, 239-249.
19. S. Arnone, G. Bagnasco, G. Busca, L. Lisi, G. Russo and M. Turco, in *Studies in Surface Science and Catalysis*, eds. A. Parmaliana, D. Sanfilippo, F. Frusteri, A. Vaccari and F. Arena, Elsevier, 1998, pp. 65-70.
20. T. Garcia, S. Agouram, J. F. Sanchez-Royo, R. Murillo, A. M. Mastral, A. Aranda, I. Vazquez, A. Dejoz and B. Solsona, *Appl. Catal. A-Gen.*, 2010, **386**, 16-27.
21. B. Solsona, I. Vazquez, T. Garcia, T. E. Davies and S. H. Taylor, *Catalysis Letters*, 2007, **116**, 116-121.
22. B. Solsona, T. E. Davies, T. Garcia, I. Vazquez, A. Dejoz and S. H. Taylor, *Appl. Catal. B-Environ.*, 2008, **84**, 176-184.
23. L. F. Liotta, G. Di Carlo, G. Pantaleo, A. M. Venezia and G. Deganello, *Applied Catalysis B: Environmental*, 2006, **66**, 217-227.
24. G. Busca, R. Guidetti and V. Lorenzelli, *Journal of the Chemical Society, Faraday Transactions*, 1990, **86**, 989-994.
25. E. Alizadeh-Gheshlaghi, B. Shaabani, A. Khodayari, Y. Azizian-Kalandaragh and R. Rahimi, *Powder Technol.*, 2012, **217**, 330-339.
26. P. Atkins, T. Overton, J. Rourke, M. Weller and F. Armstrong, *Shriver & Atkins' Inorganic Chemistry*, OUP, Oxford, 2009.
27. Q. Liu, L. C. Wang, M. Chen, Y. Cao, H. Y. He and K. N. Fan, *Journal of Catalysis*, 2009, **263**, 104-113.
28. N. A. Merino, B. P. Barbero, P. Grange and L. E. Cadús, *Journal of Catalysis*, 2005, **231**, 232-244.

29. E. Finocchio, G. Busca, V. Lorenzelli and V. S. Escribano, *J. Chem. Soc.-Faraday Trans.*, 1996, **92**, 1587-1593.
30. E. Finocchio, R. J. Willey, G. Busca and V. Lorenzelli, *J. Chem. Soc.-Faraday Trans.*, 1997, **93**, 175-180.
31. B. Puertolas, A. Smith, I. Vazquez, A. Dejoz, A. Moragues, T. Garcia and B. Solsona, *Chem. Eng. J.*, 2013, **229**, 547-558.
32. R. P. Marin, S. A. Kondrat, R. K. Pinnell, T. E. Davies, S. Golunski, J. K. Bartley, G. J. Hutchings and S. H. Taylor, *Appl. Catal. B-Environ.*, 2013, **140**, 671-679.
33. G. Salek, P. Alphonse, P. Dufour, S. Guillemet-Fritsch and C. Tenailleau, *Appl. Catal. B-Environ.*, 2014, **147**, 1-7.
34. B. Solsona, T. Garcia, G. J. Hutchings, S. H. Taylor and M. Makkee, *Appl. Catal. A-Gen.*, 2009, **365**, 222-230.
35. J. A. Schwarz, C. Contescu and A. Contescu, *Chem. Rev.*, 1995, **95**, 477-510.
36. J. W. Bae, Y. J. Lee, J. Y. Park and K. W. Jun, *Energy Fuels*, 2008, **22**, 2885-2891.
37. U. Zavyalova, P. Scholz and B. Ondruschka, *Appl. Catal. A-Gen.*, 2007, **323**, 226-233.
38. J. Taghavimoghaddam, G. P. Knowles and A. L. Chaffee, *Journal of Molecular Catalysis A: Chemical*, 2012, **358**, 79-88.
39. R. Trujillano, J.-F. Lambert and C. Louis, *The Journal of Physical Chemistry C*, 2008, **112**, 18551-18558.
40. F. E. Trigueiro, C. M. Ferreira, J. C. Volta, W. A. Gonzalez and P. G. P. de Oliveria, *Catal. Today*, 2006, **118**, 425-432.
41. Z. Z. Zhu, G. Z. Lu, Z. G. Zhang, Y. Guo, Y. L. Guo and Y. Q. Wang, *ACS Catal.*, 2013, **3**, 1154-1164.

# Chapter 2

## Experimental

*This chapter describes the preparation of bulk and supported metal oxide catalysts, the analytical techniques used to characterise these catalysts, and the catalytic test reaction of propane total oxidation.*

### 2.1 Catalyst preparation

This section outlines the methods used for catalyst preparation. The nomenclature adopted for the prepared catalysts is summarised at the beginning of each corresponding data chapter. Table 2.1 lists the chemicals used in this work.

Table 2.1: Chemicals used in this work

Chemical formula	Company	Grade / purity
$\text{Co}(\text{NO}_3)_2 \cdot 6\text{H}_2\text{O}$	Sigma Aldrich	ACS reagent, $\geq 98.0\%$
$\text{Co}(\text{CH}_3\text{COO})_2 \cdot 4\text{H}_2\text{O}$	Sigma Aldrich	ACS reagent, $\geq 98.0\%$
$\text{NH}_4\text{HCO}_3$	Sigma Aldrich	ReagentPlus, $\geq 99.0\%$
$(\text{NH}_4)_2\text{CO}_3$	Sigma Aldrich	ACS reagent, $\geq 30.0\%$ $\text{NH}_3$ basis
$\text{NaHCO}_3$	Sigma Aldrich	ACS reagent, $\geq 99.7\%$
$\text{Na}_2\text{CO}_3$	Sigma Aldrich	$\geq 99.0\%$
$\text{C}_2\text{H}_2\text{O}_4 \cdot 2\text{H}_2\text{O}$	Alfa Aesar	ACS reagent, $\geq 99.5\%$
$\text{SiO}_2$	Degussa	Aerocat
$\text{Co}_3\text{O}_4$	Sigma Aldrich	$< 10 \mu\text{m}$ particle size
5 wt% Pt/ $\text{Al}_2\text{O}_3$	Johnson Matthey	

#### 2.1.1 Bulk cobalt oxide

Mechanochemical synthesis and precipitation were used to prepare bulk (unsupported)

$\text{Co}_3\text{O}_4$  catalysts.

### 2.1.1.1 Mechanochemical synthesis

Bulk  $\text{Co}_3\text{O}_4$  catalysts were prepared mechanochemically from a cobalt salt and an acid or a base followed by calcination, based on a method described previously<sup>1</sup>. The variables studied are shown in Table 2.2.

Table 2.2: Variables studied in the mechanochemical synthesis of bulk cobalt oxide

Experimental parameter	Studied variables
Cobalt salt	$\text{Co}(\text{NO}_3)_2 \cdot 6\text{H}_2\text{O}$ (cobalt nitrate) $\text{Co}(\text{CH}_3\text{COO})_2 \cdot 4\text{H}_2\text{O}$ (cobalt acetate)
Acid or base	$\text{NH}_4\text{HCO}_3$ (ammonium hydrogen carbonate) $(\text{NH}_4)_2\text{CO}_3$ (ammonium carbonate) $\text{NaHCO}_3$ (sodium hydrogen carbonate) $\text{Na}_2\text{CO}_3$ (sodium carbonate) $\text{C}_2\text{H}_2\text{O}_4 \cdot 2\text{H}_2\text{O}$ (oxalic acid)
Molar ratio of Co salt to acid or base	2:5 1:1
Mixing time (min)	10 30
Calcination temperature ( $^\circ\text{C}$ )	300 400 500
Calcination heating rate ( $^\circ\text{C min}^{-1}$ )	1 10
Calcination atmosphere	flowing air (50 mL $\text{min}^{-1}$ air through sealed tubular furnace) static air (no gas flow through sealed tubular furnace) open air (no gas flow through open tubular furnace)

In a typical experiment the cobalt salt and the acid or base were ground together on a 25 g scale in a 125 mL capacity glass pestle and mortar. The mixture was washed with 1 L of deionised water and filtered then dried in a static air oven at  $110^\circ\text{C}$  overnight and finally ground to a powder in an agate pestle and mortar to give the catalyst precursor. Calcination of the precursor in a tube furnace for 2 h followed by grinding in the agate pestle and mortar yielded the  $\text{Co}_3\text{O}_4$  catalyst.

### 2.1.1.2 Precipitation

Bulk  $\text{Co}_3\text{O}_4$  catalysts were prepared by precipitation from a cobalt salt and a precipitating agent followed by calcination. The variables studied are shown in Table 2.3.

Table 2.3: Variables studied in the precipitation of bulk cobalt oxide

Experimental parameter	Studied variables
Cobalt salt	Co(NO <sub>3</sub> ) <sub>2</sub> ·6H <sub>2</sub> O (cobalt nitrate) Co(CH <sub>3</sub> COO) <sub>2</sub> ·4H <sub>2</sub> O (cobalt acetate)
Precipitating agent	Na <sub>2</sub> CO <sub>3</sub> (sodium carbonate) C <sub>2</sub> H <sub>2</sub> O <sub>4</sub> ·2H <sub>2</sub> O (oxalic acid)
Order of reagent addition	Precipitating agent to Co salt Co salt to precipitating agent
Molar ratio of Co salt:precipitating agent	1:1 1:2 1:4
Cobalt salt concentration (M)	0.1 0.25 1
Precipitating agent concentration (M)	0.1 0.25 0.5 1
Aging time (h)	0.25 2 6

In a typical experiment a 100 mL aqueous solution of the cobalt salt was added dropwise over 15 min to a 100 mL aqueous solution of the precipitating agent (or *vice versa*) under constant stirring (setting 3 on a Stuart hotplate) in a 250 mL round bottom flask. All reactions were performed at room temperature. The formed precipitate was aged with stirring at the reaction temperature then washed with 1 L of deionised water and filtered. The precipitate was dried in a static air oven at 110°C overnight then ground to a powder in an agate pestle and mortar to give the catalyst precursor. Calcination of the precursor in open air for 2 h at 300°C (10°C min<sup>-1</sup>) followed by grinding in the agate pestle and mortar yielded the Co<sub>3</sub>O<sub>4</sub> catalyst.

### 2.1.2 Silica supported cobalt oxide

Deposition precipitation, impregnation, and powder blending were investigated for the preparation of supported Co<sub>3</sub>O<sub>4</sub> catalysts.

### 2.1.2.1 Deposition precipitation

Catalysts composed of 3.7 wt% Co/SiO<sub>2</sub> were prepared by the addition of an aqueous solution of precipitating agent to a stirred aqueous solution of cobalt acetate containing 1 g of silica. The precipitating agent solution, 100 mL of sodium carbonate or oxalic acid with a concentration of 6.6 mM, was added dropwise over 15 min to 100 mL of a 6.6 mM cobalt acetate solution. After stirring for 2 h at room temperature the solid was filtered and washed with 1 L of deionised water, dried at 110°C in a static air oven overnight then ground in an agate pestle and mortar to give the catalyst precursor. Calcination of the precursor in open air at 300°C (10°C min<sup>-1</sup>) for 2 h followed by grinding in the agate pestle and mortar yielded the final catalyst.

### 2.1.2.2 Wet impregnation

Catalysts composed of 3.7 wt% Co/SiO<sub>2</sub> were prepared by stirring 1 g of SiO<sub>2</sub> in 50 mL of a 13.2 mM aqueous solution of cobalt acetate or cobalt nitrate at 80°C until a paste was formed. The paste was dried at 110°C in a static air oven overnight then ground in an agate pestle and mortar to give the catalyst precursor. Calcination of the precursor in open air at 300°C (10°C min<sup>-1</sup>) for 2 h followed by grinding in the agate pestle and mortar yielded the final catalyst.

Catalysts with weight loadings of 7.5, 19.6 and 42.3 wt% Co/SiO<sub>2</sub> were prepared from cobalt nitrate by the wet impregnation method described above, altering only the mass of cobalt nitrate.

### 2.1.2.3 Powder blending

Bulk  $\text{Co}_3\text{O}_4$  was firstly prepared from cobalt acetate and sodium carbonate by precipitation at room temperature: a 100 mL aqueous solution cobalt acetate with a concentration of 0.25 M was added dropwise over 15 min to a stirred 100 mL aqueous solution of sodium carbonate with a concentration of 0.25 M. The solution was aged with stirring at room temperature for 2 h then filtered and the precipitate washed with 1 L of deionised water. The precipitate was dried in a static air oven at  $110^\circ\text{C}$  overnight then ground to a powder in an agate pestle and mortar to give the catalyst precursor (cobalt hydroxycarbonate hydrate). Calcination of the precursor in open air for 2 h at  $300^\circ\text{C}$  ( $10^\circ\text{C min}^{-1}$ ) followed by grinding in the agate pestle and mortar yielded the  $\text{Co}_3\text{O}_4$  catalyst. These samples are equivalent to the precursor and catalyst presented in Chapter 4 which are named ‘AtoC’.

Catalysts composed of 3.7 wt%  $\text{Co/SiO}_2$  were prepared by stirring 1 g of  $\text{SiO}_2$  with the  $\text{Co}_3\text{O}_4$  (0.053 g) or the precipitated hydroxycarbonate (0.064 g) in water (50 mL) at room temperature for 0.5 h. The water was subsequently removed by stirring the mixture at  $80^\circ\text{C}$ . The mixture was dried at  $110^\circ\text{C}$  in a static air oven overnight then ground in an agate pestle and mortar to give the catalyst precursor. Calcination of the precursor in open air at  $300^\circ\text{C}$  ( $10^\circ\text{C min}^{-1}$ ) for 2 h followed by grinding in the agate pestle and mortar yielded the final catalyst.

## 2.2 Characterisation techniques

This section outlines the theory and experimental conditions of the analytical techniques used in this work. The term ‘sample’ is used to refer to the precursor or catalyst materials under investigation.

### 2.2.1 *Thermogravimetric Analysis-Differential Thermal Analysis*

Thermogravimetric Analysis-Differential Thermal Analysis (TGA-DTA) is used to observe chemical and physical transformations of a sample as it is heated in a specific atmosphere<sup>2</sup>. TGA records the change of mass of a sample as a function of temperature with the occurrence of processes such as decomposition, oxidation or loss of solvent. DTA is performed concurrently with TGA and records the difference in temperature between the sample crucible and a reference crucible as the sample evolves or absorbs heat. Most processes observed in TGA-DTA are kinetic, hence variables which can alter reaction rate must be kept constant between experiments to prevent transformation temperatures from shifting. Such variables include sample mass and packing in the crucible, heating rate, reaction atmosphere and its flow rate, and the size and material of the crucible.

In this work a Setaram Labsys TGA-DTA 1600 was used to study the transformation of precursors into catalysts. Each sample (40 mg of bulk  $\text{Co}_3\text{O}_4$  precursor or 15 mg of silica supported precursor, unless otherwise stated) was heated in a 100  $\mu\text{L}$  alumina crucible over the temperature range 30-950°C (1 or 10°C  $\text{min}^{-1}$ ) under flowing air (50  $\text{mL min}^{-1}$ ). The relative error in the weight change was determined to be  $\pm 5\%$  based on three repetitions.

### **2.2.2 Scanning Electron Microscopy-Energy Dispersive X-ray Analysis**

Scanning Electron Microscopy-Energy Dispersive X-ray Analysis (SEM-EDX) is used to image samples and perform elemental microanalysis<sup>3</sup>. Electrons are emitted from a gun which contains an electrically heated tungsten filament. Electromagnetic lenses then focus the electrons: a condenser lens focuses the electrons into a beam (termed the incident electron beam) and an objective lens focuses the beam onto the sample. Scanning coils scan/raster the beam over the surface of the sample row by row. Detector signals resulting from beam-sample interactions are synchronised with the beam position and an image or spectrum is recorded on a computer screen. The whole system is under vacuum to prevent scattering of the electron beam.

Two types of signals can give rise to an SEM image:

- (i) Secondary electrons are emitted from the sample following inelastic interactions with electrons from the incident electron beam. Secondary electrons have relatively low energies so only those produced near the surface of the sample escape and reach the detector – others are recaptured by the sample. Secondary electron micrographs therefore show topographical (surface features/texture) and morphological (particle shape and size) features of the sample. Due to the large depth of field of an SEM three dimensional-like images are obtained.
- (ii) Backscattered electrons are incident beam electrons which have been scattered back out of the sample following one or more elastic collisions. A greater proportion of electrons are backscattered with increasing atomic number,  $Z$ , and hence compositional contrast is observed in backscattered electron micrographs: areas of the sample with higher mean atomic number are brighter than areas with lower

mean atomic number as brightness depends on the number of electrons reaching the detector.

EDX utilises characteristic X-ray signals for elemental analysis. The vacancy created upon emission of a secondary electron, as described above, is filled by a higher energy electron and excess energy may be released as an X-ray. The energy of the X-ray is equal to the difference in energy between the two electron shells and as this value is unique for each element the chemical composition of the sample can be determined. Continuum X-rays (Bremsstrahlung) are also emitted as the incident electron beam is slowed by the sample and an X-ray spectrum consists of characteristic X-rays superimposed on this background. In addition to qualitative information, EDX is used for quantitative analysis with a detection limit of approximately 0.5% and sample composition can be determined to an overall accuracy of approximately 2%. EDX cannot be used for quantitative analysis of light elements ( $Z < 11$ ) but the concentration of oxygen present in metal oxide samples can be calculated by stoichiometry if the oxidation states of the associated cations are known.

In this work samples loaded onto adhesive carbon discs were analysed using a Carl-Zeiss EVO 40 microscope operated at 20-25 kV with EDX analysis calibrated against a cobalt standard. Topographical and morphological features were inspected from secondary electron micrographs, elemental distribution was examined using backscattered electron micrographs in conjunction with X-ray maps, and quantitative EDX analysis was performed to determine loadings for supported catalysts.

### 2.2.3 Powder X-ray Diffraction

Powder X-ray Diffraction (XRD) is used to identify crystalline phases and estimate average crystallite sizes<sup>3</sup>. Electrons from an electrically heated tungsten filament are accelerated towards a copper target to generate secondary X-rays (as described for EDX in Section 2.2.2). Monochromatic  $K\alpha$  X-rays are directed towards the catalyst sample and the incident X-ray beam is elastically scattered by atoms in a periodic lattice as shown in Figure 2.1.

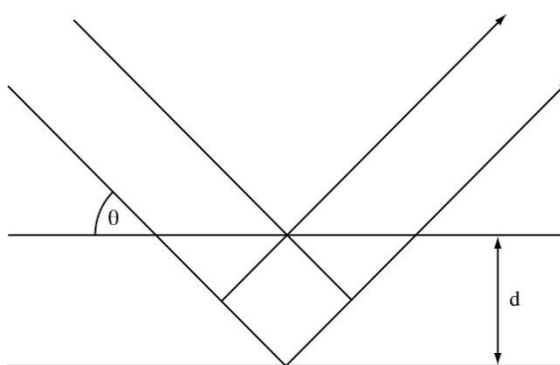


Figure 2.1 – Scattering of X-rays by lattice planes

The incident and diffracted beams pass through a series of slits which counter the divergence of the beams and increase the resolution of the diffraction pattern. A peak is observed in the pattern when the scattered X-rays are in-phase and produce constructive interference, and this is achieved when the Bragg equation is satisfied:

$$n\lambda = 2d \sin \theta$$

where  $n$  = an integer number,  $\lambda$  = X-ray wavelength,  $d$  = lattice spacing,  $\theta$  = angle between incident X-ray beam and sample (Bragg angle).

Crystallites are randomly orientated in all possible directions in powder samples so all sets of lattice planes are detected as the Bragg angle is scanned. Phases are identified by comparison of the recorded pattern with a database as each phase has a pattern with characteristic peak positions and intensities. XRD requires long range order of the

lattice, hence crystallites smaller than 2 nm, phases present in low concentrations and amorphous phases are not detected.

The size of a crystallite can be estimated from the full-width half-maximum (FWHM) of the most intense diffraction peak by employing the Scherrer equation:

$$\text{average crystallite size} = \frac{K \lambda}{\beta \cos \theta}$$

where  $K$  = Scherrer constant (often taken as 1),  $\lambda$  = X-ray wavelength,  $\beta$  = peak FWHM,  $\theta$  = angle of incidence of X-ray beam.

In this work crystalline phases were identified using a PANalytical X'Pert Pro diffractometer with a monochromatic Cu  $K\alpha$  source ( $\lambda = 0.154$  nm) operated at 40 kV and 40 mA. Diffraction patterns were collected in the  $2\theta$  range of 10-80°. A Ni filter was fitted between the diffracted beam and the detector to filter fluorescence from samples containing cobalt. Line broadening was referenced to a highly crystalline silicon standard. The relative error in the calculation of crystallite size was determined to be  $\pm 5\%$  based on three repetitions.

For in-situ XRD experiments under TPR conditions, the  $\text{Co}_3\text{O}_4$  sample was placed in an Anton Paar XRK 900 reaction chamber and the reactant gas flow rates and temperature programming from the associated ex-situ TPR experiment were utilised. Patterns were recorded at 50°C intervals, with the temperature held constant at each set-point for 8 min as the spectra were collected. These experiments were performed by Dr Marco Conte.

### 2.2.4 Nitrogen Physisorption

Nitrogen physisorption is used to determine the specific surface area of a sample. Two identical evacuated cells, one containing the sample and the other empty to act as a reference, are dosed with a given relative pressure of nitrogen gas. Physisorption of the nitrogen onto the sample surface results in a lower pressure in the sample cell compared to the reference cell and this differential, which corresponds to the volume of gas adsorbed, is recorded as nitrogen is dosed at a range of relative pressures. The experimental data is then processed according to the Brunauer-Emmett-Teller (BET) theory<sup>4</sup>, which extends the Langmuir theory of monolayer adsorption to multilayer adsorption.

The volume of gas required for monolayer coverage of the sample,  $V_{\text{mono}}$ , is derived from the intercept and slope of a plot of the BET equation:

$$\frac{P}{V_a([P_0/P] - 1)} = \frac{C - 1}{V_{\text{mono}}C} \times \frac{P}{P_0} + \frac{1}{V_{\text{mono}}C}$$

where  $V_a$  = volume of adsorbed gas;  $P_0$  = saturation pressure;  $P$  = equilibrium pressure;  $V_{\text{mono}}$  = volume of adsorbed gas for monolayer coverage;  $C$  = BET constant.

The specific surface area ( $S_{\text{BET}}$ ) of the sample can then be calculated:

$$S_{\text{BET}} = \frac{V_{\text{mono}}N_A A}{V} / m$$

where  $N_A$  = Avogadro's constant,  $6.022 \times 10^{23} \text{ mol}^{-1}$ ;  $A$  = cross-sectional area of adsorbate molecule,  $0.162 \text{ nm}^2$  for nitrogen;  $V$  = molar volume of adsorbate at STP,  $22.4 \text{ dm}^3 \text{ mol}^{-1}$ ;  $m$  = mass of sample analysed.

In this work specific surface areas were determined using a Micromeritics Gemini 2360 Surface Area Analyser and a five point BET method in the relative pressure

range of 0.05-0.35, with adsorption of nitrogen at  $-196^{\circ}\text{C}$ . Each sample (ca. 0.1 g) was pre-treated for 1 h under flowing helium at  $110^{\circ}\text{C}$  in a Micromeritics FlowPrep 060 Degasser to remove adsorbed surface species before analysis. The relative error in the surface area was determined to be  $\pm 7\%$  based on three repetitions.

### 2.2.5 *Ultraviolet-visible Spectroscopy*

Ultraviolet-visible Spectroscopy (UV-vis) is used to excite electronic transitions to assist in structural determination of samples<sup>5</sup>. Molecules are irradiated with radiation from the ultraviolet and visible regions of the electromagnetic spectrum. When the energy of the radiation is equal to the difference in energy between an occupied molecular orbital and a higher energy unoccupied molecular orbital, radiation may be absorbed causing the promotion of an electron. Two types of these transitions from the electronic ground state to electronic excited states can occur in transition metal complexes: (i) charge transfer (CT) transitions involving the metal and its associated ligands and (ii) metal centred (MC) d-d transitions. The energy of a transition depends on the geometry of the complex, the oxidation state of the metal ion and the identity of the ligands, hence bands will occur at characteristic positions in the spectrum for a given molecule.

In this work spectra were recorded on a Varian Cary 4000 spectrometer in the range 200-800 nm at a scan speed of  $150\text{ nm min}^{-1}$ . A deuterium lamp was used as the UV source ( $\lambda < 350\text{ nm}$ ) and a tungsten halogen lamp was used as the visible light source ( $\lambda > 350\text{ nm}$ ). Samples were analysed in diffuse reflectance mode: the intensity of light reflected from the sample ( $I$ ) is compared to the intensity of light reflected from a reference material ( $I_0$ , taken to be 100%), to give reflectance,  $R = I/I_0$ . The 100%

reflectance baseline spectrum was recorded using a white PTFE disc. Absorbance of radiation by a sample to promote an electronic transition results in decreased reflection.

### ***2.2.6 Fourier Transform-Infrared Spectroscopy***

Fourier Transform-Infrared Spectroscopy (FT-IR) is used to identify bonds present in a sample to assist in structural determination<sup>5</sup>. Molecules are irradiated with infrared radiation and absorption of energy, which causes transitions between vibrational energy levels, may occur when the energy of the radiation is equal to the difference in energy between two adjacent vibrational levels. A band is observed in the IR spectrum provided that the molecular vibration causes a change in dipole moment of the molecule. The percentage of radiation absorbed as a function of energy is detected and an IR spectrum is plotted as percentage transmission against wavenumber in  $\text{cm}^{-1}$  (where wavenumber is equal to the reciprocal of the wavelength of the radiation). The position of a band in the IR spectrum depends on the constituent atoms of the chemical bond, the strength of the bond, and the type of molecular vibration (a stretch or a bend), hence vibrations associated with a given bond will always appear at characteristic positions in the spectrum.

In this work spectra were recorded using a Shimadzu IRAffinity-1 FT-IR spectrometer in attenuated total reflectance (ATR) mode. Powdered sample was clamped to the stage to ensure good contact between the sample and the surface of the ATR crystal. Total internal reflection of the IR beam within the crystal creates an evanescent wave which extends into the sample. Energy absorbed by the sample attenuates the evanescent wave and this change is detected in the reflected IR beam which travels

from the crystal to the detector. For each spectrum 64 scans were acquired at an instrument resolution of  $4\text{ cm}^{-1}$  in the range  $4000\text{-}500\text{ cm}^{-1}$ .

### ***2.2.7 Temperature Programmed Reduction***

Temperature Programmed Reduction (TPR) is used to monitor the reduction of a metal oxide as a function of temperature<sup>3</sup>. A flow of a reducing gas mixture (hydrogen diluted in argon) is passed over the sample as it is heated at a constant rate. Hydrogen is consumed as the metal oxide is reduced and the difference between the hydrogen concentration in the effluent gas stream and a reference gas stream is monitored by a thermal conductivity detector (TCD). The effluent gas stream is passed through a trap before reaching the detector to remove water generated during reduction.

In this work catalyst reducibility was determined using a Thermo TPDRO 1100 apparatus. Each sample (15 mg of bulk  $\text{Co}_3\text{O}_4$  or 15-90 mg of silica supported catalyst, depending on weight loading) was packed between quartz wool plugs in a quartz reactor tube and pre-treated in helium ( $20\text{ mL min}^{-1}$ ) at  $110^\circ\text{C}$  ( $10^\circ\text{C min}^{-1}$ ) for 1 h. After cooling, TPR analysis was performed using a gas flow of 10%  $\text{H}_2/\text{Ar}$  ( $15\text{ mL min}^{-1}$ ) from 30 to  $950^\circ\text{C}$  ( $5^\circ\text{C min}^{-1}$ ).

### ***2.2.8 X-ray Photoelectron Spectroscopy***

X-ray Photoelectron Spectroscopy (XPS) is used to identify the chemical composition of the surface of a sample<sup>5</sup>. Under ultra-high vacuum, electrons from a thermionic source are directed towards a metal target (typically aluminium) to generate secondary X-rays (as described for EDX in Section 2.2.2). Monochromatic  $\text{K}\alpha$  X-rays are then directed towards the catalyst sample and cause photoelectrons to be ejected from core-

and valence-level orbitals. The kinetic energy of each photoelectron can be approximated by the Einstein equation:

$$E_K = h\nu - E_B$$

where  $E_K$  = kinetic energy of photoelectron,  $h\nu$  = energy of incident X-ray (1486.6 eV for Al  $K\alpha$  radiation), and  $E_B \approx$  the orbital energy for the electron in the atom.

Analysis of the peaks in the resulting spectrum corresponding to photoelectrons from core level orbitals gives quantitative elemental composition and chemical state information, such as oxidation state. Due to the small inelastic mean free paths of photoelectrons, only those ejected from approximately the top 10 nm of the surface are detected.

In this work XPS analysis was performed using a Kratos Axis Ultra DLD photoelectron spectrometer with a monochromatic Al  $K\alpha$  source operated at a pass energy of 40 eV. All samples were calibrated to the C 1s signal of adventitious carbon at a binding energy of 284.7 eV. These experiments were performed by Dr David Morgan.

## **2.3 Catalytic activity testing**

### ***2.3.1 Propane total oxidation reactor***

Catalysts were tested for the total oxidation of propane at atmospheric pressure in a fixed bed micro-reactor. A schematic of the rig is given in Figure 2.2.

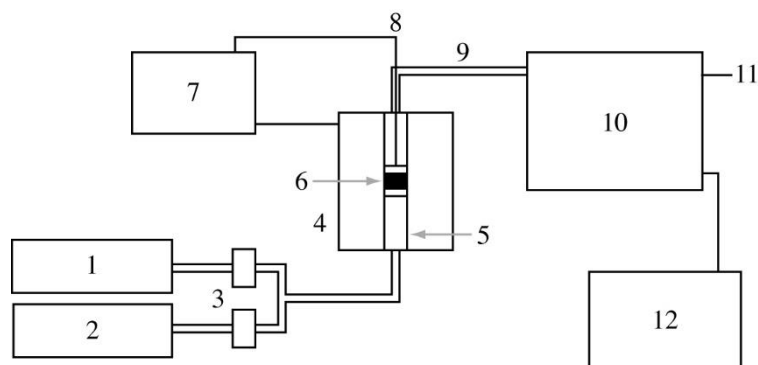


Figure 2.2 – Schematic of the propane total oxidation reactor: (1) 5000 ppm propane/He cylinder, (2) oxygen cylinder, (3) mass flow controllers, (4) tube furnace, (5) reactor tube, (6) catalyst bed, (7) furnace controller, (8) thermocouple, (9) heated exit line, (10) gas chromatograph, (11) outlet to vent, (12) computer

For each experiment powdered catalyst was packed to a constant volume (0.067 mL) between quartz wool plugs in a  $\frac{1}{4}$ " o.d. stainless steel reactor tube and heated in a tube furnace. A gas feed of 5000 ppm propane in helium ( $40 \text{ mL min}^{-1}$ ) and oxygen ( $10 \text{ mL min}^{-1}$ ) was passed over the catalyst, corresponding to a propane:oxygen ratio of 1:50 vol% and a gas hourly space velocity (GHSV) of  $45,000 \text{ h}^{-1}$ . The mass flow controllers were calibrated before use and gas flows were measured at the vent before the start of each reaction to check for leaks and blockages. Activity measurements were taken at intervals of 25 or  $50^\circ\text{C}$  in the temperature range of  $100\text{-}350^\circ\text{C}$ , with temperatures measured by a K-type thermocouple placed on top of the catalyst bed. Three steady-state measurements were taken at each temperature and the results averaged. Exhaust gas was analysed by on-line gas chromatography. The exit line from the reactor to the gas chromatograph (GC) was heated to  $110^\circ\text{C}$  to prevent condensation of water and any hydrocarbons formed in partial oxidation side reactions. Blank experiments were also performed using a reactor tube containing only quartz wool to test for homogeneous gas phase reactions over the temperature range used in this work and negligible activity was found (see Appendix, Figure A1).

### 2.3.2 Product analysis

Analytes constituting the reactor exhaust gas were separated and analysed by a Varian 3800 GC. Gases were injected onto the first column by a gas sampling valve (V1 in Figure 2.3) and transported by helium carrier gas.

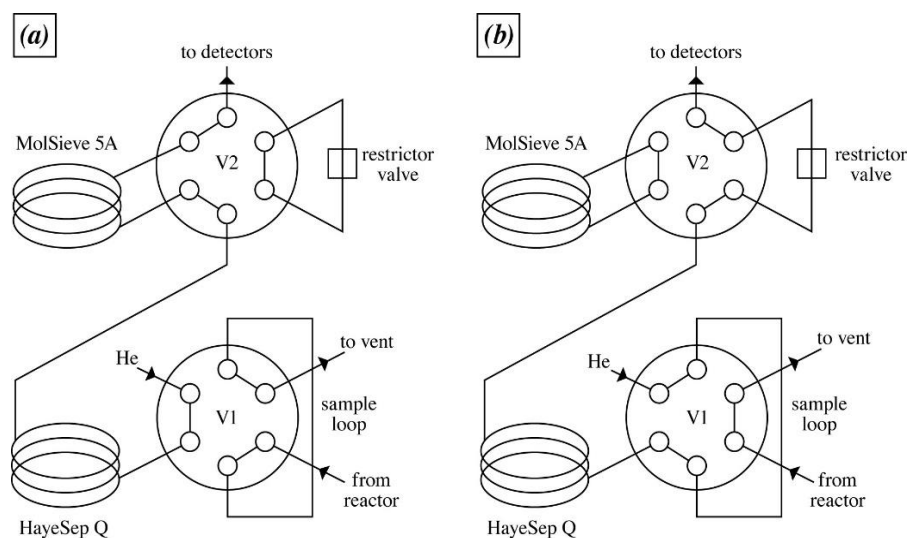


Figure 2.3 – Schematic of GC valves: (a) V1 in fill position and V2 in series position, (b) V1 in inject position and V2 in bypass position

A HayeSep Q column (80-100 mesh, 1.8 m) separated hydrocarbons and CO<sub>2</sub> and a MolSieve 13 X column (80-100 mesh, 2 m) separated O<sub>2</sub> and CO. As CO<sub>2</sub> irreversibly binds to and deactivates the MolSieve, a second valve (V2 in Figure 2.3) was used to bypass this column after elution of O<sub>2</sub> and CO. Separation was achieved by adsorption of the analytes to the stationary phases, with more strongly interacting analytes being retained in the columns for longer. Temperature programming of the column oven (shown in Table 2.5) was employed to achieve separation of the analytes with good resolution without excessively long retention times.

Table 2.5 – Column oven temperature programme

Column oven temperature (°C)	Ramp rate (°C min <sup>-1</sup> )	Hold time (min)	Total time (min)
50	-	0.00	0.00
68	2.0	3.50	12.50
220	70.0	2.50	17.17

After separation and elution of the analytes from the columns a thermal conductivity detector (TCD) was used to detect O<sub>2</sub>, CO<sub>2</sub> and CO and a flame ionisation detector (FID) was used to detect propane and any hydrocarbons formed in partial oxidation side reactions.

Quantitative and qualitative analysis was achieved by calibration of the GC with known concentrations of analytes and the calculation of a response factor (RF) for each compound, where  $RF = \text{known \% injected} / \text{peak area counts}$ . The percentage of each analyte from propane oxidation could then be determined by multiplication of peak area counts by the relevant RF. Analytes were identified by comparison of their retention times with those of the known compounds.

The following equation was used to determine propane conversion at each temperature after correcting for the carbon number of each product:

$$\text{Conversion} = (\text{products}_{\text{out}} / (\text{products}_{\text{out}} + \text{propane}_{\text{out}})) \times 100$$

Where  $\text{products}_{\text{out}}$  refers to the average counts of all oxidation products and  $\text{propane}_{\text{out}}$  refers to the average propane counts.

Carbon balances were in the range 95-105%. By testing three portions of the same catalyst, the relative error of the data was determined to be  $\pm 4\%$ .

The selectivity to each product was determined using the following equation after correcting for carbon number:

$$\text{Selectivity} = (\text{amount of product, P} / \text{total amount of products including P}) \times 100$$

## 2.4 References

1. H. Yang, Y. Hu, X. Zhang and G. Qiu, *Materials Letters*, 2004, **58**, 387-389.
2. D. Skoog, F. Holler and S. Crouch, *Principles of Instrumental Analysis*, Thomson Brooks/Cole, Australia, 2006.
3. J. W. Niemantsverdriet, *Spectroscopy in Catalysis An Introduction*, Wiley-VCH, Weinheim, 2007.
4. S. Brunauer, P. H. Emmett and E. Teller, *Journal of the American Chemical Society*, 1938, **60**, 309-319.
5. *Handbook of Heterogeneous Catalysis*, Wiley-VCH, Weinheim, 2008.

# Chapter 3

## Preparation of $\text{Co}_3\text{O}_4$ via mechanochemical reaction

### 3.1 Introduction

In this chapter the preparation of  $\text{Co}_3\text{O}_4$  by mechanochemical synthesis and subsequent thermal decomposition of a precursor is studied. A number of variables are investigated, namely the starting materials, grinding time and calcination conditions. The samples are characterised by a range of techniques and the catalysts are tested for the total oxidation of propane.

### 3.2 Reaction of cobalt nitrate and ammonium hydrogen carbonate

#### 3.2.1 Investigation of grinding time and calcination temperature

##### 3.2.1.1 Preparation

Cobalt nitrate (15.0 g) and ammonium hydrogen carbonate (10.2 g) were ground together for 10 or 30 minutes according to the method described in *Section 2.1.1.1*. The precursors were calcined for 2 hours at 300, 400 or 500°C with a heating rate of  $1^\circ\text{C min}^{-1}$  in open air (no gas flow through an open tubular furnace). This information and the nomenclature of the prepared samples are summarised in Table 3.1.

Table 3.1 – Sample nomenclature

Sample <sup>a</sup>	Grinding time (min)	Calcination temperature (°C)	Heating rate (°C min <sup>-1</sup> )	Calcination atmosphere
G10 <sup>b</sup>	10	-	-	-
G10-300-1-o	10	300	1	open air
G10-400-1-o	10	400	1	open air
G10-500-1-o	10	500	1	open air
G30 <sup>b</sup>	30	-	-	-
G30-300-1-o	30	300	1	open air
G30-400-1-o	30	400	1	open air
G30-500-1-o	30	500	1	open air

a – Sample nomenclature takes the format: Grinding time (min) – calcination temperature (°C) – heating rate (°C min<sup>-1</sup>) – calcination atmosphere, where o = open air

b – Uncalcined catalyst precursors

The starting materials were mixed with a molar ratio of 2:5 as the reaction was originally reported to proceed *via* the following equation<sup>1</sup>:



As grinding commenced the mixture quickly turned wet and viscous with the formation of water and the mortar became cold, indicating the reaction was endothermic. Bubbles were visible in the mixture for approximately 10 minutes as ammonia and carbon dioxide were released. The mixture turned bright pink then a berry purple colour. No colour change was observed beyond this, even after grinding for an extended duration of 1 hour.

### 3.2.1.2 Results and Discussion

The XRD patterns of the precursors from 10 and 30 minutes of grinding are shown in Figure 3.1, with the Miller indices given in brackets. The diffraction peaks were very broad and had low intensities, indicating that poorly crystalline materials were produced by grinding. Nevertheless, both precursors could be assigned to hydrated cobalt hydroxycarbonate ( $\text{Co}(\text{OH})_x(\text{CO}_3)_{0.5(2-x)} \cdot n\text{H}_2\text{O}$ )<sup>2</sup>, which has also been referred to as cobalt hydroxide carbonate<sup>3</sup> and cobalt basic carbonate<sup>4</sup>. This hydrated

orthorhombic phase of cobalt hydroxycarbonate can be differentiated from the anhydrous  $\text{Co}_2(\text{OH})_2\text{CO}_3$  monoclinic phase by comparison of their XRD patterns<sup>2</sup>.

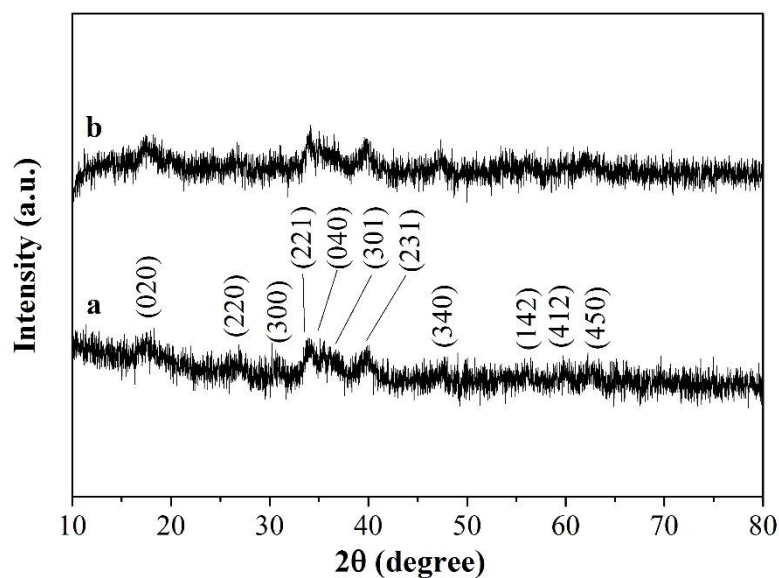


Figure 3.1 – XRD patterns of (a) G10 and (b) G30

The FT-IR spectra of the precursors are shown in Figure 3.2. Stretching vibrations of the carbonate anion were present at  $1455$ ,  $1371$  and  $1073\text{ cm}^{-1}$  whilst the bands observed at  $830$ ,  $740$  and  $668\text{ cm}^{-1}$  were due to bending vibrations of the carbonate anion<sup>3</sup>. The broad band centred at  $3480\text{ cm}^{-1}$ , due to OH stretching, indicated the presence of water and/or hydrogen-bonded hydroxyl anions<sup>3</sup>. Likewise the weak band at  $1040\text{ cm}^{-1}$ , due to OH bending, may be attributed to water and/or hydroxyl anions<sup>5</sup>. The band at  $962\text{ cm}^{-1}$  was assigned to the Co-OH bending vibration<sup>3</sup>. Overall, the spectra indicated that hydrated cobalt hydroxycarbonate was produced after both 10 and 30 minutes of grinding. Bands were also observed in the spectra due to atmospheric  $\text{H}_2\text{O}$  (centred at  $3750$  and  $1675\text{ cm}^{-1}$ ) and atmospheric  $\text{CO}_2$  (centred at  $2350\text{ cm}^{-1}$ )<sup>6</sup>.

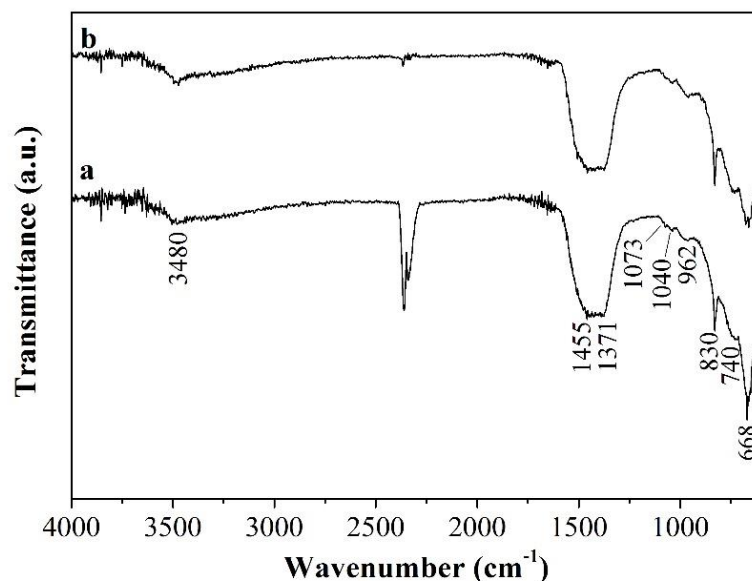
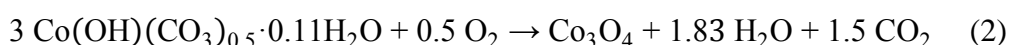


Figure 3.2 – FT-IR spectra of (a) G10 and (b) G30

TGA-DTA was performed to probe the thermal decomposition of the precursors in an oxidative atmosphere and the results are shown in Figure 3.3. A weight loss of 25.6% was observed for G30, which matches the theoretical weight change of 25.6% for the transformation of the reported compound  $\text{Co}(\text{OH})(\text{CO}_3)_{0.5} \cdot 0.11\text{H}_2\text{O}$  to the spinel phase of cobalt oxide based on the following equation<sup>7</sup>:



A smaller weight loss of 23.0% was observed for G10. Previously, a range of  $\text{Co}(\text{OH})_x(\text{CO}_3)_{0.5(2-x)} \cdot n\text{H}_2\text{O}$  compounds, with differing values of  $x$  and  $n$  calculated from CHN analysis and TGA data, have been reported to display similar XRD and FT-IR profiles, irrespective of differences in their formulae<sup>3</sup>. As CHN analysis was not performed in the current work, the formulae of both the G10 and G30 precursors are assumed to be  $\text{Co}(\text{OH})_x(\text{CO}_3)_{0.5(2-x)} \cdot n\text{H}_2\text{O}$ .

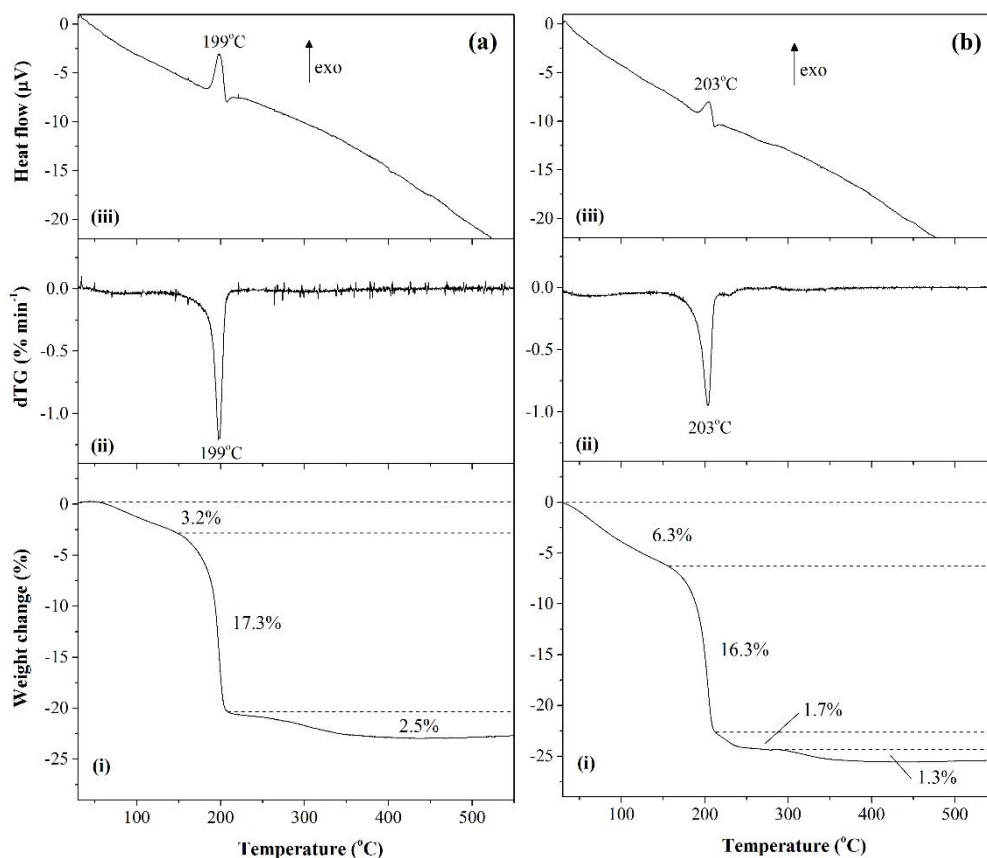


Figure 3.3 – (i) TGA, (ii) dTG and (iii) DTA curves of (a) G10 & (b) G30. Experiments were performed at 1°C min<sup>-1</sup>

The G10 sample displayed three main decomposition steps, while four steps were observed for the G30 sample. The first weight loss of 3-6% occurred gradually until 150°C and can be attributed to the loss of surface-adsorbed water and water of crystallisation. The smaller percentage loss of H<sub>2</sub>O from G10 indicated that the sample contained less water of crystallisation than G30, as the proportion of adsorbed water on the samples was likely to be similar following overnight oven-drying. Centred at *ca.* 200°C, the second weight loss of approximately 17% was accompanied by a weak exothermic peak. This step was assigned to the decomposition of hydroxyl and carbonate groups and the simultaneous oxidation of Co<sup>2+</sup> to Co<sup>3+</sup> to form the oxide catalyst<sup>3,8</sup>. The weak exothermic peak resulted from a combination of the endothermic decomposition of the precursor anions and the exothermic oxidation of cobalt ions<sup>9</sup>.

The extra weight loss step for G30 was observed as a small shoulder at *ca.* 230°C. Li *et al.*<sup>2</sup> postulated that such a shoulder was due to the decomposition of residual carbonates. This assignment correlates with a TGA-MS study of the decomposition of copper zinc hydroxycarbonates, which found that a “high-temperature carbonate” was decomposed after the dehydroxylation and decarbonation which occur in the main weight loss step<sup>10</sup>. Previous studies have shown that this extra step is present for hydrated cobalt hydroxycarbonate, but is not observed for anhydrous cobalt hydroxycarbonate<sup>2</sup>. Whilst G10 has been assigned as hydrated based upon its XRD pattern, the absence of the “high-temperature carbonate” peak further suggests that G10 contained less water of crystallisation than G30, in agreement with lower weight loss observed in the first decomposition step. The final weight loss for both samples occurred gradually until 370°C. This could be indicative of the formation of a non-stoichiometric oxide at 200°C, which slowly transformed to Co<sub>3</sub>O<sub>4</sub> with increasing temperature<sup>11</sup>.

The above TGA data showed that all three weight loss steps occurred or were underway by 300°C, indicating that an extended calcination at a temperature of 300°C may be sufficient for the formation of cobalt oxide. A TGA experiment emulating calcination for 2 hours at 300°C was performed to determine if full decomposition of the precursors, including any residual carbonates, would occur. A sample of G30 was heated to 300°C at a rate of 1°C min<sup>-1</sup> then held at that temperature for 2 hours. As can be seen in Figure 3.4, the four weight loss regions were observed under these calcination conditions and the final weight loss step was completed during the two hour isotherm. The total weight loss observed was 24.2%, which is in agreement with

the expected value, within the experimental error of  $\pm 5\%$ . A minimum temperature of  $300^{\circ}\text{C}$  was therefore chosen for calcination of the precursors.

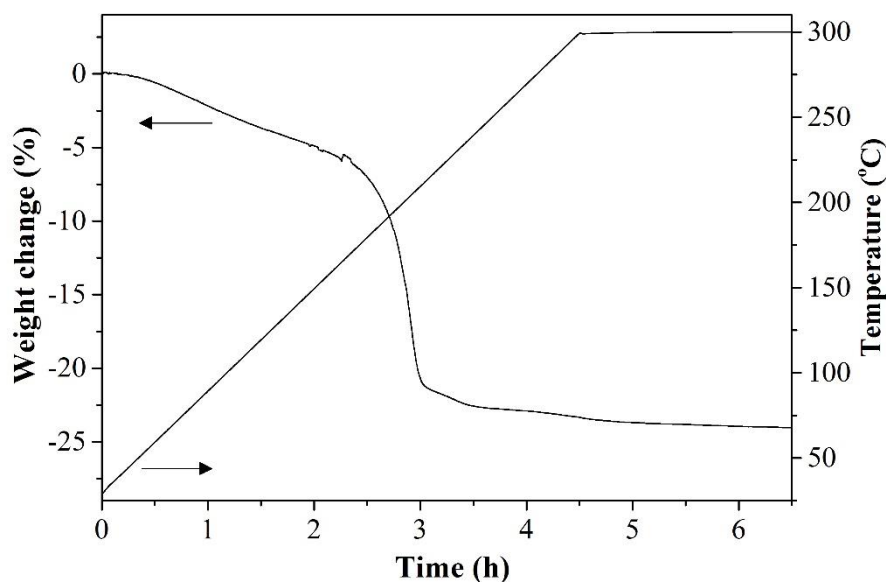


Figure 3.4 – TGA curve of G30 under calcination conditions

Figure 3.5 shows the XRD patterns of the catalysts formed by calcination of G10 and G30 at  $300$ ,  $400$  and  $500^{\circ}\text{C}$ . In all cases, the observed diffraction peaks corresponded to the spinel  $\text{Co}_3\text{O}_4$  phase<sup>12</sup>, as expected from the TGA weight change calculations, which were based on the formation of this phase. No peaks relating to the precursors or other cobalt phases were present, hence complete conversion to  $\text{Co}_3\text{O}_4$  was assumed. The XRD pattern of commercial  $\text{Co}_3\text{O}_4$  (Figure 3.5 (g)) presented diffraction peaks which were narrower and of higher intensities than those of the mechanochemical catalysts, indicating a higher degree of crystallinity in the commercial sample. However, the peaks of the mechanochemical catalysts became less broad and more intense with increasing calcination temperature, which suggested that more crystalline materials were produced at higher temperatures. The strong influence of calcination temperature on crystallite growth has formerly been reported for  $\text{Co}_3\text{O}_4$  derived from the cobalt hydroxycarbonate hydrate precursor<sup>1</sup>. Crystallite

sizes (shown in Table 3.2) were determined by the Scherrer equation using the full-width half-maximum of the most intense diffraction peak at  $2\theta = 37.1^\circ$ . Calcination at 300, 400 and 500°C gave rise to average crystallite sizes of approximately 10, 23, and 47 nm, respectively, and no clear differences could be distinguished between the G10 and G30 catalysts. The commercial sample presented very large crystallites of 220 nm in size.

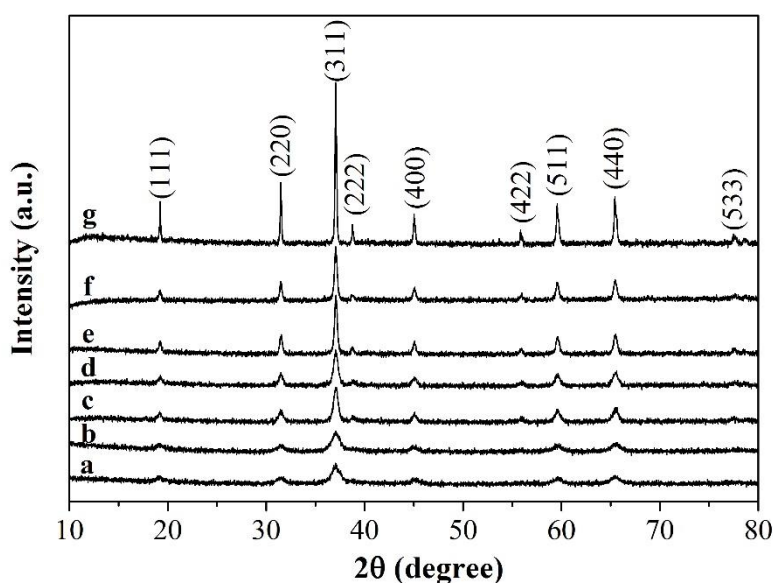


Figure 3.5 – XRD patterns of (a) G10-300-1-o, (b) G30-300-1-o, (c) G10-400-1-o, (d) G30-400-1-o, (e) G10-500-1-o, (f) G30-500-1-o and (g) commercial  $\text{Co}_3\text{O}_4$

Close examination of the XRD patterns revealed that the peaks appeared at slightly lower diffraction angles for the commercial sample compared to the mechanochemical samples. The appearance of the peaks of the mechanochemical catalysts at higher angles indicated that these samples possessed a contracted (*i.e.* distorted) unit cell<sup>13</sup>. Such a shift relative to a commercial sample has been reported previously for  $\text{Co}_3\text{O}_4$  and the distortion was apportioned to a greater number of defects in the prepared catalysts<sup>14</sup>. A previous study of the mechanochemical preparation of  $\text{Co}_3\text{O}_4$ , using a ball mill and grinding times of up to six hours, found that diffraction peaks shifted to higher angles with extended duration of grinding<sup>13</sup>. In the present work no differences

were identified between the G10 and G30 catalysts, suggesting that a difference in grinding time of 20 minutes was too short for such modifications to occur.

The BET specific surface areas of the precursors and catalysts are presented in Table 3.2. As noted for other characterisation techniques, similar results were observed irrespective of the initial duration of grinding. The cobalt hydroxycarbonate hydrates were synthesised with relatively high surface areas of *ca.* 125 m<sup>2</sup> g<sup>-1</sup>. Calcination at 300°C led to a slight increase in surface area compared to the precursors, with a greater increase observed for the G10-derived sample. Surface areas decreased progressively at higher temperatures, falling by approximately 60-80% compared to the catalysts prepared at 300°C. The decrease in surface area with increasing calcination temperature correlates with the increase in crystallite size observed in XRD experiments and suggests the occurrence of crystallite growth and sintering<sup>15</sup>. Commercial Co<sub>3</sub>O<sub>4</sub> presented a very low surface area of 1 m<sup>2</sup> g<sup>-1</sup>, which was not unexpected considering the very large crystallite size of the sample.

Table 3.2 – Physicochemical characteristics of precursors and catalysts

Sample	Co <sub>3</sub> O <sub>4</sub> crystallite size (nm)	Surface area (m <sup>2</sup> g <sup>-1</sup> )	Co-O IR bands (cm <sup>-1</sup> )	
			Co <sup>2+</sup>	Co <sup>3+</sup>
G10	-	127	-	-
G10-300-1-o	10	137	658	561
G10-400-1-o	22	51	658	558
G10-500-1-o	47	22	657	556
G30	-	123	-	-
G30-300-1-o	10	128	658	558
G30-400-1-o	23	50	658	558
G30-500-1-o	46	26	657	555
commCo <sub>3</sub> O <sub>4</sub>	220	1	-	-

Figure 3.6 shows the FT-IR spectra of the catalysts. Two intense bands due to Co-O stretching vibrations were observed at *ca.* 658 and 558 cm<sup>-1</sup>. The frequencies at which

the bands were detected are given in Table 3.2. The first band, which is attributed to tetrahedrally coordinated  $\text{Co}^{2+}$  ions in the spinel structure of  $\text{Co}_3\text{O}_4$ <sup>16</sup>, appeared at a similar position for each catalyst. The second band is ascribed to octahedrally coordinated  $\text{Co}^{3+}$  ions<sup>16</sup>. The latter band appeared at slightly lower wavenumbers with increasing calcination temperature. Likewise, the band was observed at lower wavenumbers for the G30 catalysts compared to the G10 catalysts at each calcination temperature except 400°C. Such a shift to a lower wavenumber may be assigned to a decrease in Co-O bond strength<sup>14</sup>. Two shoulders were also distinguished in the spectrum centred at 677 and 596  $\text{cm}^{-1}$ . These can be assigned to longitudinal modes of the  $\text{Co}^{2+}$  and  $\text{Co}^{3+}$  vibrations, respectively, whilst the more intense bands discussed above are due to transverse vibrations<sup>17</sup>. The two pairs of bands are typically observed in FT-IR spectra recorded in reflectance mode (as used in the current work), whereas only transverse vibrations are seen in transmission spectra<sup>18</sup>.

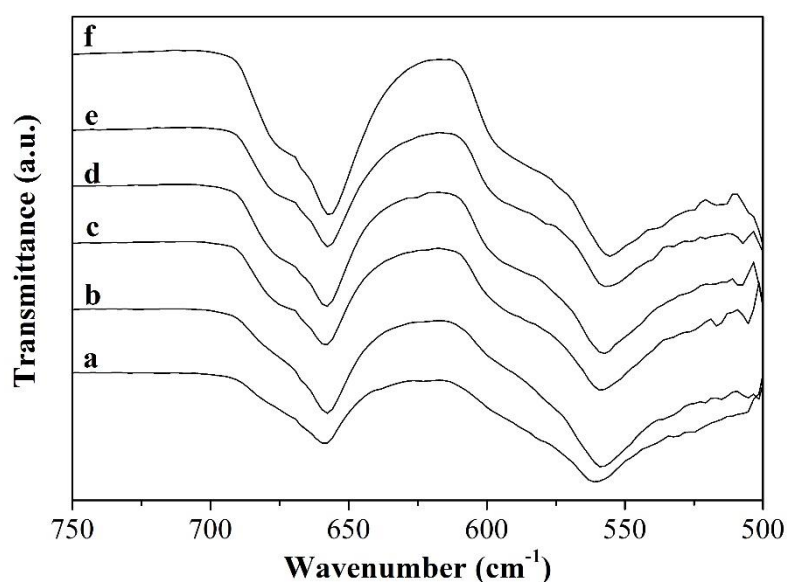


Figure 3.6 – FT-IR spectra of (a) G10-300-1-o, (b) G30-300-1-o, (c) G10-400-1-o, (d) G30-400-1-o, (e) G10-500-1-o and (f) G30-500-1-o

Secondary electron SEM micrographs of G30-300-1-o are shown in Figure 3.7. At low magnification (Figure 3.7 (a)) it could be seen the catalyst consisted of irregularly

shaped particles of a broad range of sizes, ranging from less than 1  $\mu\text{m}$  up to 150  $\mu\text{m}$  in size. Higher magnifications (Figure 3.7 (b)) revealed that larger particles were made up of aggregates of smaller particles, which gave rise to rough surfaces. Each small particle is assumed to be an aggregate composed of the nanoscale crystallites observed in XRD analysis<sup>19</sup>. Some particles presented smooth faces, but inspection of their edges revealed roughness. Similar morphologies and varieties of particle sizes were observed for all of the G10 and G30 precursors and catalysts, and variations due to calcination at different temperatures were not apparent. Micrographs of the commercial catalyst are shown in Figure 3.7 (c) and (d). In contrast to the mechanochemical samples, the commercial  $\text{Co}_3\text{O}_4$  appeared to have a very regular structure with particles of a much smaller size range between *ca.* 0.5 and 2  $\mu\text{m}$ . Each cubic particle presented a smooth surface. The better agreement between the XRD crystallite size and the observed particle sizes could be due to less agglomeration of crystallites to form particles.

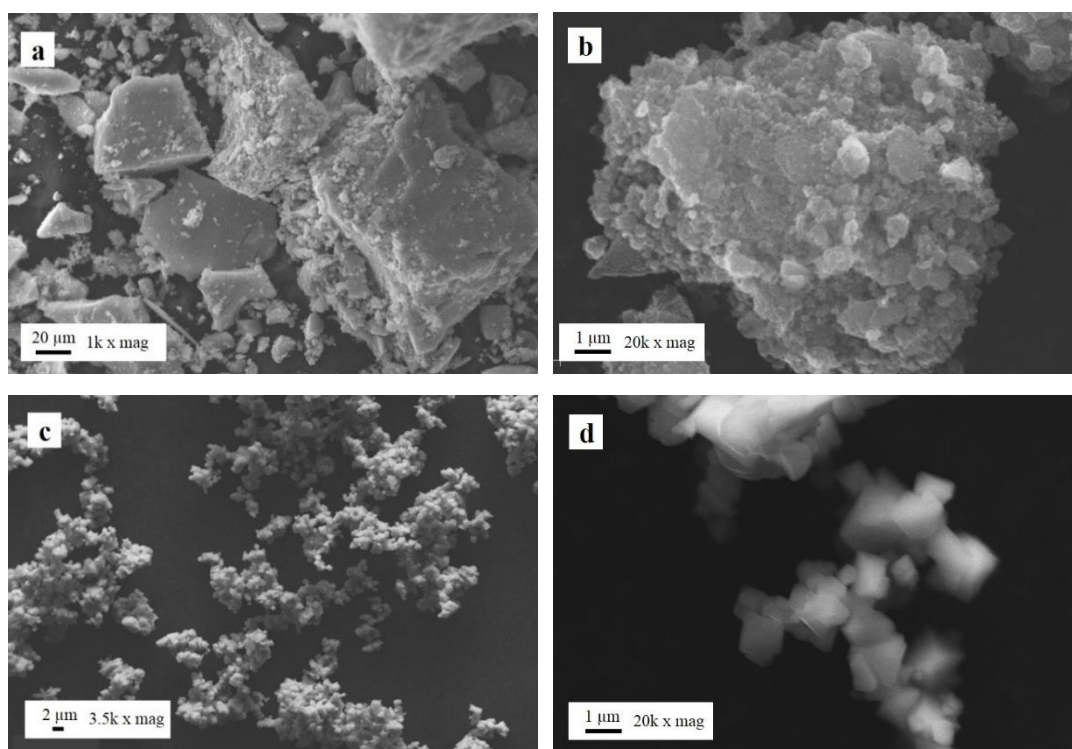


Figure 3.7 – SEM micrographs of G30-300-1-o at (a) 1k x mag and (b) 20k x mag, and commercial  $\text{Co}_3\text{O}_4$  at (c) 3.5k x mag and (d) 20k x mag

The TPR profiles of the catalysts are presented in Figure 3.8. Two main reduction peaks were observed for the samples calcined at 300°C. This two-step profile is commonly reported for the reduction of  $\text{Co}_3\text{O}_4$  to metallic Co *via*  $\text{CoO}^{13}$ , with the low temperature peak corresponding to the reduction of  $\text{Co}^{3+}$  to  $\text{Co}^{2+}$  (labelled as peak I in Figure 3.8), and the high temperature peak corresponding to the reduction of  $\text{Co}^{2+}$  to  $\text{Co}^0$  (peak II). Closer inspection of the profiles revealed the presence of a shoulder on the high temperature peak (peak III), which was more noticeable for the catalysts calcined at 400°C. For the 500°C catalysts, the high temperature peak was split into two well resolved peaks and a further shoulder peak (peak IV). For all reduction profiles in Figure 3.8, the ratio of the area of the low temperature peak to the combined areas of the high temperature peaks was approximately 1:3. This is consistent with the theoretical hydrogen consumption ratio based on the following equations, and therefore suggests that peaks II, III and IV were all due to the reduction of CoO:



The reduction peaks were shifted to higher temperatures with increasing catalyst calcination temperature. The dependence of reduction temperature on crystallite size has been reported previously for unsupported  $\text{Co}_3\text{O}_4^{15}$ . The reduction of the 300°C catalysts (11 nm crystallite size) at lower temperatures than the 500°C catalysts (47 nm crystallite size) can be explained by diffusion limitation with increasing size and the facilitation of reduction in smaller crystallites due to the presence of more structural defects<sup>20</sup>. It should also be noted that all peaks of the G30 samples appeared at temperatures 10-15°C higher than those of the G10 samples at each given calcination temperature. The presence of multiple peaks for the reduction of CoO to Co may be attributed to the wide range of particle sizes which make up the catalyst samples, as

observed in the SEM images (Figure 3.7). The larger particles which consisted of aggregates of many crystallites are likely to be more difficult to reduce than smaller particles due to diffusion limitations.

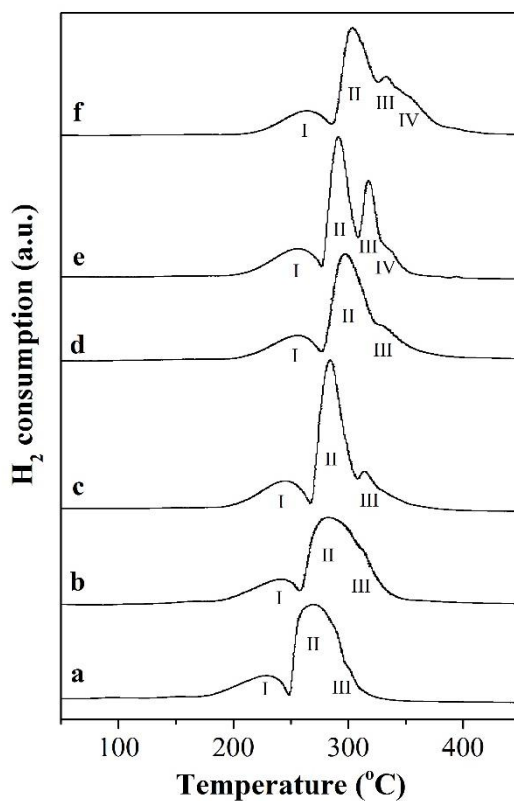


Figure 3.8 – H<sub>2</sub>-TPR profiles of (a) G10-300-1-o, (b) G30-300-1-o, (c) G10-400-1-o, (d) G30-400-1-o, (e) G10-500-1-o and (f) G30-500-1-o

The phase transformations which occurred during the reduction of G30-300-1-o were followed by in-situ XRD. Diffraction patterns (shown in Figure 3.9) were recorded at 50°C intervals as G30-300-1-o was heated from 50 to 600°C under a flow of 10% H<sub>2</sub>/Ar. Co<sub>3</sub>O<sub>4</sub> was the only phase observed until 200°C. Both Co<sub>3</sub>O<sub>4</sub> and CoO were present at 250°C, then only CoO could be detected at 300°C. This phase change from Co<sub>3</sub>O<sub>4</sub> to CoO corresponded to the low temperature TPR peak, and the existence of both phases at 250°C demonstrated that not all of the sample was reduced simultaneously, which resulted in a broad reduction peak. The reduction of CoO was observed from 350 to 550°C: the intensity of the CoO peaks decreased whilst the

intensity of the Co peaks increased. Only Co was detected at 600°C. The concurrent presence of the CoO and Co phases indicated that some parts of the sample were fully reduced to the metallic state before others, and this corroborates the assignment of peaks II, III and IV to the reduction of CoO. The occurrence of the reduction events at higher temperatures in the in-situ XRD experiment compared to the conventional TPR experiment can likely be attributed to the difference in experimental set-up; a greater mass of sample with a shallower bed-depth was utilised in the XRD experiment.

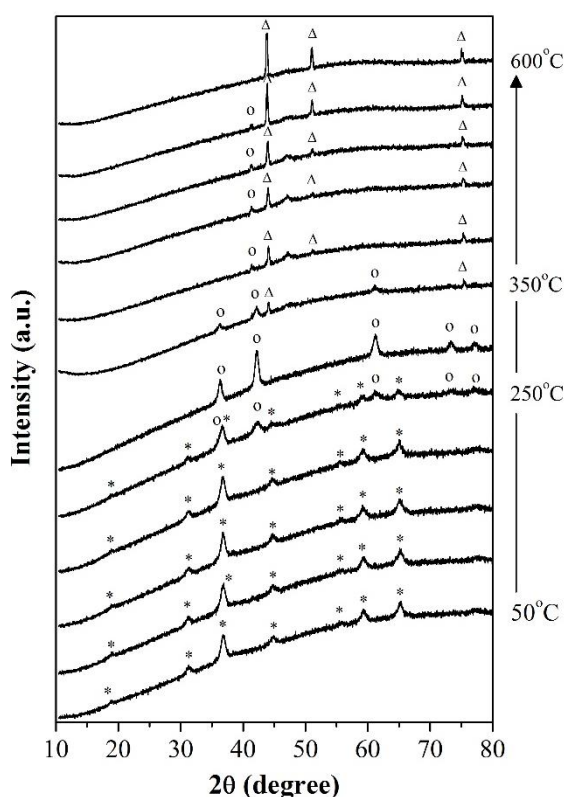


Figure 3.9 – In-situ XRD patterns of G10-300-1-o reduced in H<sub>2</sub>. Patterns were recorded at 50°C intervals. \* = Co<sub>3</sub>O<sub>4</sub>, o = CoO, Δ = Co metal

The Co 2p and O 1s regions of the XPS spectra of the catalysts are shown in Figure 3.10. For the Co 2p spectra, two main peaks separated by a spin-orbit splitting of 15 eV were observed at 779.7 and 794.7 eV, which correspond to the 2p<sub>3/2</sub> and 2p<sub>1/2</sub> levels, respectively<sup>21</sup>. The positions of these peaks, together with the presence of low intensity satellites centred at 790 and 805 eV, are indicative of Co<sub>3</sub>O<sub>4</sub><sup>21</sup>. No major

differences were observed between the binding energies or the peak profiles of any of the samples, which suggests that in each sample the Co atoms were in a similar local environment<sup>22</sup>. The asymmetry of the two main peaks is attributed to contributions from  $\text{Co}^{2+}$  and  $\text{Co}^{3+}$  ions<sup>22</sup>. In the O 1s spectra, two peaks were observed at 529.8 and 531.5 eV. These peaks have previously been identified as lattice  $\text{O}^{2-}$  and surface  $\text{O}^-$  species, respectively<sup>22</sup>. As for the Co spectra, no notable differences were seen between the binding energies or the peak profiles of the O 1s spectra.

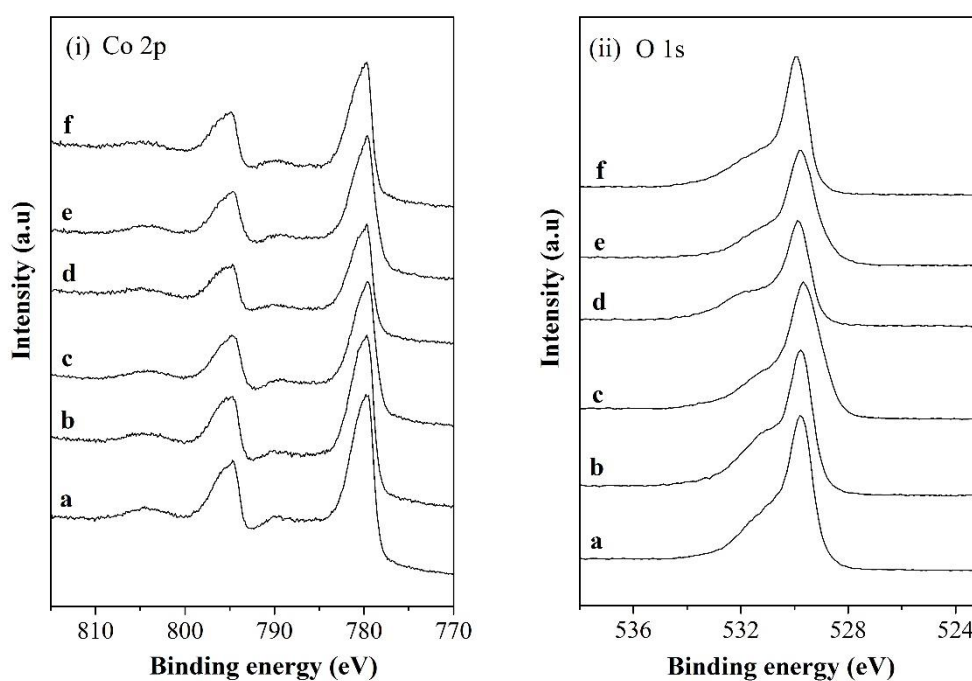
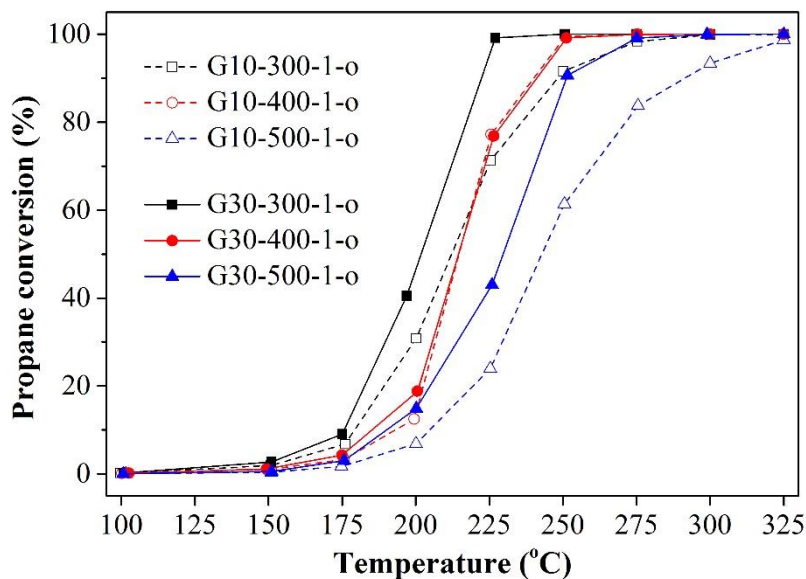
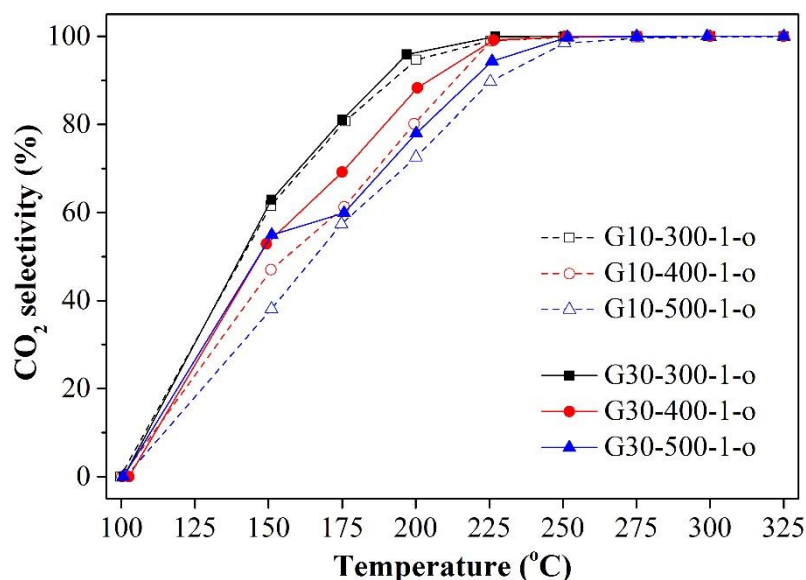


Figure 3.10 – XPS spectra of (i) Co 2p region and (ii) O 1s region: (a) G10-300-1-o, (b) G30-300-1-o, (c) G10-400-1-o, (d) G30-400-1-o, (e) G10-500-1-o and (f) G30-500-1-o

The activity of each catalyst for the total oxidation of propane is shown in Figure 3.11. In all cases, 100% conversion of propane was achieved by approximately 325°C. Comparison of the temperatures at which 10, 50 and 90% propane conversions were achieved (reported in Table 3.3) revealed that the most active catalyst was G30-300-1-o whilst the least active catalyst was G10-500-1, as these samples displayed the lowest and highest temperatures required for the conversions,

respectively. The activity observed for G30-300-1-o was comparable to that of a sample prepared in a similar way and tested for the total oxidation of propane under similar conditions<sup>14</sup>. For the G30 catalysts, a clear trend was observed, with catalysts becoming less active with increasing calcination temperature; the  $T_{50}$  for this series increased from 202°C to 215°C to 230°C. For the G10 catalysts, similar activities were observed for the samples calcined at 300 and 400°C ( $T_{50} \sim 215^\circ\text{C}$ ), but the sample calcined at 500°C was considerably less active ( $T_{50} = 243^\circ\text{C}$ ). The G30 catalysts were more active than the G10 catalysts at each calcination temperature except 400°C, where very little difference in activity was observed between the two samples.

Figure 3.11 – Propane conversion over  $\text{Co}_3\text{O}_4$  catalystsFigure 3.12 –  $\text{CO}_2$  selectivity over  $\text{Co}_3\text{O}_4$  catalysts

The selectivity of each catalyst towards  $\text{CO}_2$ , the desired total oxidation product, is shown in Figure 3.12. At low propane conversions, all catalysts were found to produce propene by partial oxidation, however  $\text{CO}_2$  was the predominant product following catalyst light-off, as observed previously for  $\text{Co}_3\text{O}_4$  under similar reaction conditions<sup>23</sup>. No other reaction products were observed.

Table 3.3 – Catalytic activity

Sample	T <sub>10</sub> (°C)	T <sub>50</sub> (°C)	T <sub>90</sub> (°C)	Reaction rate <sup>a</sup> (mol <sub>C<sub>3</sub>H<sub>8</sub></sub> g <sub>cat</sub> <sup>-1</sup> s <sup>-1</sup> )	Specific reaction rate <sup>a</sup> (mol <sub>C<sub>3</sub>H<sub>8</sub></sub> m <sup>-2</sup> s <sup>-1</sup> )
G10-300-1-o	179	212	248	20.9 x 10 <sup>-7</sup>	1.5 x 10 <sup>-8</sup>
G10-400-1-o	193	215	240	18.2 x 10 <sup>-7</sup>	3.6 x 10 <sup>-8</sup>
G10-500-1-o	205	243	291	4.8 x 10 <sup>-7</sup>	2.2 x 10 <sup>-8</sup>
G30-300-1-o	176	202	222	25.7 x 10 <sup>-7</sup>	2.0 x 10 <sup>-8</sup>
G30-400-1-o	185	215	241	16.6 x 10 <sup>-7</sup>	3.3 x 10 <sup>-8</sup>
G30-500-1-o	190	230	251	8.2 x 10 <sup>-7</sup>	3.1 x 10 <sup>-8</sup>
Pt/Al <sub>2</sub> O <sub>3</sub>	217	283	325	10.2 x 10 <sup>-7</sup>	-
comm Co <sub>3</sub> O <sub>4</sub>	272	>325	>325	0.14 x 10 <sup>-7</sup>	1.4 x 10 <sup>-8</sup>

a – Reaction rates were calculated from propane conversion at 225°C

The rates of reaction of the catalysts at 225°C are given in Table 3.3. The highest activity per gram of catalyst was observed for G30-300-1-o, and reaction rate was seen to decrease with increasing temperature of calcination for both the G10 and G30 catalysts. In contrast, on consideration of the specific reaction rates (surface area normalised rates), similar levels of activity were observed for all samples

Surface area and crystallite size, which are generally inversely related, are considered to be important factors for the activity of unsupported Co<sub>3</sub>O<sub>4</sub> catalysts. Samples which present a high surface area and are composed of small crystallites will have a greater proportion of surface atoms relative to the total number of atoms in the sample<sup>23</sup> and hence will contain a greater number of active sites<sup>24</sup>. In addition, a greater proportion of atoms will be coordinatively unsaturated, such that high surface area samples will present more surface defects, which, as discussed below, have been linked to high activity. In this work, the most active catalyst presented the highest surface area and smallest crystallite size, and a strong link between surface area and activity was seen for the G30 catalysts. Taking into account the nominal variations between the specific

reaction rates (Table 3.3), the activity of the G30 catalysts can be considered to be strongly dependent on surface area.

Several studies have demonstrated that the total oxidation of propane by  $\text{Co}_3\text{O}_4$  occurs via a Mars-van Krevelen redox cycle<sup>25, 26</sup>: Propane reduces the catalyst surface and is itself oxidised to  $\text{CO}_2$ . The oxidizing species are considered to be  $\text{Co}^{3+}$  ions, and nucleophilic lattice oxide ions ( $\text{O}^{2-}$ ) are incorporated into the oxidation product. To complete the cycle, molecular oxygen re-oxidizes the catalyst surface. As the catalytic cycle involves reduction of the catalyst surface, the ease with which reduction occurs in  $\text{H}_2$ -TPR could be an indicator of catalytic activity<sup>23</sup>. Considering the G30 catalysts, the most active catalyst (G30-300-1-o) was reduced at the lowest temperature, whilst the least active catalyst (G30-500-1-o) displayed the highest temperature of reduction. As mentioned above, the presence of more structural defects (specifically low coordination defect lattice oxygen sites) in catalysts with smaller crystallites are thought to facilitate reduction<sup>20, 23</sup>.

The significance of structural defects for catalytic activity has also been reported by other authors. Garcia *et al.*<sup>27</sup> suggested that a high  $\text{Co}^{2+}/\text{Co}^{3+}$  ratio (*i.e.* a greater proportion of  $\text{Co}^{2+}$  ions), as evidenced by XPS, indicates the presence of oxygen defects, and high activity for propane total oxidation was linked to a high concentration of oxygen defects. The observation of lattice strain in the XRD patterns of  $\text{Co}_3\text{O}_4$ , which is indicative of structural defects, has been related to increased activity<sup>13, 14</sup>. A further feature suggested to influence activity is the ease with which the catalyst is re-oxidised<sup>26</sup>. In a mechanistic study of propane oxidation over gold-containing and gold-free  $\text{Co}_3\text{O}_4$ , the catalysts were observed to exhibit similar

reduction behaviour, hence the higher activity of the gold-containing sample was attributed to a higher rate of re-oxidation. A higher concentration of oxygen defects was determined to be responsible for the faster re-oxidation and consequently the higher activity. In this work no differences between the XPS or XRD data of the G30 samples were observed, however for these catalysts differences in surface area seem to be the significant factor in determining activity.

The trend observed for the G30 catalysts of decreasing catalytic activity with increasing calcination temperature was not seen for the G10 catalysts; the G10 catalysts calcined at 300 and 400°C displayed similar levels of activity despite differences in characteristics, whilst calcination at 500°C gave the least active catalyst as expected from the lowest surface area, largest average crystallite size and highest temperature of reduction of the series. A number of studies have previously found that activity cannot always be correlated with characteristics such as surface area, crystallite size and reducibility by hydrogen<sup>13, 24, 28</sup>, which indicates that other factors contribute to activity.

When the G10 and G30 samples are contrasted, the higher activity of the G30 catalysts calcined at 300 and 500°C is unexpected based on the majority of the characterisation data. The duration for which the starting materials were ground was found to influence the composition of the cobalt hydroxycarbonate hydrate precursors, but few differences between the calcined materials were apparent at each calcination temperature. Based on data from XRD, N<sub>2</sub> physisorption, TPR and XPS, an activity similar to or greater than the G30 catalysts would be expected for the G10 catalysts. The only difference which could account for the lower activity of the G10 catalysts

was observed in FT-IR spectroscopy; the strength of the  $\text{Co}^{3+}\text{-O}$  bond was observed to be slightly weaker in the G30 catalysts calcined at 300 and 500°C compared to the G10 catalysts. This may suggest that the surface of G30 catalysts could be more easily reduced in the catalytic cycle. Although this does not concur with  $\text{H}_2\text{-TPR}$  data (Figure 3.8), where the G10 catalysts were observed to reduce at temperatures 10-15°C lower than the G30 catalysts, the reduction of metal oxides has been shown to occur by a different process when propane is used as the reductant rather than hydrogen<sup>29</sup>. Additionally, FT-IR is a surface sensitive technique, whereas TPR investigates bulk properties of the catalysts.

Within the G30 series, the effect on activity of the decreasing strength of the Co-O bond with increasing calcination temperature (see Table 3.2) is likely to be outweighed by the decrease in surface area and increase in crystallite size. However, when comparing samples calcined at the same temperature which present similar surface areas and crystallite sizes (G10-300-1-o vs G30-300-1-o, and G10-500-1-o vs G30-500-1-o), the weaker bond results in a higher activity. The link between the strength of this bond and activity for catalysts with comparable crystallite sizes and surface areas is corroborated by the similar activity ( $T_{50} = 215^\circ\text{C}$ ) and bond strength (band at  $558\text{ cm}^{-1}$ ) observed for the catalysts calcined at 400°C. Based on this argument, the similar activity displayed by the G10 samples calcined at 300 and 400°C could be rationalised by the relatively strong Co-O bond strength but high surface area of G10-300-1-o resulting in a similar activity for G10-400-1-o, which displayed a weaker Co-O bond but lower surface area.

The light-off activity of G30-300-1-o (the most active prepared catalyst) was compared to two commercial catalysts – the commercial  $\text{Co}_3\text{O}_4$  sample from Sigma Aldrich discussed above and a 5 wt.%  $\text{Pt}/\text{Al}_2\text{O}_3$  sample, which is known to exhibit high activity for the total oxidation of propane<sup>30</sup>. Figure 3.13 shows the conversion of propane and Figure 3.14 shows the selectivity to  $\text{CO}_2$ . Both of the commercial catalysts were far less active than the mechanochemical sample at low temperatures and 10% conversion was not observed for the Pt sample until 217°C. The Pt catalyst displayed a selectivity to  $\text{CO}_2$  of greater than 99% at all temperatures, nonetheless light-off occurred at a temperature approximately 80°C higher than for G30-300-1-o and 100% conversion of propane was still not achieved by 325°C. The commercial cobalt oxide displayed the lowest catalytic activity in this work, with a maximum propane conversion of *ca.* 30% observed at 325°C. The low activity is likely due to the very low surface area of the sample ( $1 \text{ m}^2 \text{ g}^{-1}$ ), as the specific reaction rate was comparable to the catalysts prepared by grinding (Table 3.3). Additionally, the ordered structure of the commercial catalyst, as evidenced by SEM and XRD experiments, may have contributed to the low activity.

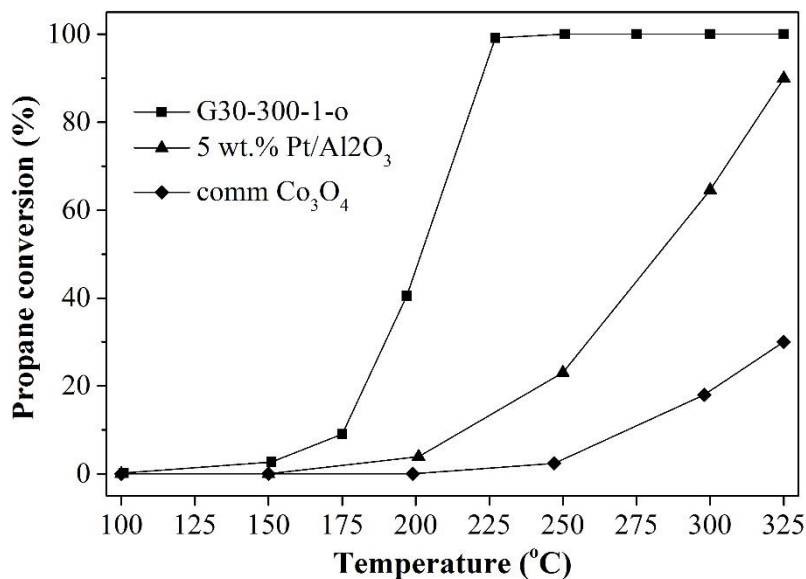
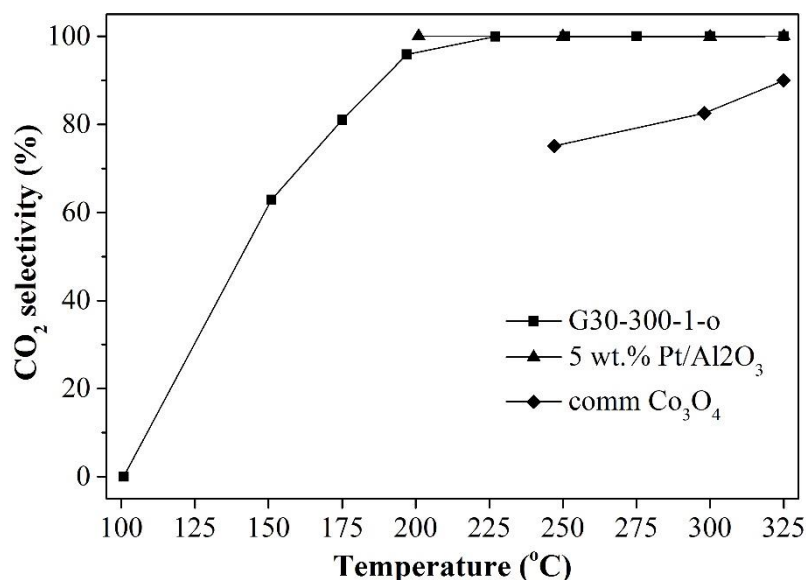


Figure 3.13 – Comparison of propane conversion over commercial catalysts

Figure 3.14 – Comparison of CO<sub>2</sub> selectivity over commercial catalysts

The stability of G30-300-1-o with time-on-line was investigated at a reaction temperature of 215°C and the results are shown in Figure 3.15. Throughout the experiment the conversion of propane remained relatively constant at an average of 73% and the catalyst displayed a consistent selectivity to CO<sub>2</sub> of 99%. The decreases in propane conversion to *ca.* 70%, centred at hours 13 and 36, may be due to the drop in the temperature of the laboratory overnight (both occurring at around 5 am), whilst

the greatest activity of 75% observed at hour 21 can be matched to the warmest part of the day (approximately 1 pm). No deactivation was detected after 42.5 hours on-line and the observed propane conversion correlated well with that of *ca.* 76% expected from the corresponding light-off experiment (Figure 3.11).

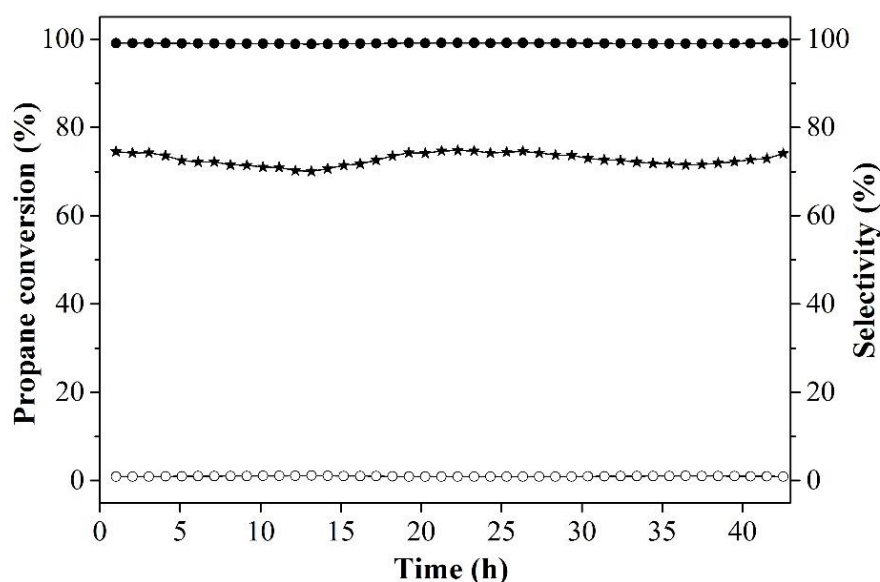


Figure 3.15 – Propane oxidation over G30-300-1-o with time-on-line at 215 °C. Star = propane conversion, filled circle = selectivity to CO<sub>2</sub>, open circle = selectivity to propene.

### 3.2.1.3 Conclusions

Cobalt hydroxycarbonate hydrates were produced by the mechanochemical reaction of cobalt nitrate and ammonium hydrogen carbonate. Calcination of these precursor materials gave rise to Co<sub>3</sub>O<sub>4</sub> catalysts which demonstrated high, stable activity for the total oxidation of propane. The most active catalyst possessed a high surface area, small average crystallite size and high reducibility, whilst the least active catalysts displayed low surface areas, large crystallite sizes and the lowest reducibility. The catalysts derived from the G30 precursor were generally more active than those derived from the G10 precursor, but the only physicochemical difference between the two series of catalysts to account for this was the strength of the Co<sup>3+</sup>-O bond. In terms of catalyst preparation, a longer duration of grinding of the starting materials

(30 minutes) and a lower calcination temperature (300°C) were found to give the most active catalyst.

### 3.2.2 Investigation of calcination atmosphere

#### 3.2.2.1 Preparation

To investigate the influence of calcination atmosphere on the properties and activity of the cobalt oxide catalysts, the G30 cobalt hydroxycarbonate hydrate precursor was calcined for 2 hours at 300°C (1°C min<sup>-1</sup>) in an atmosphere of static air (no gas flow through a sealed tubular furnace) or flowing air (50 mL min<sup>-1</sup> air flow through a sealed tubular furnace). These samples were compared to G30-300-1-o (the most active catalyst from *Section 3.2.1*) which was calcined in open air (no gas flow through an open tubular furnace). The nomenclature of the prepared samples is summarised in Table 3.4.

Table 3.4 – Sample nomenclature

Sample	Grinding time (min)	Calcination temperature (°C)	Heating rate (°C min <sup>-1</sup> )	Calcination atmosphere
G30 <sup>a</sup>	30	-	-	-
G30-300-1-o	30	300	1	open air
G30-300-1-s	30	300	1	static air
G30-300-1-f	30	300	1	flowing air

a – Uncalcined catalyst precursor

#### 3.2.2.2 Results and Discussion

XRD analysis of the catalysts (patterns shown in Figure 3.16) found that the spinel phase of cobalt oxide was formed in all cases, irrespective of the calcination atmosphere to which the G30 precursor was exposed. The average crystallite sizes are reported in Table 3.5. Whilst no difference was seen between the samples calcined under open and static air, crystallites with a slightly larger average size were formed under flowing air.

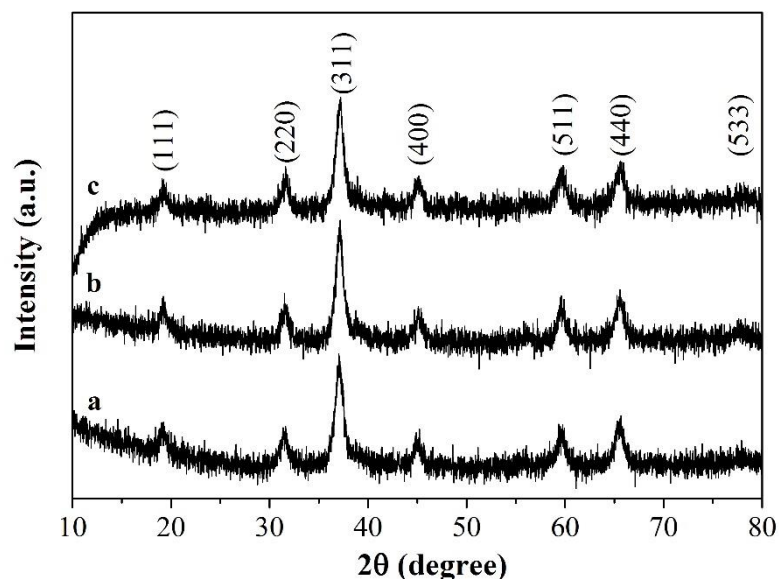


Figure 3.16 – XRD patterns of (a) G30-300-1-o, (b) G30-300-1-s and (c) G30-300-1-f

The specific surface areas of the precursor and catalysts are presented in Table 3.5. In line with the XRD data, the samples calcined under open and static air presented similar surface areas of *ca.* 125 m<sup>2</sup> g<sup>-1</sup>. A lower surface area compared to the precursor and the other catalysts was observed following calcination under flowing air, consistent with the larger crystallite size, but the difference was not significant within experimental error.

Table 3.5 – Physicochemical characteristics of precursors and catalysts

Sample	Co <sub>3</sub> O <sub>4</sub> crystallite size (nm)	Surface area (m <sup>2</sup> g <sup>-1</sup> )	Co-O IR bands (cm <sup>-1</sup> )	
			Co <sup>2+</sup>	Co <sup>3+</sup>
G30	-	123	-	-
G30-300-1-o	10	128	658	558
G30-300-1-s	10	125	658	558
G30-300-1-f	12	116	658	559

The FT-IR spectra of the catalysts were recorded and the positions at which the Co-O stretching vibrations were observed are given in Table 3.5. The band due to Co<sup>2+</sup>-O appeared for all three catalysts at 658 cm<sup>-1</sup>. The band attributed to Co<sup>3+</sup>-O was present

at  $558\text{ cm}^{-1}$  for both G30-300-1-o and G30-300-1-s, but was observed at a slightly higher wavenumber for the catalyst calcined under flowing air.

The TPR profiles of the catalysts are shown in Figure 3.17. All three catalysts presented similar profiles. The reduction peaks were present at similar temperatures for each catalyst, likely due to the similarity in average crystallite size, as reduction temperature has been shown to depend on  $\text{Co}_3\text{O}_4$  crystallite size<sup>15</sup>. As noted in *Section 3.2.1.2*, the two main reduction peaks correspond to the sequential reduction of  $\text{Co}_3\text{O}_4$  to  $\text{CoO}$  then  $\text{CoO}$  to  $\text{Co}$  metal<sup>13</sup>. The asymmetry of each high temperature peak is again attributed to the reduction of  $\text{CoO}$  particles of a range of sizes.

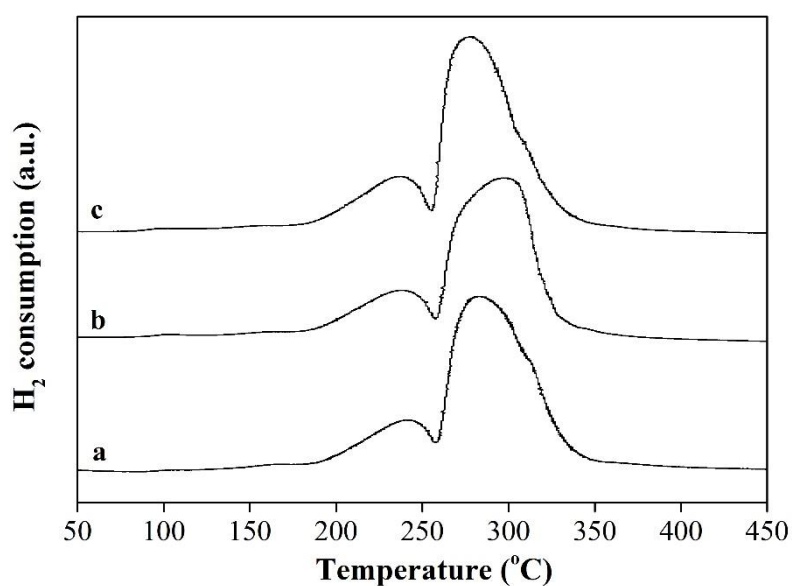


Figure 3.17 –  $\text{H}_2$ -TPR profiles of (a) G30-300-1-o, (b) G30-300-1-s and (c) G30-300-1-f

Figure 3.18 shows the  $\text{Co } 2p$  and  $\text{O } 1s$  XPS spectra of the catalysts. No differences in binding energy or profile shape were observed between the spectra of the catalysts calcined under different air atmospheres; the  $\text{Co } 2p$  spectra were indicative of  $\text{Co}_3\text{O}_4$ <sup>21</sup> and the  $\text{O } 1s$  spectra revealed the presence of lattice  $\text{O}^{2-}$  and surface  $\text{O}^-$  species<sup>22</sup>.

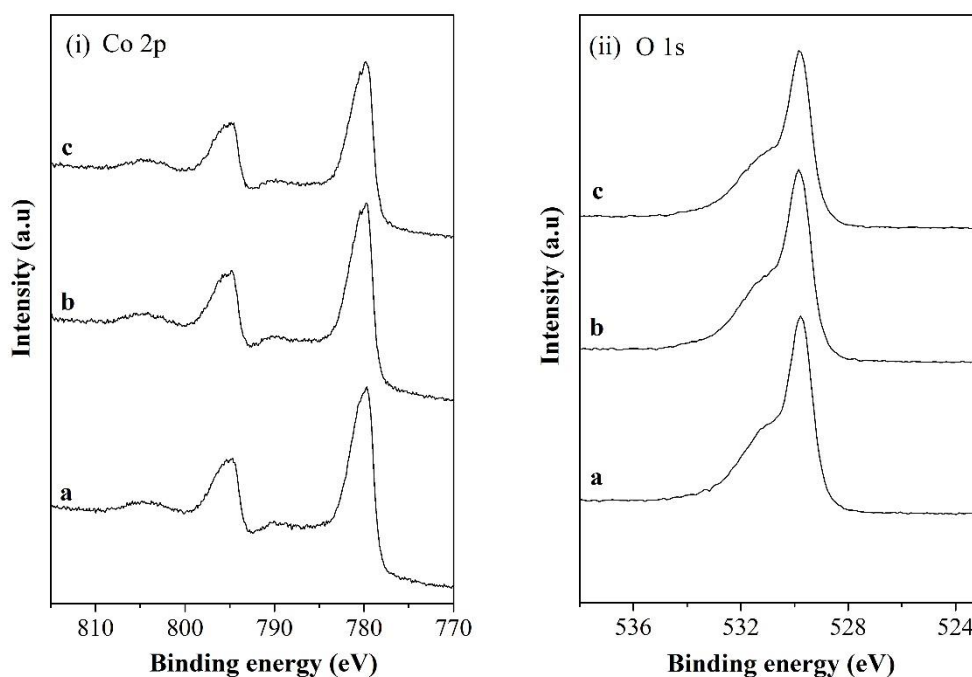
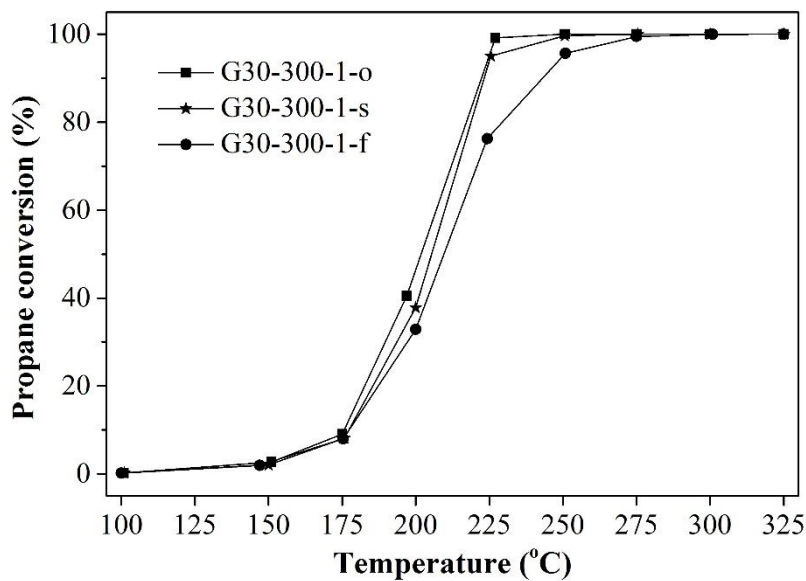
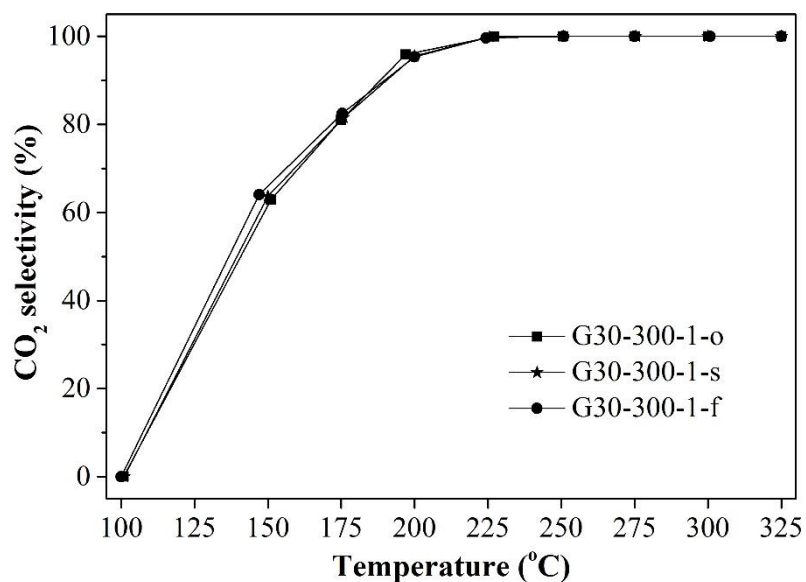


Figure 3.18 – XPS spectra of (i) Co 2p region and (ii) O 1s region:  
 (a) G30-300-1-o, (b) G30-300-1-s and (c) G30-300-1-f

The activity of the catalysts for the total oxidation of propane is shown in Figure 3.19. Comparison of the temperatures at which 10 and 50% propane conversions were achieved (reported in Table 3.6) revealed only small differences between the catalysts. The catalyst calcined under flowing air required the highest temperature for 90% conversion, but G30-300-1-o and G30-300-1-s continued to display a similar activity across all reaction temperatures and achieved 90% conversion at a temperature *ca.* 20°C lower than G30-300-1-f.

Figure 3.19 – Propane conversion over Co<sub>3</sub>O<sub>4</sub> catalystsFigure 3.20 – CO<sub>2</sub> selectivity over Co<sub>3</sub>O<sub>4</sub> catalysts

The selectivity of the catalysts towards CO<sub>2</sub> is shown in Figure 3.20. As observed for the samples in *Section 3.2.1.2*, propene was produced over the catalysts at low propane conversions, and selectivity to CO<sub>2</sub> increased with conversion. No other reaction products were observed.

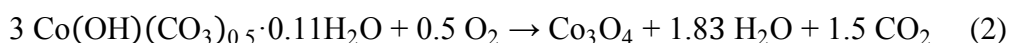
Table 3.6 – Catalytic activity

Sample	T <sub>10</sub> (°C)	T <sub>50</sub> (°C)	T <sub>90</sub> (°C)	Reaction rate <sup>a</sup> (mol <sub>C<sub>3</sub>H<sub>8</sub></sub> g <sub>cat</sub> <sup>-1</sup> s <sup>-1</sup> )	Specific reaction rate <sup>a</sup> (mol <sub>C<sub>3</sub>H<sub>8</sub></sub> m <sup>-2</sup> s <sup>-1</sup> )
G30-300-1-o	176	202	222	25.7 x 10 <sup>-7</sup>	2.0 x 10 <sup>-8</sup>
G30-300-1-s	177	205	223	25.1 x 10 <sup>-7</sup>	2.0 x 10 <sup>-8</sup>
G30-300-1-f	177	209	243	20.4 x 10 <sup>-7</sup>	1.8 x 10 <sup>-8</sup>

a – Reaction rates were calculated from propane conversion at 225°C

The rates of reaction of the catalysts at 225°C are given in Table 3.6. The samples calcined under open and static air displayed very similar rates per gram of catalyst, but lower activity was observed for the sample calcined under flowing air. In contrast, every catalyst presented a similar specific rate of reaction.

Variations between the catalysts calcined under open and static air were seen to be minimal. Differences between the two catalysts were initially expected due to the differences in experimental set-up; gases could freely diffuse with the external laboratory atmosphere during the open air calcination, but for the static air calcination, as the furnace was sealed, it was anticipated that the oxygen concentration may deplete below the level necessary to form stoichiometric Co<sub>3</sub>O<sub>4</sub> or the decomposition products may alter the catalyst properties. Nonetheless, the similarities observed for the two catalysts can be rationalised by the relatively small mass of precursor (*ca.* 1 g) used in each experiment. As only a small amount of oxygen would have been required to form stoichiometric Co<sub>3</sub>O<sub>4</sub> (calculated to be 0.0015 moles based on Equation 2), the initial volume of air in the calcination tube would have provided sufficient oxygen (initial number of moles of O<sub>2</sub> calculated to be 0.0054 moles).



Additionally, the decomposition products most likely exited through the furnace vent. It is possible that differences between the catalysts may have been observed if the experiments were performed on a larger scale.

In contrast, calcination of the G30 precursor under flowing air was found to give a catalyst with slightly different physicochemical properties which resulted in lower catalytic activity. An increase in crystallite size and reduction in surface area has been reported previously for  $\text{Co}_3\text{O}_4$  catalysts calcined in flowing air compared to those calcined in static air<sup>31</sup>. It was suggested that the flowing air would provide a high concentration of oxygen which could facilitate exothermic combustion events and subsequently promote crystallite growth<sup>31</sup>. The exothermic reaction in this case is the oxidation of  $\text{Co}^{2+}$  ions of the cobalt hydroxycarbonate hydrate precursor to  $\text{Co}^{3+}$  to form  $\text{Co}_3\text{O}_4$ .

The lower surface area and larger average crystallite size of the G30-300-1-f catalyst, which would result in a less defective surface with a smaller number of active sites, could account for the lower activity observed for this sample compared to the other catalysts. In addition, the stronger  $\text{Co}^{3+}$ -O bond would make reduction of the G30-300-1-f catalyst surface less facile and inhibit the rate at which the Mars-van Krevelen cycle could proceed. The small variations between the physicochemical properties of the catalysts correlate with the small differences observed in catalytic activity.

### ***3.2.2.3 Conclusions***

Calcination of the cobalt hydroxycarbonate hydrate precursor under different air atmospheres gave rise only to the spinel phase of cobalt oxide in all cases. Catalysts formed under open and static air were found to be more active than a catalyst formed under flowing air due to their higher surface area, smaller average crystallite size and lower Co-O bond strength.

### 3.2.3 *Ball milling*

To investigate the possibility of producing  $\text{Co}_3\text{O}_4$  catalysts which demonstrated a higher activity for the total oxidation of propane, mechanochemical synthesis of cobalt nitrate and ammonium hydrogen carbonate using a ball mill was attempted (as grinding for longer than 30 minutes could not realistically be performed using a pestle and mortar). As mentioned in *Section 3.2.1.2*, a previous study has shown that a distorted unit cell (indicative of a higher concentration of defects) could be created by extended grinding, which in turn resulted in greater activity for propane total oxidation<sup>13</sup>. In the study citric acid and a cobalt hydroxycarbonate hydrate were ground together in a planetary ball mill for up to six hours to give a cobalt citrate precursor and subsequent calcination gave the cobalt oxide catalyst<sup>13</sup>.  $\text{Co}_3\text{O}_4$  has previously been synthesised from cobalt nitrate and ammonium hydrogen carbonate using a planetary ball mill, but only one sample was synthesised, so no conclusions could be drawn regarding the influence of grinding duration on catalyst properties<sup>32</sup>.

In this work, a number of experiments were performed using a roller ball mill (Pascall Engineering), a 568 mL capacity tin-plated aluminium container (8.5 cm o.d.) and several different grinding media. In initial experiments, various masses of cobalt nitrate and ammonium hydrogen carbonate, always in a 2:5 molar ratio, and 100 stainless steel ball bearings of 1/4" diameter were loaded into the milling container. Irrespective of the total mass of starting materials used, the container had to be vented at regular intervals due to the build-up of pressure caused by the production of carbon dioxide and ammonia meaning that continuous grinding was not possible.

An opening was made in the lid of the container to allow gases to escape and further experiments were performed. Whilst the problem of pressure build up was circumvented, a new issue was encountered whereby the ball bearing became stuck in the viscous reaction mixture on the walls of the container after several minutes of grinding. Evidently, venting the container during the initial experiments had dislodged the ball bearings from the reaction mixture, enabling extended grinding to be performed.

A number of additional experiments were performed in which the total mass of starting materials, the number and size of ball bearings (up to  $\frac{3}{4}$ "") and the speed of rotation of the mill were varied systematically. In all cases, the grinding media eventually became embedded in the reaction mixture, meaning catalysts could not be synthesised by extended grinding.

Future work on the mechanochemical reaction of these starting materials in the roller ball mill could focus on the addition of grinding aids such as diluents or small amounts of solvent to reduce the viscosity of the reaction mixture.

### **3.3 Reaction of cobalt nitrate and alternative bases**

#### ***3.3.1 Preparation***

To investigate the mechanochemical synthesis of  $\text{Co}_3\text{O}_4$  using alternative bases to ammonium hydrogen carbonate, cobalt nitrate (15.0 g) and either sodium hydrogen carbonate (10.8 g), ammonium carbonate (12.4 g) or sodium carbonate (13.7 g) were ground together on a 2:5 molar ratio for 30 minutes according to the method described in *Section 2.1.1.1*. The precursors were calcined for 2 hours at  $300^\circ\text{C}$  ( $1^\circ\text{C min}^{-1}$ ) in

open air. These samples were compared to G30-300-1-o (the most active sample from *Section 3.2.1*), which was prepared from cobalt nitrate (15.0 g) and ammonium hydrogen carbonate (10.2 g). The nomenclature of the prepared samples is summarised in Table 3.7.

Table 3.7 – Sample nomenclature

Sample	Base	Grinding time (min)	Calcination conditions
G30 <sup>a</sup> G30-300-1-o	NH <sub>4</sub> HCO <sub>3</sub>	30	- 300°C / 1°C min <sup>-1</sup> / open air
G30-NaHCO <sub>3</sub> <sup>a</sup> G30-NaHCO <sub>3</sub> -300-1	NaHCO <sub>3</sub>	30	- 300°C / 1°C min <sup>-1</sup> / open air
G30-(NH <sub>4</sub> ) <sub>2</sub> CO <sub>3</sub> <sup>a</sup> G30-(NH <sub>4</sub> ) <sub>2</sub> CO <sub>3</sub> -300-1	(NH <sub>4</sub> ) <sub>2</sub> CO <sub>3</sub>	30	- 300°C / 1°C min <sup>-1</sup> / open air
G30-Na <sub>2</sub> CO <sub>3</sub> <sup>a</sup> G30-Na <sub>2</sub> CO <sub>3</sub> -300-1	Na <sub>2</sub> CO <sub>3</sub>	30	- 300°C / 1°C min <sup>-1</sup> / open air

a – Uncalcined catalyst precursors

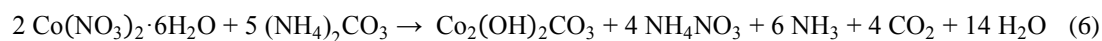
As noted in *Section 3.2.1.2*, the ammonium hydrogen carbonate reaction mixture quickly became wet and viscous and turned a berry purple colour. Whilst characterisation indicated that the formed precursor was hydrated rather than anhydrous cobalt hydroxycarbonate, Equation 1 gives a good indication of the relative number of moles of the products formed in the reaction:



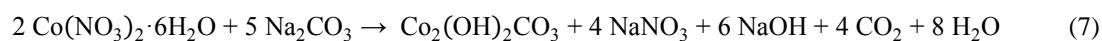
When sodium hydrogen carbonate was reacted, the reaction mixture turned the same berry purple colour, but was not as wet as the ammonium hydrogen carbonate mixture, meaning grinding was slightly less facile. The drier reaction mixture was expected based on the fewer number of moles of water produced in the reaction, as shown in Equation 5:



Ammonium carbonate (Equation 6) also gave a drier reaction mixture, which is likely due to the greater mass of ammonium carbonate required for a 2:5 molar ratio with the cobalt nitrate.



The sodium carbonate reaction mixture remained completely dry for the first 15 minutes of grinding, and by 30 minutes the mixture was only slightly wet. The lack of water in the mixture was expected as this reaction produced the fewest number of moles of water (based on Equation 7) and required the greatest mass of base for a 2:5 molar ratio.



### 3.3.2 Results and Discussion

The XRD patterns of the precursors (shown in Figure 3.21) indicated that the reaction of cobalt nitrate with each of the different bases gave rise to poorly crystalline cobalt hydroxycarbonate hydrate<sup>2</sup>.

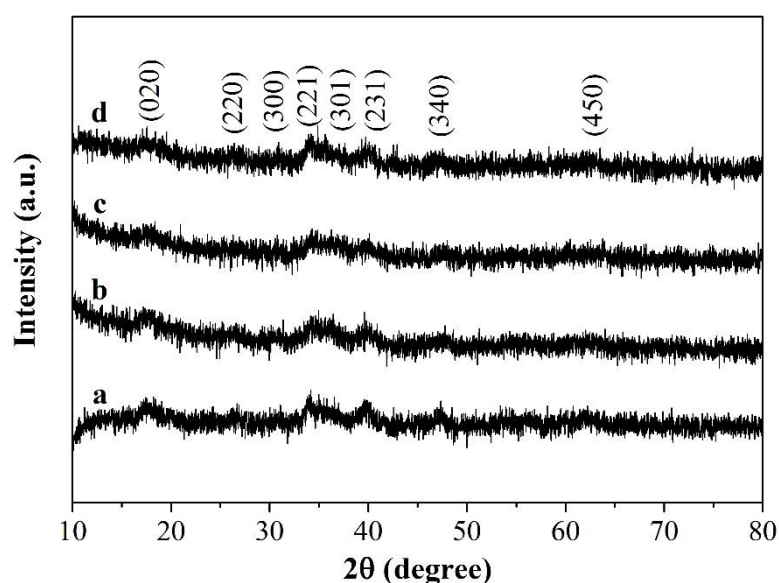


Figure 3.21 – XRD patterns of (a) G30, (b) G30-NaHCO<sub>3</sub>, (c) G30-(NH<sub>4</sub>)<sub>2</sub>CO<sub>3</sub> and (d) G30-Na<sub>2</sub>CO<sub>3</sub>

The FT-IR spectra of the precursors (not shown) revealed bands relating to carbonate anions, water and/or hydroxyl anions and Co-OH, as described for the precursors in *Section 3.2.1.2*. The bands were present at identical positions in the spectra, again indicating that hydrated cobalt hydroxycarbonate was formed by reaction of cobalt nitrate with each of the bases.

The TGA-DTA curves of each precursor are shown in Figure 3.22. Similar profiles were observed for all samples, corresponding to the decomposition of hydrated cobalt hydroxycarbonate to  $\text{Co}_3\text{O}_4$ , as described for the precursors in *Section 3.2.1.2*. The small shoulder seen for G30 at 230°C, due to a “high temperature carbonate” species<sup>10</sup>, was not observed for any of the other samples. Overall, the TGA indicated that calcination of all four of the precursors at 300°C would give rise to cobalt oxide.

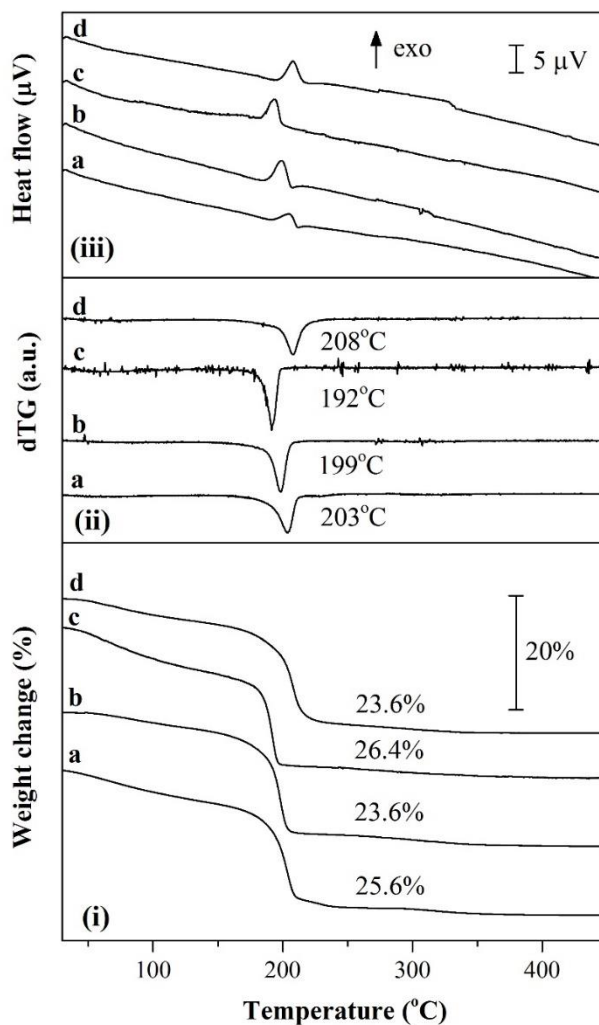


Figure 3.22 – (i) TGA, (ii) dTG and (iii) DTA curves of (a) G30, (b) G30-NaHCO<sub>3</sub>, (c) G30-(NH<sub>4</sub>)<sub>2</sub>CO<sub>3</sub> and (d) G30-Na<sub>2</sub>CO<sub>3</sub>. Experiments were performed at 1°C min<sup>-1</sup>

The precursors were calcined at 300°C (1°C min<sup>-1</sup>) for 2 hours under open air and the XRD patterns of these materials are shown in Figure 3.23. Only diffraction peaks corresponding to Co<sub>3</sub>O<sub>4</sub> were observed for each catalyst, hence complete conversion to the oxide was assumed. The pattern of G30-(NH<sub>4</sub>)<sub>2</sub>CO<sub>3</sub>-300-1 (Figure 3.23c) presented peaks which were slightly narrower and of higher intensities than those of the other catalysts, indicating that this sample was more crystalline. Calculation of average crystallite sizes using the Scherrer equation (values given in Table 3.8) found that the catalysts prepared from ammonium hydrogen carbonate, sodium hydrogen carbonate and sodium carbonate consisted of crystallites of approximately 10 nm in

size, but the ammonium carbonate-derived sample presented larger crystallites of 15 nm in size. A correlation was observed between the crystallite sizes of the catalysts and the temperatures at which the precursors transformed into  $\text{Co}_3\text{O}_4$ . Based on the first derivatives of the TGA curves shown in Figure 3.22(ii),  $\text{G30}-(\text{NH}_4)_2\text{CO}_3$  began the transition to  $\text{Co}_3\text{O}_4$  at the lowest temperature ( $192^\circ\text{C}$ ) and displayed the largest crystallite size (15 nm), whilst  $\text{G30}-\text{Na}_2\text{CO}_3$  required the highest temperature for conversion ( $208^\circ\text{C}$ ) and displayed the smallest crystallite size (9 nm). Transformation of the precursor at a lower temperature would result in a longer aging time for the  $\text{Co}_3\text{O}_4$  catalyst during the calcination and hence a greater degree of crystallite growth could occur.

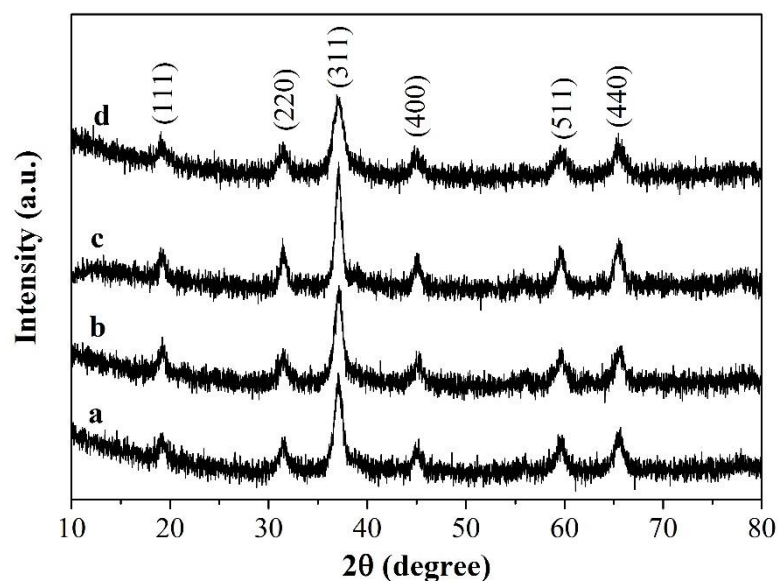


Figure 3.23 – XRD patterns of (a)  $\text{G30}-300-1-\text{o}$ , (b)  $\text{G30}-\text{NaHCO}_3-300-1$ , (c)  $\text{G30}-(\text{NH}_4)_2\text{CO}_3-300-1$  and (d)  $\text{G30}-\text{Na}_2\text{CO}_3-300-1$

Table 3.8 – Physicochemical characteristics of precursors and catalysts

Sample	$\text{Co}_3\text{O}_4$ crystallite size (nm)	Surface area ( $\text{m}^2 \text{g}^{-1}$ )		Co-O IR bands ( $\text{cm}^{-1}$ )	
		Precursor	Catalyst	$\text{Co}^{2+}$	$\text{Co}^{2+}$
$\text{G30}-300-1-\text{o}$	10	123	128	658	558
$\text{G30}-\text{NaHCO}_3-300-1$	11	148	131	658	559
$\text{G30}-(\text{NH}_4)_2\text{CO}_3-300-1$	15	142	92	658	558
$\text{G30}-\text{Na}_2\text{CO}_3-300-1$	9	130	108	658	558

The BET specific surface areas of the precursors and catalysts are reported in Table 3.8. All four precursors exhibited relatively high surface areas ranging between *ca.* 120-150 m<sup>2</sup> g<sup>-1</sup>. The precursor with the highest surface area was synthesised from sodium hydrogen carbonate, whilst the G30 precursor, derived from ammonium hydrogen carbonate, presented the lowest surface area. However, the surface areas of the precursors did not correlate with the surface areas observed for the final catalysts, *i.e.* despite a difference in surface area of 25 m<sup>2</sup> g<sup>-1</sup> between G30-NaHCO<sub>3</sub> and G30, the catalysts produced from these precursors displayed similar surface areas. With the exception of G30-300-1-o, a decrease in surface area was observed upon calcination of the precursors at 300°C. G30-(NH<sub>4</sub>)<sub>2</sub>CO<sub>3</sub>-300-1 presented the lowest surface area of 92 m<sup>2</sup> g<sup>-1</sup>, which was expected based on the large crystallite size of this catalyst (15 nm) and suggested the occurrence of crystallite growth and sintering<sup>15</sup>. G30-300-1-o and G30-NaHCO<sub>3</sub>-300-1 showed the highest surface areas of *ca.* 130 m<sup>2</sup> g<sup>-1</sup>, which could be linked with the relatively small average crystallite sizes of these samples (10-11 nm). In contrast, although the crystallite size of G30-(NH<sub>4</sub>)<sub>2</sub>CO<sub>3</sub>-300-1 was also relatively small at 9 nm, this catalyst exhibited a surface area of only 108 m<sup>2</sup> g<sup>-1</sup>. It appeared that a factor other than crystallite growth or sintering was responsible for the low surface area of this catalyst.

The FT-IR spectra of the catalysts were recorded and the positions at which the Co-O stretching vibrations were observed are given in Table 3.8. The band due to Co<sup>2+</sup>-O appeared for all four catalysts at 658 cm<sup>-1</sup>. The band attributed to Co<sup>3+</sup>-O was present at 558 cm<sup>-1</sup> for all of the catalysts except G30-NaHCO<sub>3</sub>-300-1, for which it was observed at 559 cm<sup>-1</sup>. The presence of this band at a slightly higher wavenumber for

this sample may indicate a higher strength of the Co-O bond<sup>14</sup>. No other species were observed in the FT-IR spectra of the catalysts.

SEM analysis of the catalysts prepared with alternative bases revealed that, in all cases, the morphology and wide range of particle sizes of the samples were similar to those of G30-300-1-o, which was shown in Figure 3.7. The catalysts comprised irregularly shaped particles of a very broad range of sizes, with each larger particle being an agglomeration of smaller particles.

Figure 3.24 shows the H<sub>2</sub>-TPR profiles of the catalysts. For the catalysts synthesised using alternative bases, no major differences in the reduction profiles were observed compared to G30-300-1-o, which was described previously in *Section 3.2.1.2*. The reduction of Co<sub>3</sub>O<sub>4</sub> to CoO occurred at a temperature *ca.* 6°C lower for G30-NaHCO<sub>3</sub>-300-1 and G30-(NH<sub>4</sub>)<sub>2</sub>CO<sub>3</sub>-300-1 compared to the original catalyst synthesised using ammonium hydrogen carbonate, and 25°C lower for G30-Na<sub>2</sub>CO<sub>3</sub>-300-1. The high temperature reduction step, which occurred between temperatures of 250 and 350°C, was asymmetric in all cases and shoulder peaks were apparent. As previously, this was attributed to the reduction of CoO particles of a range of sizes to Co metal.

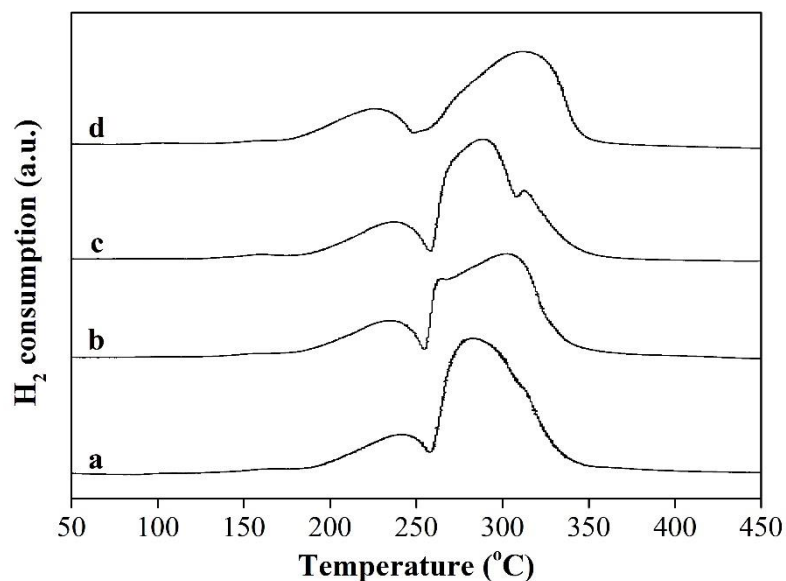


Figure 3.24 – H<sub>2</sub>-TPR profiles of (a) G30-300-1-o, (b) G30-NaHCO<sub>3</sub>-300-1, (c) G30-(NH<sub>4</sub>)<sub>2</sub>CO<sub>3</sub>-300-1 and (d) G30-Na<sub>2</sub>CO<sub>3</sub>-300-1

The XPS spectra of the catalysts were recorded and no differences in binding energy or profile shape were observed between the four catalysts in the Co 2p and O 1s regions. In the Co 2p region, two main peaks at 779.7 and 794.7 eV, and satellites centred at 790 and 805 eV, were indicative of Co<sub>3</sub>O<sub>4</sub><sup>21</sup>. In the O 1s region, peaks observed at 529.8 and 531.5 eV were attributed to lattice O<sup>2-</sup> and surface O<sup>-</sup> species, respectively<sup>22</sup>. For the G30-Na<sub>2</sub>CO<sub>3</sub>-300-1 catalyst, an extra peak at a binding energy of 1071.1 eV was attributed to the presence of sodium<sup>33</sup>. In terms of weight loading, the sodium content was equivalent to 5 wt.% Na/Co<sub>3</sub>O<sub>4</sub>. The lower than expected surface area of this catalyst may be due to the presence of sodium on the catalyst surface.

The activity of the catalysts for the total oxidation of propane is shown in Figure 3.25. All catalysts achieved 100% propane conversion by 275°C except for G30-Na<sub>2</sub>CO<sub>3</sub>-300-1, which required a temperature greater than 325°C for complete conversion. Based on the T<sub>10</sub>, T<sub>50</sub> and T<sub>90</sub> values, which are reported in Table 3.9, the

activity of the catalysts increased in the order:  $\text{G30-Na}_2\text{CO}_3\text{-300-1} < \text{G30-NaHCO}_3\text{-300-1} < \text{G30-(NH}_4)_2\text{CO}_3\text{-300-1} < \text{G30-300-1-o}$ .

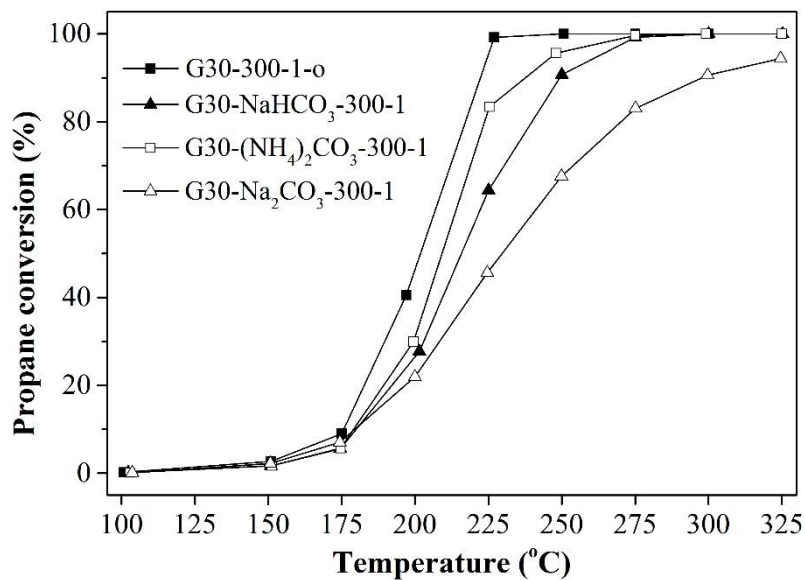


Figure 3.25 – Propane conversion over  $\text{Co}_3\text{O}_4$  catalysts

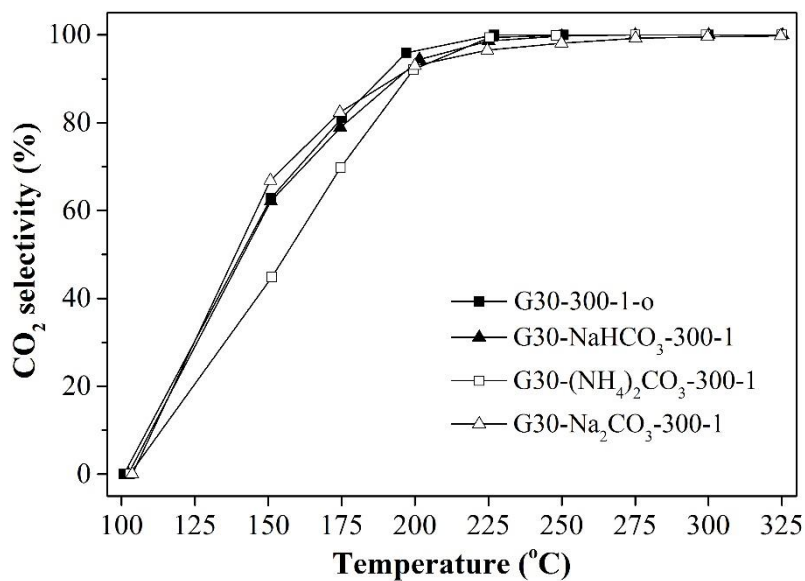


Figure 3.26 –  $\text{CO}_2$  selectivity over  $\text{Co}_3\text{O}_4$  catalysts

The selectivity of the catalysts towards  $\text{CO}_2$  is shown in Figure 3.26. Propene was produced over the catalysts at low propane conversions, and selectivity to  $\text{CO}_2$  increased with conversion. No other reaction products were observed.

Table 3.9 – Catalytic activity

Sample	T <sub>10</sub> (°C)	T <sub>50</sub> (°C)	T <sub>90</sub> (°C)	Reaction rate <sup>a</sup> (mol <sub>C<sub>3</sub>H<sub>8</sub></sub> g <sub>cat</sub> <sup>-1</sup> s <sup>-1</sup> )	Specific reaction rate <sup>a</sup> (mol <sub>C<sub>3</sub>H<sub>8</sub></sub> m <sup>-2</sup> s <sup>-1</sup> )
G30-300-1-o	176	202	222	25.7 x 10 <sup>-7</sup>	2.0 x 10 <sup>-8</sup>
G30-NaHCO <sub>3</sub> -300-1	180	216	249	17.1 x 10 <sup>-7</sup>	1.3 x 10 <sup>-8</sup>
G30-(NH <sub>4</sub> ) <sub>2</sub> CO <sub>3</sub> -300-1	179	209	239	16.6 x 10 <sup>-7</sup>	1.8 x 10 <sup>-8</sup>
G30-Na <sub>2</sub> CO <sub>3</sub> -300-1	180	230	298	10.4 x 10 <sup>-7</sup>	1.0 x 10 <sup>-8</sup>

a – Reaction rates were calculated from propane conversion at 225°C

The rates of reaction of the catalysts at 225°C are given in Table 3.9. G30-300-1-o presented the highest activity per gram of catalyst, and the lowest rate was observed for G30-Na<sub>2</sub>CO<sub>3</sub>-300-1. Intermediate rates were observed for G30-NaHCO<sub>3</sub>-300-1 and G30-(NH<sub>4</sub>)<sub>2</sub>CO<sub>3</sub>-300-1. Similar specific reaction rates were observed for all samples.

In *Sections 3.2.1 and 3.2.2*, the most active of the catalysts prepared from cobalt nitrate and ammonium hydrogen carbonate by grinding for 30 minutes were observed to have the highest surface areas and smallest crystallite sizes. Based on the surface area and XRD data presented in this section, the activity of the catalysts prepared from alternative bases would be expected to increase in the order: G30-(NH<sub>4</sub>)<sub>2</sub>CO<sub>3</sub>-300-1 < G30-Na<sub>2</sub>CO<sub>3</sub>-300-1 < G30-300-1-o ~ G30-NaHCO<sub>3</sub>-300-1. Other features of the catalysts are likely to be responsible for the differences between this expected series and the observed activity series of: G30-Na<sub>2</sub>CO<sub>3</sub>-300-1 < G30-NaHCO<sub>3</sub>-300-1 < G30-(NH<sub>4</sub>)<sub>2</sub>CO<sub>3</sub>-300-1 < G30-300-1-o.

The poor activity of G30-Na<sub>2</sub>CO<sub>3</sub>-300-1 may be attributed to the presence of sodium on the catalyst. The high level of residual sodium was likely due to the large initial mass of sodium from the carbonate (equivalent to 5.9 g Na) and the lack of water produced during the catalyst synthesis. Sodium carbonate, sodium nitrate and sodium

hydroxide, the possible sodium sources, are all highly soluble in water, but in the dry reaction mixture these compounds would have been in constant intimate contact with the synthesised precursor. A reduction in surface area (and concomitant decrease in activity) due to residual sodium from catalyst synthesis has previously been reported for a number of catalytic systems across a range reactions<sup>34-36</sup>. An increase in crystallinity with increased sodium content was also noted for the reported catalysts, but in this work similar average  $\text{Co}_3\text{O}_4$  crystallite sizes were observed for both the sodium-free and sodium-containing catalysts (Table 3.8). TGA experiments revealed that the  $\text{G30-Na}_2\text{CO}_3$  precursor decomposed at the highest temperature of all the catalysts in this series. The presence of sodium may be the reason for the delayed decomposition of the hydroxycarbonate precursor, which as discussed above is thought to be responsible for the small crystallite size of the catalyst due to the shortest time available for crystallite growth. As no sodium containing phases were observed by XRD, the contaminant was likely highly dispersed over the catalyst. The importance of extensive washing of the catalyst precursor during synthesis to remove residual sodium has been highlighted<sup>34</sup>, and one study even found that sodium content could be decreased and surface area increased by washing the calcined catalyst<sup>36</sup>. More thoroughly washing  $\text{G30-Na}_2\text{CO}_3$  before the drying step or washing  $\text{G30-Na}_2\text{CO}_3\text{-300-1}$  after calcination may improve the activity of this catalyst.

The lower than expected activity of  $\text{G30-NaHCO}_3\text{-300-1}$  may also be due to the presence of sodium on the catalyst surface, causing active sites to be blocked. Although no XPS peak relating to sodium was observed for this sample, sodium present at low levels would not necessarily be detected, especially if it were poorly dispersed<sup>37</sup>. Nonetheless, a lower mass of sodium was used in the synthesis of this

catalyst (3.0 g compared to 5.9 g for G30-Na<sub>2</sub>CO<sub>3</sub>-300-1) and the wetter reaction mixture would likely facilitate the separation of any sodium compounds from the precursor. The higher strength of the Co<sup>3+</sup>-O bond in this catalyst compared to the other catalysts in this series could more likely account for the lower observed activity. As discussed in *Section 3.2.2*, the stronger bond would make reduction of the catalyst surface less facile and inhibit the rate at which catalytic cycle could proceed.

G30-(NH<sub>4</sub>)<sub>2</sub>CO<sub>3</sub>-300-1 was expected to be the least active catalyst of the series based on its low surface area and high crystallite size. These characteristics were attributed to the low decomposition temperature of the G30-(NH<sub>4</sub>)<sub>2</sub>CO<sub>3</sub> precursor, which enabled more crystallite growth and sintering to occur during the calcination. Nevertheless, this catalyst was found to display the second highest propane oxidation activity. The sodium-free synthesis route avoided the presence of surface contaminants and the Co<sup>3+</sup>-O bond was observed to be equal in strength to that of G30-300-1-o. Comparison of G30-(NH<sub>4</sub>)<sub>2</sub>CO<sub>3</sub>-300-1 with the catalysts prepared by 30 minutes of grinding from *Section 3.2.1* revealed that the surface area, crystallite size and catalytic activity of the (NH<sub>4</sub>)<sub>2</sub>CO<sub>3</sub>-derived catalyst were all midway between the values of the G30-300-1-o and G30-400-1-o catalysts. As such, the observed activity of this catalyst was to be expected, even if its position in the activity series was not as predicted.

The G30-300-1-o catalyst displayed the highest activity for propane oxidation as expected due to its high surface area, small crystallite size, low Co<sup>3+</sup>-O bond strength and lack of surface contaminants.

### 3.3.3 Conclusions

Cobalt hydroxycarbonate hydrate was synthesised by the mechanochemical reaction of cobalt nitrate with carbonates and hydrogen carbonates of ammonium and sodium. Each of the precursors gave rise to the desired  $\text{Co}_3\text{O}_4$  catalyst upon calcination at  $300^\circ\text{C}$ . The catalysts displayed similar bulk characteristics, such as crystallite size, surface area and  $\text{H}_2$ -reducibility. Nonetheless, differences in catalytic activity were observed, which could be attributed to surface contaminants or differing strengths of the surface Co-O bonds. The importance of the catalyst surface in determining catalytic activity is highlighted. The most active catalyst was synthesised from ammonium hydrogen carbonate.

## 3.4 An alternative cobalt oxide precursor: reaction of cobalt acetate and oxalic acid

### 3.4.1 Preparation

To investigate the mechanochemical synthesis of  $\text{Co}_3\text{O}_4$  *via* an alternative precursor to cobalt hydroxycarbonate hydrate, cobalt acetate (16.5 g) and oxalic acid (8.35 g) were ground together on a 1:1 molar ratio for 30 minutes according to the method described in *Section 2.1.1.1* to give a cobalt oxalate precursor. The precursor was calcined for 2 hours at  $300^\circ\text{C}$  ( $1^\circ\text{C min}^{-1}$ ) or  $400^\circ\text{C}$  (1 or  $10^\circ\text{C min}^{-1}$ ) in open air. These samples were compared to G30-300-1-o (the most active sample from previous sections), which was prepared from cobalt nitrate and ammonium hydrogen carbonate. The total mass of starting materials used in the two different syntheses was comparable at *ca.* 25 g. The nomenclature of the prepared samples is summarised in Table 3.10.

Table 3.10 – Sample nomenclature

Sample	Grinding time (min)	Calcination conditions
G30 <sup>a</sup>	30	-
G30-300-1-o	30	300°C / 1°C min <sup>-1</sup> / open air
G30-oxalate <sup>a</sup>	30	-
G30-oxalate-300-1	30	300°C / 1°C min <sup>-1</sup> / open air
G30-oxalate-400-1	30	400°C / 1°C min <sup>-1</sup> / open air
G30-oxalate-400-10	30	400°C / 10°C min <sup>-1</sup> / open air

a – Uncalcined catalyst precursors

The starting materials were mixed on a 1:1 molar ratio in accordance with the following equation:



The mixture did not turn very wet, but grinding was facile and the smell of the evolved acetic acid could be detected as the mixture turned the characteristic pale pink colour of cobalt oxalate.

### 3.4.2 Results and Discussion

The XRD pattern of the G30-oxalate precursor is shown in Figure 3.27, with the pattern of G30 shown for comparison. For the G30-oxalate precursor, all diffraction peaks corresponded to the orthorhombic  $\beta$ -phase of cobalt oxalate dihydrate<sup>38, 39</sup> ( $\text{CoC}_2\text{O}_4 \cdot 2\text{H}_2\text{O}$ ). The main diffraction peaks were narrow and intense, indicating that the materials were synthesised with a good degree of crystallinity.

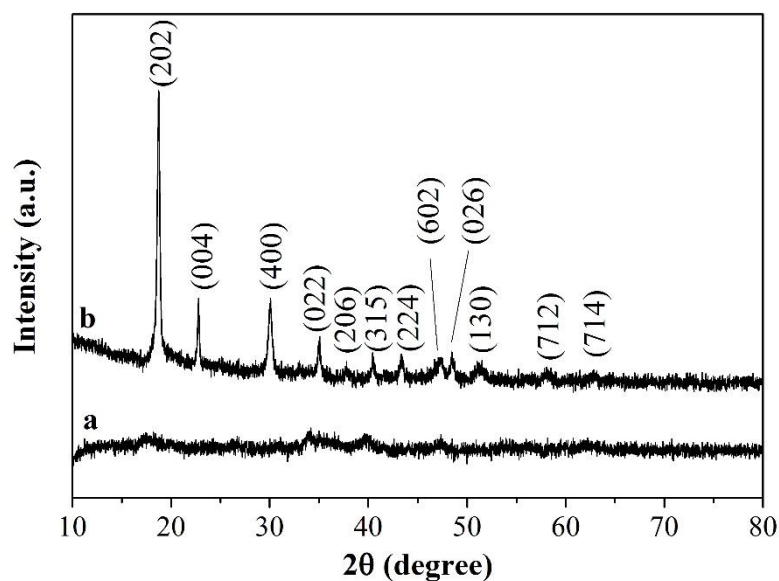


Figure 3.27 – XRD patterns of (a) G30 and (b) G30-oxalate

The FT-IR spectrum of the G30-oxalate precursor is shown in Figure 3.28. The broad band centred at  $3366\text{ cm}^{-1}$  can be attributed to water of crystallisation<sup>40</sup>. Stretching vibrations of the oxalate anion were present at  $1626\text{ cm}^{-1}$  (asymmetric (O-C-O) stretch), and  $1360$  and  $1314\text{ cm}^{-1}$  (symmetric (O-C-O) stretches)<sup>41</sup>. The positions of these stretching vibrations indicated that the oxalate ligand was bis-bidentate, *i.e.* both pairs of oxygen ions were coordinated to cobalt ions, with the oxalate ligands forming bridges between metal centres<sup>41</sup>. The band at  $825\text{ cm}^{-1}$  was attributed to oxalate (O-C-O) bending vibrations and the band at  $738\text{ cm}^{-1}$  to Co-O vibrations<sup>41, 42</sup>. Bands due to atmospheric  $\text{H}_2\text{O}$  (centred at  $3750$  and  $1675\text{ cm}^{-1}$ ) and atmospheric  $\text{CO}_2$  (centred at  $2350\text{ cm}^{-1}$ ) were also present in the spectrum<sup>6</sup>. Overall, the spectrum indicated that hydrated cobalt oxalate had been produced by grinding.

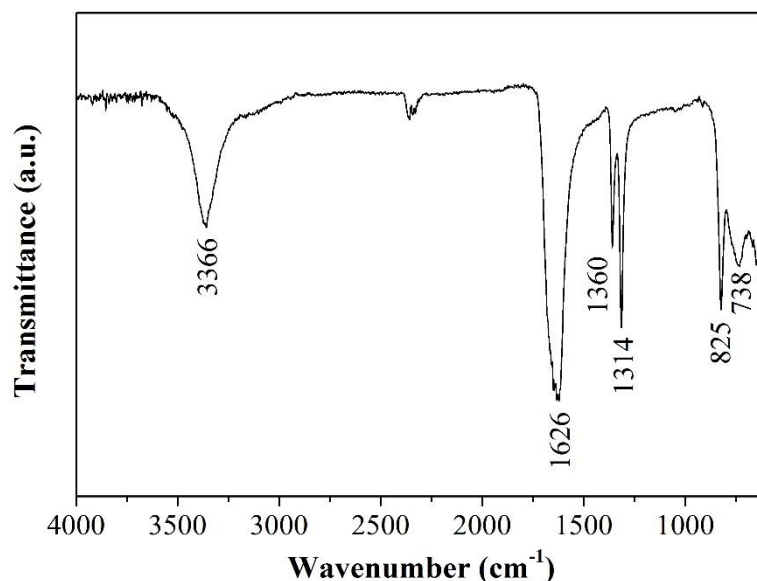
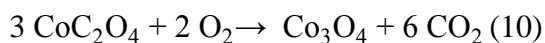


Figure 3.28 – FT-IR spectrum of G30-oxalate

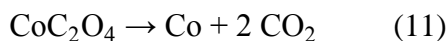
The thermal decomposition of the cobalt oxalate hydrate precursor was followed by TGA-DTA, and the curves are shown in Figure 3.29. Experiments were performed in an air atmosphere at 1 or 10°C min<sup>-1</sup>. Considering firstly the decomposition of G30-oxalate at 1°C min<sup>-1</sup> (curves (a) in Figure 3.29 (i-iii)), two main weight loss steps centred at 182 and 260°C were observed. The first step, which was accompanied by a characteristic endothermic peak, was attributed to the removal of water of crystallisation to form anhydrous cobalt oxalate<sup>40</sup>. The observed weight loss of 17.3%, which corresponded to a loss of 1.7 water molecules per formula unit, was close to the theoretical value of 19.7% for the loss of 2 molecules of water based on Equation 9:



The plateau following the loss of water represented the region in which the dehydrated cobalt oxalate was thermally stable<sup>43</sup>. The observed weight loss of 36.4% for the second step corresponded to the formation of Co<sub>3</sub>O<sub>4</sub> from anhydrous cobalt oxalate (theoretical weight loss of 36.4%) as shown in Equation 10:



Inspection of the DTG and DTA curves indicated that this step encompassed two events, which were centred at 255 and 263°C. Studies have shown that metallic cobalt and CoO are initially formed during the decomposition of cobalt oxalate, as described in Equations 11 and 12, but these species are rapidly oxidised to Co<sub>3</sub>O<sub>4</sub> in the presence of oxygen<sup>44, 45</sup>.



Overall, the second step is assigned to the endothermic decomposition of the oxalate ligand and the exothermic oxidation of Co, CoO and CO<sup>46</sup>. The exothermic events mask the presence of the endothermic oxalate decomposition.

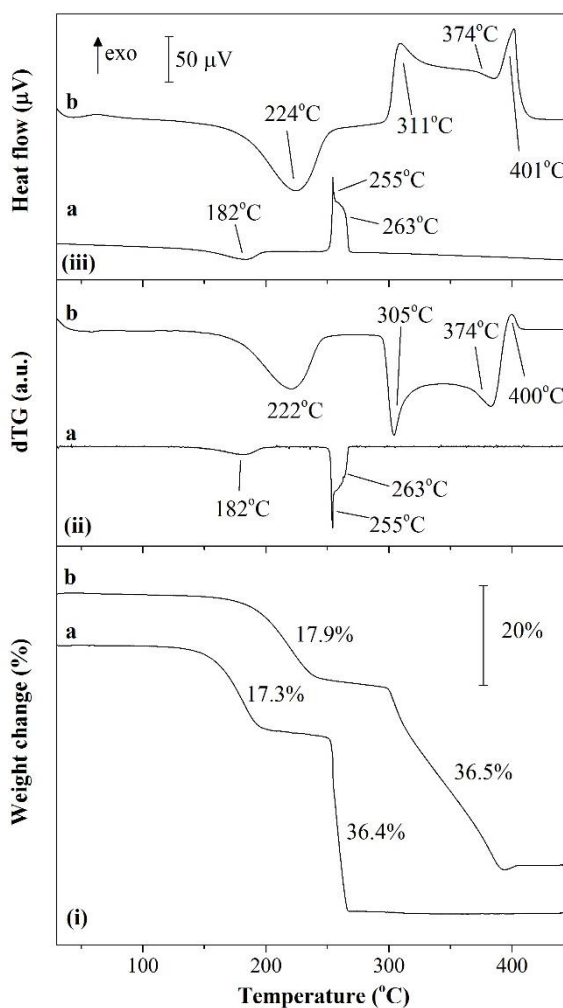


Figure 3.29 – (i) TGA, (ii) dTG and (iii) DTA curves of G30-oxalate: (a) 1°C min<sup>-1</sup> and (b) 10°C min<sup>-1</sup>

When G30-oxalate was decomposed at  $10^{\circ}\text{C min}^{-1}$  (curves (b) in Figure 3.29), a similar TGA profile was observed, but the two main weight loss steps were shifted to higher temperatures (from 182 and  $260^{\circ}\text{C}$  to 224 and  $350^{\circ}\text{C}$ ), as expected for experiments performed at a faster heating rate<sup>47</sup>. The 17.9% weight loss of the first step corresponded to a loss of 1.8 water molecules per formula unit. The separate events that occurred during the second weight loss step were more easily distinguished in the DTG and DTA curves, with the peaks centred at *ca.* 310 and  $374^{\circ}\text{C}$ . An extra feature at  $400^{\circ}\text{C}$  was present for the decomposition performed at  $10^{\circ}\text{C min}^{-1}$ : the weight change was observed to increase after reaching a minimum value. Such a feature has previously been reported when cobalt oxalate was heated rapidly in a limited supply of air<sup>43</sup>, and this mass gain and the corresponding exothermic peak can again be attributed to the oxidation of CoO or metallic Co to  $\text{Co}_3\text{O}_4$ <sup>48</sup>.

Based on the above TGA-DTA data, the G30-oxalate precursor was calcined for 2 hours under open air at 300 or  $400^{\circ}\text{C}$  at a heating rate of  $1^{\circ}\text{C min}^{-1}$ , and at  $400^{\circ}\text{C}$  at a heating rate of  $10^{\circ}\text{C min}^{-1}$ . Complete transformation of the precursor to the desired  $\text{Co}_3\text{O}_4$  catalysts was expected under these conditions. The XRD patterns of the calcined materials are shown in Figure 3.30. The pattern of G30-300-1-o is shown for comparison. Only diffraction peaks corresponding to  $\text{Co}_3\text{O}_4$  were observed for each catalyst, hence complete conversion to the oxide was assumed. The broadest peaks were observed in the pattern of the hydroxycarbonate-derived catalyst (G30-300-1-o, Figure 3.30 (a)), indicating that the oxalate-derived catalysts were more crystalline. The strong exotherm seen for the oxalate ( $>50 \mu\text{V}$ , Figure 3.29 (iii)), compared to the weakly exothermic decomposition of the hydroxycarbonate ( $<5 \mu\text{V}$ , Figure 3.3 (iii)), may have raised the temperature of the sample above the set-point of the furnace. The

peaks of the oxalate-derived catalysts were narrower and more intense for the catalysts calcined at 400°C than the catalyst calcined at 300°C, which suggests that more crystallite growth occurred at higher calcination temperatures. Calculation of average crystallite sizes using the Scherrer equation (values given in Table 3.11) found that G30-oxalate-300-1 consisted of crystallites of 15 nm in size, whilst calcination at 400°C gave rise to crystallites which were twice as large at *ca.* 30 nm in size. No significant difference in crystallite size was observed between the catalysts calcined at 400°C with different heating rates.

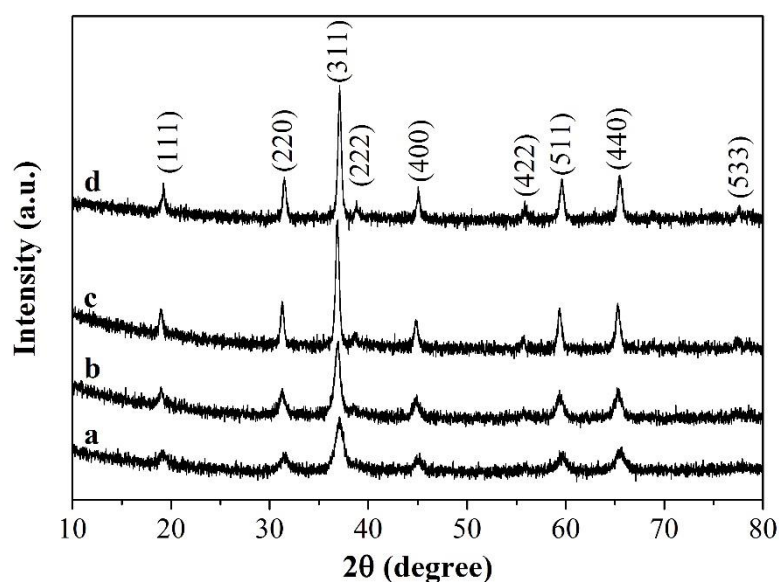


Figure 3.30 – XRD patterns of (a) G30-300-1-o, (b) G30-oxalate-300-1, (c) G30-oxalate-400-1 and (d) G30-oxalate-400-10

The BET specific surface areas of the precursors and catalysts are reported in Table 3.11. At  $17 \text{ m}^2 \text{ g}^{-1}$ , G30-oxalate presented a considerably lower surface area than G30 ( $123 \text{ m}^2 \text{ g}^{-1}$ ). However, a large increase in surface area was observed when G30-oxalate was calcined at 300°C, with the catalyst presenting a surface area of  $98 \text{ m}^2 \text{ g}^{-1}$ . Calcination at 400°C gave a lower surface area of *ca.*  $38 \text{ m}^2 \text{ g}^{-1}$  for the catalysts calcined at both 1 and  $10^\circ \text{C min}^{-1}$ , correlating with the increase in crystallite size observed in XRD experiments. A previous study found that the surface area of

cobalt oxalate dihydrate increased during thermal decomposition in air, reaching a maximum just as decomposition to the oxide was complete<sup>49</sup>. The rise in surface area was attributed to the formation of an increased number of oxide particles of a smaller size from the initial oxalate particles<sup>49</sup>. After the peak in surface area, sintering causes a progressive decrease of the surface area of the oxide<sup>49</sup>.

Table 3.11 – Physicochemical characteristics of precursors and catalysts

Sample	Co <sub>3</sub> O <sub>4</sub> crystallite size (nm)	Surface area (m <sup>2</sup> g <sup>-1</sup> )	Co-O IR bands (cm <sup>-1</sup> )	
			Co <sup>2+</sup>	Co <sup>2+</sup>
G30	-	123	-	-
G30-300-1-o	10	128	658	558
G30-oxalate	-	17	-	-
G30-oxalate-300-1	15	98	658	558
G30-oxalate-400-1	29	38	658	556
G30-oxalate-400-10	32	39	658	556

The FT-IR spectra of the catalysts were recorded and the positions at which the Co-O stretching vibrations were observed are given in Table 3.8. The band attributed to Co<sup>2+</sup>-O was observed at 658 cm<sup>-1</sup> for all catalysts. The band due to Co<sup>3+</sup>-O appeared at 558 cm<sup>-1</sup> for G30-oxalate-300-1, the same position observed for G30-300-1-o. For the catalysts calcined at 400°C, the band was shifted to 556 cm<sup>-1</sup>.

Figure 3.31 shows a secondary electron SEM micrograph of G30-oxalate-300-1. This catalyst (along with the G30-oxalate precursor and the catalysts calcined at 400°C) presented a similar morphology and wide range of particle sizes to the other catalysts in this chapter prepared by mechanochemical reactions.

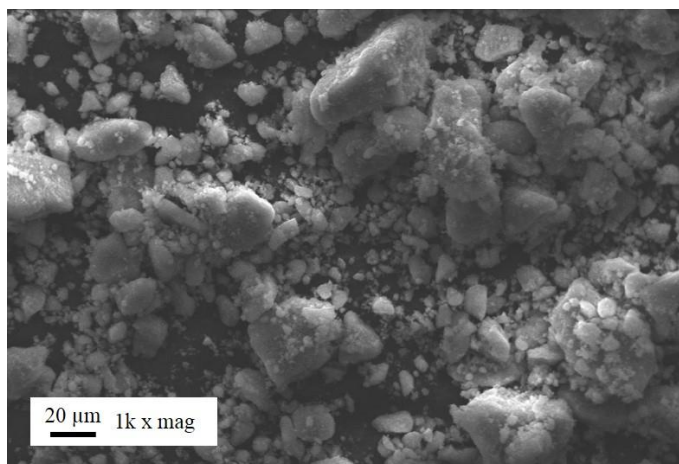


Figure 3.31 – SEM micrograph of G30-oxalate-300-1-o at 1k x mag

The TPR profiles of the catalysts are shown in Figure 3.32, with the profile of G30-300-1-o shown for comparison. The first peak (peak I), which corresponds to the reduction of  $\text{Co}_3\text{O}_4$  to  $\text{CoO}$ , occurred at a temperature  $10^\circ\text{C}$  lower for the hydroxycarbonate-derived catalyst compared to the oxalate-derived catalysts. The area of peak I to the combined areas of the higher temperature peaks (peaks II and III for the catalysts calcined at  $300^\circ\text{C}$ , and peaks II, III and IV for the catalysts calcined at  $400^\circ\text{C}$ ) was approximately 1:3. This indicated that the high temperature peaks were all due to the reduction of  $\text{CoO}$  to  $\text{Co}$  metal, and the presence of multiple peaks is again attributed to the reduction of  $\text{CoO}$  particles of a range of sizes. In contrast to the hydroxycarbonate-derived catalysts discussed in *Section 3.2.1.2*, the reduction peaks were present at similar temperatures for each of the oxalate-derived catalysts, in spite of differences in crystallite sizes.

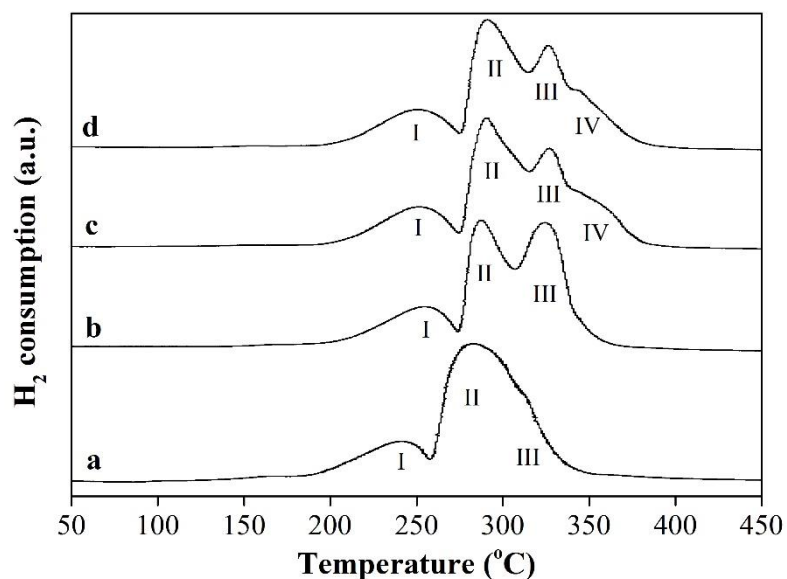


Figure 3.32 – H<sub>2</sub>-TPR profiles of (a) G30-300-1-o, (b) G30-oxalate-300-1, (c) G30-oxalate-400-1 and (d) G30-oxalate-400-10

The XPS spectra of the catalysts were recorded and similar profiles were observed for all catalysts. In the Co 2p region, two main peaks at 779.7 and 794.7 eV, and satellites centred at 790 and 805 eV, were indicative of Co<sub>3</sub>O<sub>4</sub><sup>21</sup>. In the O 1s region, peaks observed at 529.8 and 531.5 eV were attributed to lattice O<sup>2-</sup> and surface O<sup>-</sup> species, respectively<sup>22</sup>.

The activity of the catalysts for the total oxidation of propane is shown in Figure 3.33. All catalysts achieved 100% propane conversion by 325°C. Comparison of the temperatures at which 10, 50 and 90% propane conversions were achieved (reported in Table 3.12) revealed that the catalyst calcined at 300°C was the most active of the oxalate-derived catalysts (*e.g.* T<sub>50</sub> was *ca.* 20°C lower for this catalyst). G30-oxalate-300-1 was slightly less active than G30-300-1-o, the most active hydroxycarbonate-derived catalyst described in this chapter. The catalysts calcined at 400°C displayed similar activities to each other at lower temperatures, but the sample

calcined with a heating rate of  $1^{\circ}\text{C min}^{-1}$  required a temperature  $15^{\circ}\text{C}$  higher than the sample calcined at  $10^{\circ}\text{C min}^{-1}$  to achieve 90% conversion.

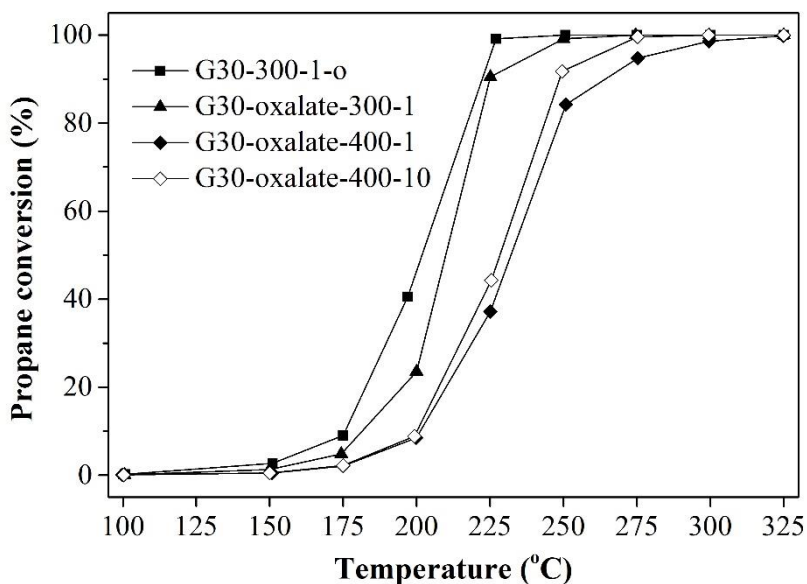


Figure 3.33 – Propane conversion over  $\text{Co}_3\text{O}_4$  catalysts

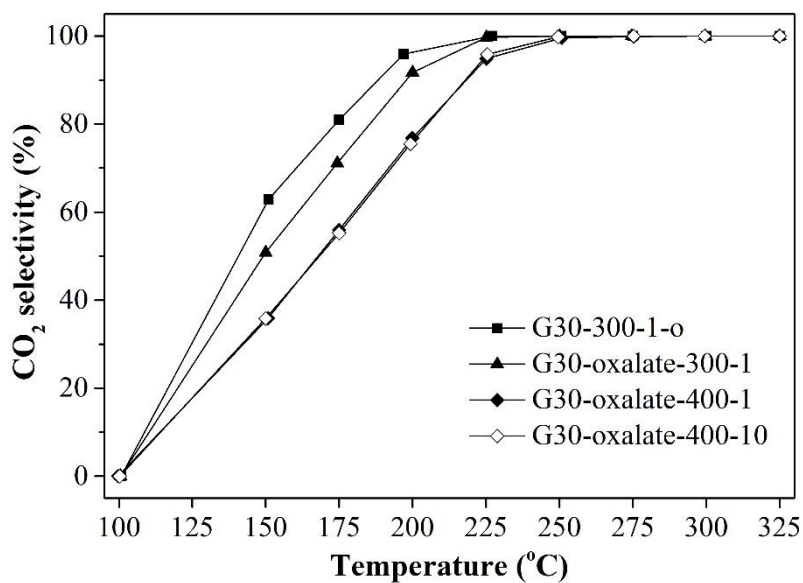


Figure 3.34 –  $\text{CO}_2$  selectivity over  $\text{Co}_3\text{O}_4$  catalysts

The selectivity of the catalysts towards  $\text{CO}_2$  is shown in Figure 3.34. Propene was produced over the catalysts at low propane conversions, and selectivity to  $\text{CO}_2$  increased with conversion. No other reaction products were observed.

Table 3.12 – Catalytic activity

Sample	T <sub>10</sub> (°C)	T <sub>50</sub> (°C)	T <sub>90</sub> (°C)	Reaction rate <sup>a</sup> (mol <sub>C<sub>3</sub>H<sub>8</sub></sub> g <sub>cat</sub> <sup>-1</sup> s <sup>-1</sup> )	Specific reaction rate <sup>a</sup> (mol <sub>C<sub>3</sub>H<sub>8</sub></sub> m <sup>-2</sup> s <sup>-1</sup> )
G30-300-1-o	176	202	222	25.7 x 10 <sup>-7</sup>	2.0 x 10 <sup>-8</sup>
G30-oxalate-300-1	181	210	225	28.7 x 10 <sup>-7</sup>	2.9 x 10 <sup>-8</sup>
G30-oxalate-400-1	201	232	264	9.8 x 10 <sup>-7</sup>	2.6 x 10 <sup>-8</sup>
G30-oxalate-400-10	200	228	249	11.7 x 10 <sup>-7</sup>	3.0 x 10 <sup>-8</sup>

a – Reaction rates were calculated from propane conversion at 225°C

The rates of reaction of the catalysts at 225°C are given in Table 3.12. For the oxalate-derived catalysts, the highest activity per gram of catalyst was observed for G30-oxalate-300-1. This catalyst presented a rate which was comparable to that of G30-300-1-o. The catalysts calcined at higher temperatures displayed lower reaction rates. Similar specific reaction rates were observed for all samples.

Catalysts derived from mechanochemically synthesised cobalt oxalate have previously been reported. Cobalt hydroxycarbonate hydrate and oxalic acid starting materials were utilised in the synthesis of Co<sub>3</sub>O<sub>4</sub> catalysts for carbon monoxide oxidation<sup>50, 51</sup>. Cobalt acetate and oxalic acid were reacted to give Co<sub>3</sub>O<sub>4</sub> pH sensors<sup>52</sup>. The work in this chapter is the first report of propane total oxidation over Co<sub>3</sub>O<sub>4</sub> catalysts derived from mechanochemically synthesised cobalt oxalate.

The activity of the G30-oxalate catalysts described in this section was found to be closely linked to surface area and crystallite size. As observed for the G30 catalysts in *Section 3.2.1*, activity decreased with increasing calcination temperature due to the reduction in surface area and increase in crystallite size of the catalysts. The temperature at which the catalysts were calcined was found to be far more important than the heating rate employed, as demonstrated by the negligible differences in physicochemical properties and activity observed for G30-oxalate-400-1 and

G30-oxalate-400-10. As previously discussed for the hydroxycarbonate-derived catalysts, the reduction temperatures observed in H<sub>2</sub>-TPR of the G30-oxalate catalysts did not give a good indication of propane oxidation activity.

With a lower surface area and larger crystallite size, G30-oxalate-300-1 displayed a slightly lower activity than G30-300-1-o. Nonetheless, the catalysts were similar despite synthesis *via* different chemical routes. As decomposition of the precursor gives only carbon dioxide and water as by-products, synthesis of Co<sub>3</sub>O<sub>4</sub> from cobalt oxalate dihydrate avoided the presence of surface contaminants. Additionally, calcination at 300°C gave rise to a Co<sup>3+</sup>-O bond of equal strength to that of the bond in G30-300-1-o.

As discussed in *Section 3.2.1*, the weaker Co<sup>3+</sup>-O bond of the catalysts calcined at higher temperatures, which could increase activity by facilitation of the Mars-van Krevelen cycle, is likely outweighed by the lower surface area and larger crystallite size of these samples.

### **3.4.3 Conclusions**

Cobalt oxalate dihydrate was produced by the mechanochemical reaction of cobalt acetate and oxalic acid. Calcination of the precursor gave rise to Co<sub>3</sub>O<sub>4</sub> catalysts with high activity for propane total oxidation activity, comparable to that of hydroxycarbonate hydrate-derived catalysts. High surface area and small crystallite size were necessary for high activity. Overall, mechanochemically synthesised cobalt oxalate dihydrate appeared to be a viable precursor for highly active Co<sub>3</sub>O<sub>4</sub> catalysts.

### 3.5 Chapter conclusions

The preparation of  $\text{Co}_3\text{O}_4$  by mechanochemical synthesis of a precursor and subsequent calcination has been investigated. Cobalt hydroxycarbonate hydrate precursors can be synthesised from a range of carbonates or hydrogen carbonates, but the most active catalyst for propane total oxidation was produced from cobalt nitrate and ammonium hydrogen carbonate ground together for 30 minutes. Additionally, calcination of the precursors at  $300^\circ\text{C}$  under non-flowing air was found to be the optimal method of thermal decomposition. A cobalt oxalate dihydrate precursor was also prepared and the resulting catalysts demonstrated comparable activity to the hydroxycarbonate-derived catalysts.

Small crystallites and high surface areas were found to be necessary features for highly active catalysts. Provided that these criteria were fulfilled, the weaker the  $\text{Co}^{3+}\text{-O}$  bond of the catalyst, the greater the observed propane total oxidation activity. The absence of surface contaminants (such as sodium) was also found to be necessary for high activity. Whilst the most active catalysts generally displayed high reducibility in TPR experiments, no firm link between reduction temperature and catalytic activity was observed.

### 3.6 References

1. H. Yang, Y. Hu, X. Zhang and G. Qiu, *Materials Letters*, 2004, **58**, 387-389.
2. B. X. Li, Y. Xie, C. Z. Wu, Z. Q. Li and J. Zhang, *Mater. Chem. Phys.*, 2006, **99**, 479-486.
3. R. Xu and H. C. Zeng, *J. Phys. Chem. B*, 2003, **107**, 12643-12649.
4. J. Q. Wang, B. Niu, G. D. Du, R. Zeng, Z. X. Chen, Z. P. Guo and S. X. Dou, *Mater. Chem. Phys.*, 2011, **126**, 747-754.
5. J. Yang, H. F. Cheng and R. L. Frost, *Spectroc. Acta Pt. A-Molec. Biomolec. Spectr.*, 2011, **78**, 420-428.
6. P. Atkins and J. De Paula, *Atkins' Physical Chemistry*, OUP, Oxford, 2006.

7. P. Porta, R. Dragone, G. Fierro, M. Inversi, M. Lojacono and G. Moretti, *J. Chem. Soc.-Faraday Trans.*, 1992, **88**, 311-319.
8. T. Ishikawa and E. Matijevic, *Colloid Polym. Sci.*, 1991, **269**, 179-186.
9. D. G. Klissurski and E. L. Uzunova, *Chem. Mat.*, 1991, **3**, 1060-1063.
10. M. Behrens, F. Girgsdies, A. Trunschke and R. Schlögl, *Eur. J. Inorg. Chem.*, 2009, 1347-1357.
11. G. Salek, P. Alphonse, P. Dufour, S. Guillemet-Fritsch and C. Tenailleau, *Appl. Catal. B-Environ.*, 2014, **147**, 1-7.
12. P. Dutta, M. S. Seehra, S. Thota and J. Kumar, *J. Phys.-Condes. Matter*, 2008, **20**, 8.
13. Q. Liu, L. C. Wang, M. Chen, Y. Cao, H. Y. He and K. N. Fan, *Journal of Catalysis*, 2009, **263**, 104-113.
14. B. Solsona, T. E. Davies, T. Garcia, I. Vazquez, A. Dejoz and S. H. Taylor, *Appl. Catal. B-Environ.*, 2008, **84**, 176-184.
15. B. de Rivas, R. Lopez-Fonseca, C. Jimenez-Gonzalez and J. I. Gutierrez-Ortiz, *Journal of Catalysis*, 2011, **281**, 88-97.
16. I. Manouchehri, P. Kameli and H. Salamati, *J. Supercond. Nov. Magn*, 2011, **24**, 1907-1910.
17. B. Lefez, P. Nkeng, J. Lopitiaux and G. Poillerat, *Mater. Res. Bull.*, 1996, **31**, 1263-1267.
18. P. Nkeng, J. F. Koenig, J. L. Gautier, P. Chartier and G. Poillerat, *J. Electroanal. Chem.*, 1996, **402**, 81-89.
19. *Sintering: Mechanisms of Conventional Nanodensification and Field Assisted Processes*, Springer Verlag, Berlin, 2013.
20. D. Potoczna-Petru and L. Kepinski, *Catalysis Letters*, 2001, **73**, 41-46.
21. M. C. Biesinger, B. P. Payne, A. P. Grosvenor, L. W. M. Lau, A. R. Gerson and R. S. Smart, *Appl. Surf. Sci.*, 2011, **257**, 2717-2730.
22. B. de Rivas, R. Lopez-Fonseca, C. Jimenez-Gonzalez and J. I. Gutierrez-Ortiz, *Chem. Eng. J.*, 2012, **184**, 184-192.
23. B. Solsona, I. Vazquez, T. Garcia, T. E. Davies and S. H. Taylor, *Catalysis Letters*, 2007, **116**, 116-121.
24. B. Puertolas, A. Smith, I. Vazquez, A. Dejoz, A. Moragues, T. Garcia and B. Solsona, *Chem. Eng. J.*, 2013, **229**, 547-558.
25. E. Finocchio, R. J. Willey, G. Busca and V. Lorenzelli, *J. Chem. Soc.-Faraday Trans.*, 1997, **93**, 175-180.
26. B. Solsona, T. Garcia, G. J. Hutchings, S. H. Taylor and M. Makkee, *Appl. Catal. A-Gen.*, 2009, **365**, 222-230.
27. T. Garcia, S. Agouram, J. F. Sanchez-Royo, R. Murillo, A. M. Mastral, A. Aranda, I. Vazquez, A. Dejoz and B. Solsona, *Appl. Catal. A-Gen.*, 2010, **386**, 16-27.
28. R. P. Marin, S. A. Kondrat, R. K. Pinnell, T. E. Davies, S. Golunski, J. K. Bartley, G. J. Hutchings and S. H. Taylor, *Appl. Catal. B-Environ.*, 2013, **140**, 671-679.
29. V. V. Galvita, H. Poelman, G. Rampelberg, B. De Schutter, C. Detavernier and G. B. Marin, *Catalysis Letters*, 2012, **142**, 959-968.
30. A. C. Gluhoi, N. Bogdanchikova and B. E. Nieuwenhuys, *Catal. Today*, 2006, **113**, 178-181.
31. R. P. Marin, Cardiff University, Cardiff, 2012.
32. S. M. I. Morsy, S. A. Shaban, A. M. Ibrahim and M. M. Selim, *J. Alloy. Compd.*, 2009, **486**, 83-87.

33. A. A. Mirzaei, H. R. Shaterian and M. Kaykhaii, *Appl. Surf. Sci.*, 2005, **239**, 246-254.
34. G. Prieto, K. P. de Jong and P. E. de Jongh, *Catal. Today*, 2013, **215**, 142-151.
35. X. An, B. S. Wu, W. J. Hou, H. J. Wan, Z. C. Tao, T. Z. Li, Z. X. Zhang, H. W. Xiang, Y. W. Li, B. F. Xu and F. Yi, *J. Mol. Catal. A-Chem.*, 2007, **263**, 266-272.
36. L. C. Huang, Z. F. Qin, G. F. Wang, M. X. Du, H. Ge, X. K. Li, Z. W. Wu and J. G. Wang, *Ind. Eng. Chem. Res.*, 2010, **49**, 4670-4675.
37. J. W. Niemantsverdriet, *Spectroscopy in Catalysis An Introduction*, Wiley-VCH, Weinheim, 2007.
38. J. Ahmed, T. Ahmad, K. V. Ramanujachary, S. E. Lofland and A. K. Ganguli, *Journal of Colloid and Interface Science*, 2008, **321**, 434-441.
39. W. A. Ang, Y. L. Cheah, C. L. Wong, R. Prasanth, H. H. Hng and S. Madhavi, *J. Phys. Chem. C*, 2013, **117**, 16316-16325.
40. M. A. Gabal, A. A. El-Bellihi and S. S. Ata-Allah, *Mater. Chem. Phys.*, 2003, **81**, 84-92.
41. P. Román, C. Guzmán-Miralles, A. Luque, J. I. Beitia, J. Cano, F. Lloret, M. Julve and S. Alvarez, *Inorg. Chem.*, 1996, **35**, 3741-3751.
42. H. Luo, D. B. Zou, L. G. Zhou and T. K. Ying, *J. Alloy. Compd.*, 2009, **481**, L12-L14.
43. D. Dollimore, D. L. Griffiths and D. Nicholson, *Journal of the Chemical Society (Resumed)*, 1963, 2617-2623.
44. M. Maciejewski, E. Ingier-Stocka, W. D. Emmerich and A. Baiker, *J. Therm. Anal.*, 2000, **60**, 735-758.
45. A. K. Nikumbh, A. E. Athare and V. B. Raut, *Thermochim. Acta*, 1991, **186**, 217-233.
46. M. C. Lopez, J. L. Tirado and C. P. Vicente, *J. Power Sources*, 2013, **227**, 65-71.
47. D. Skoog, F. Holler and S. Crouch, *Principles of Instrumental Analysis*, Thomson Brooks/Cole, Australia, 2006.
48. J. Mullens, A. Vos, R. Carleer, J. Yperman and L. C. Vanpoucke, *Thermochim. Acta*, 1992, **207**, 337-339.
49. D. Dollimore and D. Nicholson, *Journal of the Chemical Society*, 1962, 960-&.
50. Q. Liu, C. X. Liu, X. L. Nie, L. Bai and S. H. Wen, *Materials Letters*, 2012, **72**, 101-103.
51. C. X. Liu, Q. Liu, L. Bai, A. Q. Dong, G. B. Liu and S. H. Wen, *J. Mol. Catal. A-Chem.*, 2013, **370**, 1-6.
52. Q. W. Li, G. A. Luo and Y. Q. Shu, *Anal. Chim. Acta*, 2000, **409**, 137-142.

# Chapter 4

## Preparation of $\text{Co}_3\text{O}_4$ via precipitation

### 4.1 Introduction

In this chapter the preparation of  $\text{Co}_3\text{O}_4$  by precipitation and subsequent thermal decomposition of a precursor is studied. A number of precipitation parameters are investigated with a view to improving catalytic activity. The samples are characterised by a range of techniques and the catalysts are tested for the total oxidation of propane.

### 4.2 Investigation of starting materials and order of addition in the precipitation of $\text{Co}_3\text{O}_4$ precursors

Initial experiments focused on the precipitation of precursors from different cobalt salts (nitrate or acetate) and precipitating agents (sodium carbonate or oxalic acid). The order in which the cobalt salt and the precipitating agent were added together was also investigated: either the precipitating agent solution was added to the cobalt salt solution (referred to as PA to Co) or the cobalt salt solution was added to the precipitating agent solution (referred to as Co to PA).

#### 4.2.1 Preparation

Aqueous solutions of sodium carbonate or oxalic acid (0.25 M) were added to aqueous solutions of cobalt nitrate or cobalt acetate (0.25 M) (or *vice versa*) on a 1:1 molar

ratio according to the method described in *Section 2.1.1.2*. The precipitates were aged for 2 h. The precursors were calcined for 2 h at 300°C with a heating rate of 10°C min<sup>-1</sup> in open air (no gas flow through an open tubular furnace). This information and the nomenclature of the prepared samples are summarised in Table 4.1. *N.B.* In contrast to Chapter 3, the uncalcined catalyst precursors and the catalysts have not been named separately in this chapter.

Table 4.1 – Sample nomenclature and pH values

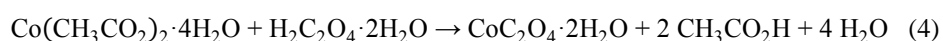
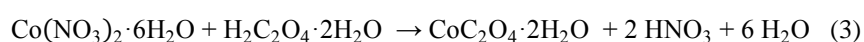
Sample	Order of addition	Cobalt salt solution			Precipitating agent solution			Molar ratio	Aging time (h)	Reaction solution pH	
		salt	conc (M)	initial pH	agent	conc (M)	initial pH			before aging	after aging
CtoN	PA to Co	nitrate	0.25	5.9	Na <sub>2</sub> CO <sub>3</sub>	0.25	12.1	1:1	2	7.3	7.4
CtoA	PA to Co	acetate	0.25	7.3	Na <sub>2</sub> CO <sub>3</sub>	0.25	11.7	1:1	2	7.5	7.9
OtoN	PA to Co	nitrate	0.25	5.3	oxalic acid	0.25	0.8	1:1	2	0.6	0.5
OtoA	PA to Co	acetate	0.25	7.3	oxalic acid	0.25	0.9	1:1	2	3.3	3.2
NtoC	Co to PA	nitrate	0.25	5.2	Na <sub>2</sub> CO <sub>3</sub>	0.25	11.7	1:1	2	7.0	7.4
AtoC	Co to PA	acetate	0.25	7.3	Na <sub>2</sub> CO <sub>3</sub>	0.25	11.6	1:1	2	7.2	7.7
NtoO	Co to PA	nitrate	0.25	5.3	oxalic acid	0.25	0.6	1:1	2	0.4	0.3
AtoO	Co to PA	acetate	0.25	7.2	oxalic acid	0.25	0.8	1:1	2	2.7	3.1

The pH values of the cobalt salt and precipitating agent solutions were measured prior to the start of the reaction. Additionally, the pH of the reaction solution was recorded upon total addition of the precipitating agent (just before aging commenced) and again at the end of the 2 h aging time. These values are reported in Table 4.1. No significant differences in pH were observed between the reaction solutions prepared by PA to Co precipitation or Co to PA precipitation.

When sodium carbonate was used as precipitating agent the solutions presented a value of *ca.* pH 7.3 before aging, and a slight increase to *ca.* pH 7.6 was observed at the end of the 2 h aging. Such an increase in pH has previously been assigned to the evolution of gaseous carbon dioxide<sup>1</sup>, which would shift the equilibrium  $\text{CO}_2 + \text{H}_2\text{O} \leftrightarrow \text{H}_2\text{CO}_3 \leftrightarrow \text{HCO}_3^- + \text{H}^+ \leftrightarrow \text{CO}_3^{2-} + 2\text{H}^+$  to the left, reducing the concentration of hydrogen ions. The reactions between sodium carbonate and cobalt nitrate or cobalt acetate were assumed to proceed according to Equations 1 and 2, respectively:



When oxalic acid was used as the precipitating agent, the reaction solutions were observed to be very acidic ( $0.4 \leq \text{pH} \leq 3.3$ ). A small decrease in pH after aging was observed in all experiments except AtoO, where the pH rose slightly. The lower pH observed for the experiments involving cobalt nitrate may be attributed to the production of a strong acid (nitric acid) in these reactions, whilst a weak acid (acetic acid) is produced on reaction of cobalt acetate, as shown in Equations 3 and 4, respectively:



### 4.2.2 Results and Discussion

The XRD patterns of the precursors synthesised by reaction of the cobalt salts with sodium carbonate are shown in Figure 4.1. All materials corresponded to hydrated cobalt hydroxycarbonate<sup>2</sup>,  $(\text{Co}(\text{OH})_x(\text{CO}_3)_{0.5(2-x)} \cdot n\text{H}_2\text{O})$ , which was the phase obtained from mechanochemical reactions of cobalt nitrate with various carbonates and hydrogen carbonates in Chapter 3. As observed for the mechanochemical materials, the precipitated materials presented very broad diffraction peaks with low intensities, which indicated that poorly crystalline materials were synthesised.

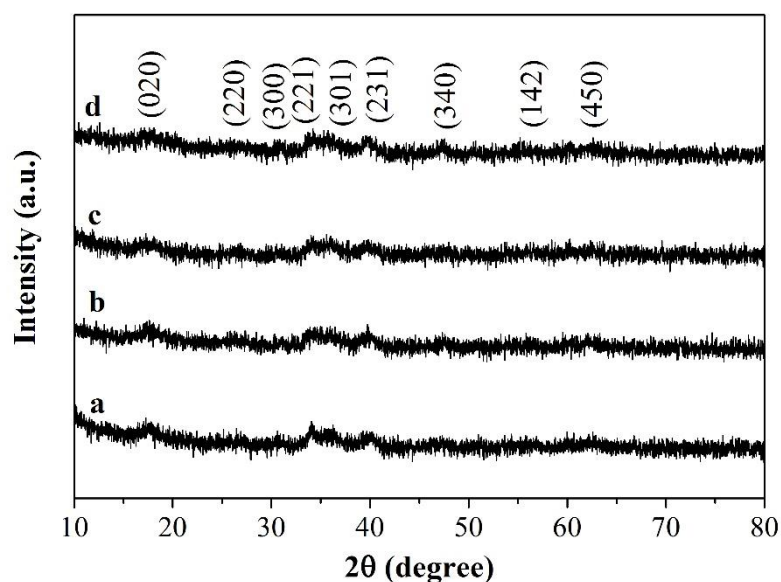


Figure 4.1 – XRD patterns of PA to Co precursors: (a) CtoN, (b) CtoA; and Co to PA precursors: (c) NtoC, (d) AtoC

The XRD patterns of the precursors synthesised by reaction of the cobalt salts with oxalic acid are shown in Figure 4.2. For all materials, all diffraction peaks corresponded to cobalt oxalate dihydrate,  $(\text{CoC}_2\text{O}_4 \cdot 2\text{H}_2\text{O})^{3,4}$ . This phase was also obtained from the mechanochemical reaction of cobalt acetate with oxalic acid, as described in *Section 3.4* of Chapter 3. The high intensities and narrowness of the main diffraction peaks indicated that the oxalates had long range crystallinity.

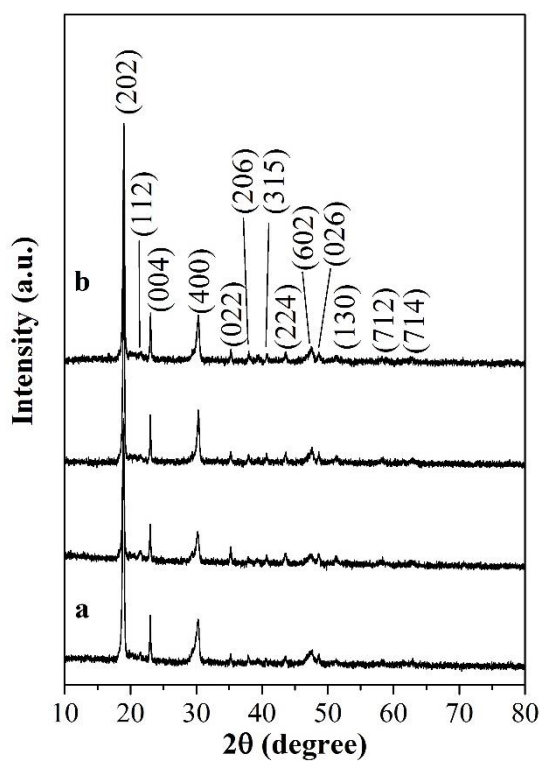


Figure 4.2 – XRD patterns of PA to Co precursors: (a) OtoN, (b) OtoA; and Co to PA precursors: (c) NtoO, (d) AtoO

Figure 4.3 shows the FT-IR spectra of the sodium carbonate-derived precursors. As expected, the spectra indicated that the precursors were hydrated cobalt hydroxycarbonate. As discussed in Chapter 3, stretching vibrations of carbonate anions were present at 1458, 1381 and 1074  $\text{cm}^{-1}$  whilst bands observed at 829, 740 and 690  $\text{cm}^{-1}$  were due to bending vibrations of carbonate anions<sup>5</sup>. Bands at 3481  $\text{cm}^{-1}$  and 1040  $\text{cm}^{-1}$  indicated the presence of water and/or hydroxyl anions<sup>5</sup>. The band at 962  $\text{cm}^{-1}$  was assigned to Co-OH bending<sup>5</sup>.

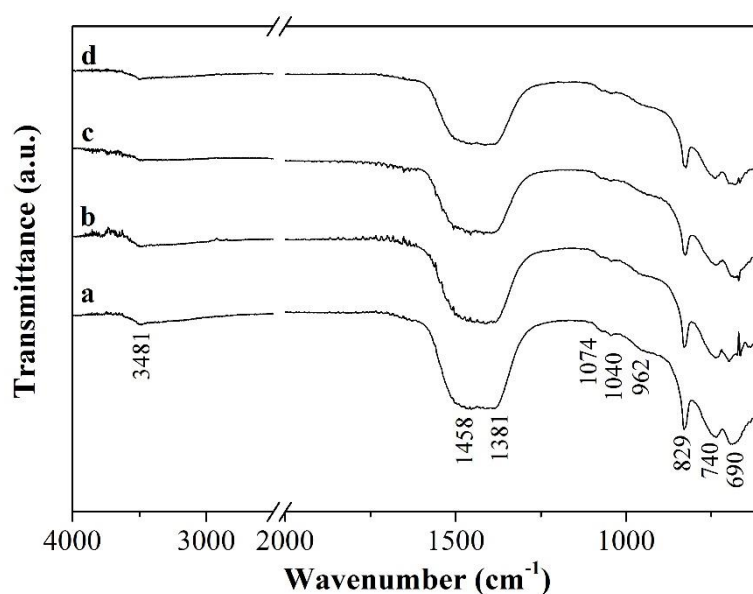


Figure 4.3 – FT-IR spectra of PA to Co precursors: (a) CtoN, (b) CtoA; and Co to PA precursors: (c) NtoC, (d) AtoC

Figure 4.4 shows the FT-IR spectra of the oxalic acid-derived precursors. The spectra indicated that all of the precursors were hydrated cobalt oxalate. As discussed in Chapter 3, the band at  $3356\text{ cm}^{-1}$  was assigned to water of crystallisation<sup>6</sup>. Bands due to the oxalate anion were present at  $1610$ ,  $1359$  and  $1316\text{ cm}^{-1}$  (stretching vibrations) and  $825\text{ cm}^{-1}$  (bending vibrations), and the band at  $738\text{ cm}^{-1}$  was attributed to Co-O vibrations<sup>7,8</sup>.

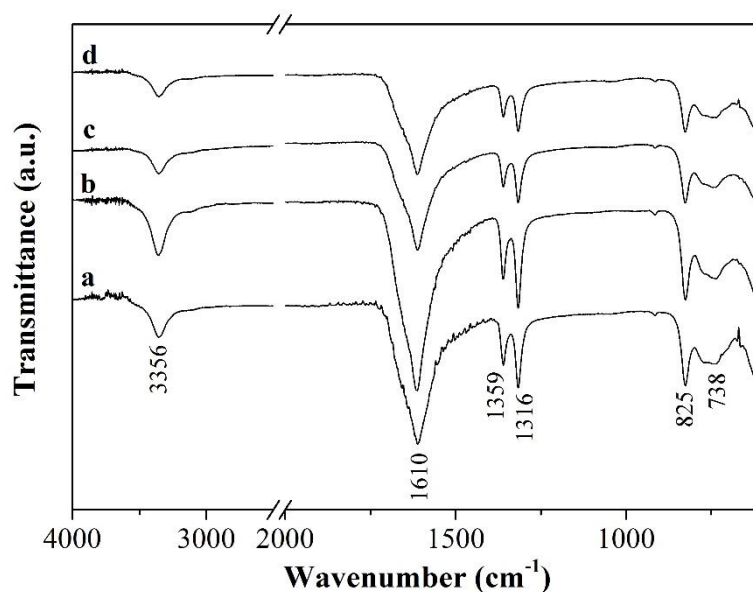


Figure 4.4 – FT-IR spectra of PA to Co precursors: (a) OtoN, (b) OtoA; and Co to PA precursors: (c) NtoO, (d) AtoO

The TGA-DTG-DTA curves of the precursors synthesised from sodium carbonate are shown in Figure 4.5 (a) and (b). A total weight loss of between 24.6 and 25.9% was observed for these precursors, which is in agreement with the theoretical value of 25.6% for the transformation of  $\text{Co}(\text{OH})(\text{CO}_3)_{0.5} \cdot 0.11\text{H}_2\text{O}$  to  $\text{Co}_3\text{O}_4$ , within the experimental error of  $\pm 5\%$ . The formula of each precursor is assumed to be  $(\text{Co}(\text{OH})_x(\text{CO}_3)_{0.5(2-x)} \cdot n\text{H}_2\text{O}) - \text{CHN}$  analysis would enable the exact formulae to be determined. An initial gradual weight loss until  $190^\circ\text{C}$  is assigned to the removal of surface-adsorbed water and water of crystallisation. The second weight loss step, centred at  $245^\circ\text{C}$ , was accompanied by two overlapping peaks in both the DTG and

DTA curves, which indicated that two events contributed to this main weight loss step. The first event may be attributed to the decomposition of hydroxyl and carbonate groups and the simultaneous oxidation of  $\text{Co}^{2+}$  to  $\text{Co}^{3+}$  to form the oxide catalyst<sup>5, 9</sup>, with the exothermic oxidation of the cobalt ions masking the endothermic decomposition of the precursor anions. As the second event is also exothermic, it is attributed to the concurrent endothermic decomposition of “high temperature carbonates”<sup>10</sup> (observed for G30 in *Section 3.2.1*) and exothermic oxidation of any remaining  $\text{Co}^{2+}$  ions, which did not initially react due to the fast heating rate of  $10^\circ\text{C min}^{-1}$ . Mass spectroscopic analysis of the effluent gases could clarify the decomposition pathway. The gradual weight loss observed until *ca.*  $400^\circ\text{C}$  could represent the slow transformation of a non-stoichiometric oxide to  $\text{Co}_3\text{O}_4$ <sup>11</sup>.

The TGA-DTG-DTA curves of the precursors synthesised from oxalic acid, shown in Figure 4.5 (c) and (d), were also analogous to the profiles observed for the mechanochemically synthesised counterpart in Chapter 3. The two main weight loss steps were attributed to the loss of water of crystallisation and the subsequent transformation of the anhydrous oxalate to cobalt oxide<sup>6</sup>. The first step corresponded to a loss of 1.6 molecules of water per formula unit for the PA to Co samples and 1.7 molecules of water for the Co to PA samples. For the second step, the observed weight loss of 37.0-37.5% was in agreement (within experimental error of  $\pm 5\%$ ) with the theoretical value of 36.4% for the decomposition of  $\text{CoC}_2\text{O}_4$  to  $\text{Co}_3\text{O}_4$ . As described in *Section 3.4*, the second weight loss step is complicated by the formation and rapid oxidation of CoO, metallic cobalt and carbon monoxide<sup>12</sup>.

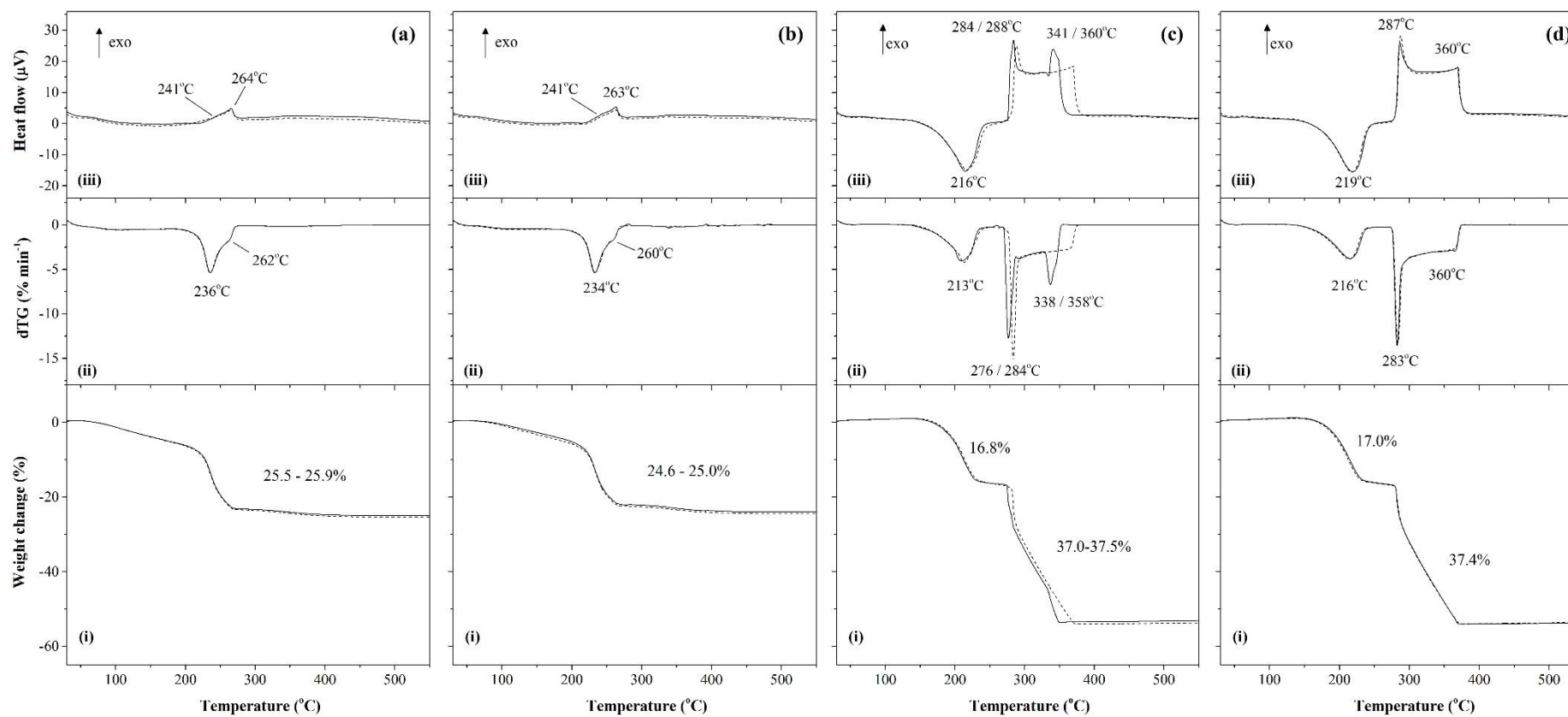


Figure 4.5 – (i) TGA, (ii) DTG and (iii) DTA curves of  
 (a) CtoN precursor (solid line) and CtoA precursor (dashed line), (b) NtoC precursor (solid line) and AtoC precursor (dashed line),  
 (c) OtoN precursor (solid line) and OtoA precursor (dashed line), (d) NtoO precursor (solid line) and AtoO precursor (dashed line)

The TGA data presented in Figure 4.5 indicated that the major decomposition steps had occurred or were underway by 300°C, but further TGA experiments were performed to determine if full decomposition of both the hydroxycarbonate and oxalate precursors would occur after calcination at this temperature. A sample of CtoA was heated to 300°C at a rate of 10°C min<sup>-1</sup> then held at that temperature for 2 hours (shown in Figure 4.6 (i)). The observed weight loss of 25.2% was in agreement with the expected value for complete decomposition (*ca.* 25.6%). A sample of OtoA was also heated under these conditions (Figure 4.6 (ii)) and a weight loss of 54.4% was observed, which was also consistent with the expected value for conversion to Co<sub>3</sub>O<sub>4</sub> (56.1%). In both cases, full decomposition was completed within the 2 hour isotherm. These results suggested that heat treatment of the precursors under these conditions should yield the desired Co<sub>3</sub>O<sub>4</sub> phase, hence the precursors were calcined at 300°C for 2 hours with a heating rate of 10°C min<sup>-1</sup>.

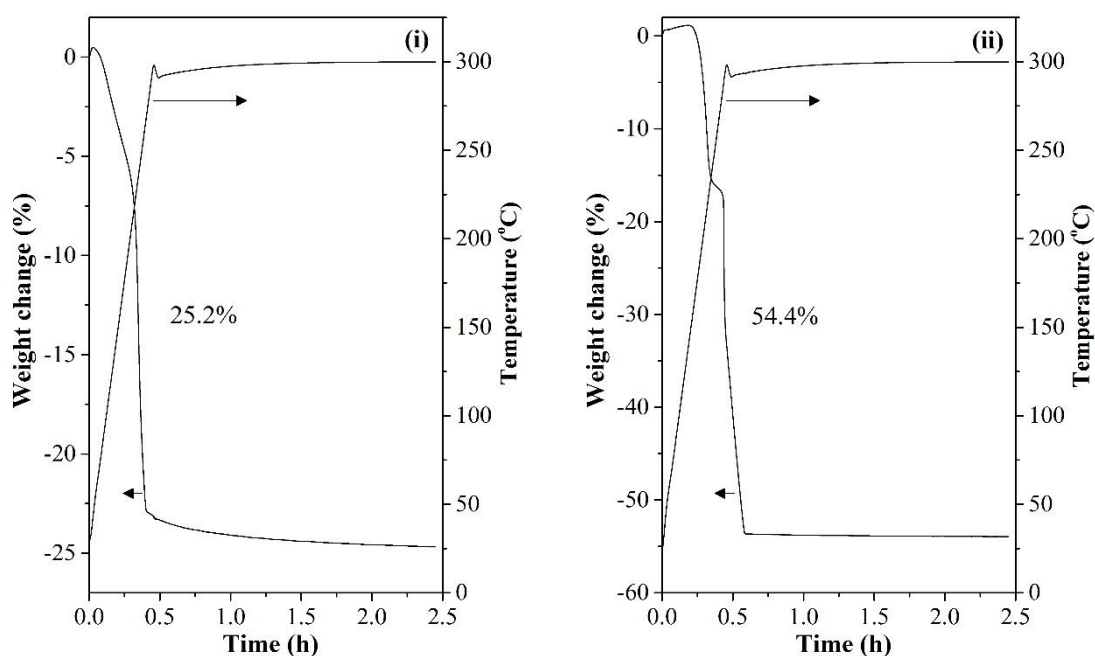


Figure 4.6 – TGA of precursors under calcination conditions (300°C for 2 h at 10°C min<sup>-1</sup>):  
(i) CtoA precursor and (ii) OtoA precursor

The XRD patterns of the catalysts formed by calcination are shown in Figure 4. As expected, only peaks corresponding to  $\text{Co}_3\text{O}_4$  were observed<sup>13</sup>. The catalysts from the oxalate precursors presented narrower and more intense diffraction peaks than the catalysts from the hydroxycarbonate precursors, which is attributed to the more exothermic decomposition of the oxalate precursor (observed in the DTA curves of these samples, Figure 4.5 (iii)). The average  $\text{Co}_3\text{O}_4$  crystallite sizes are reported in Table 4.2. The crystallites of the oxalate-derived catalysts were found to be larger than those of the hydroxycarbonate-derived catalysts by 7-10 nm (18-19 nm vs 9-11 nm).

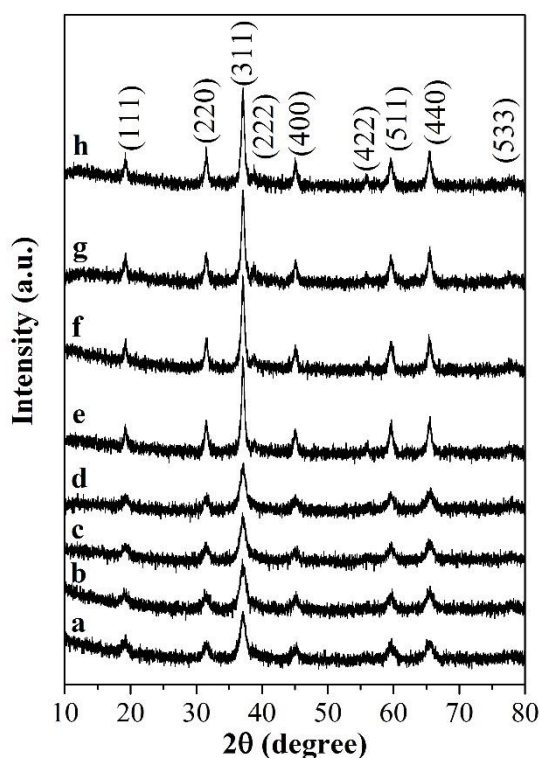


Figure 4.7 – XRD patterns of (a) CtoN, (b) CtoA, (c) NtoC, (d) AtoC, (e) OtoN, (f) OtoA, (g) NtoO and (h) AtoO

The BET surface areas of the precursors and catalysts are given in Table 4.2. The precursors synthesised from sodium carbonate presented high surface areas between 147 and 166  $\text{m}^2 \text{g}^{-1}$ . In contrast, the precursors synthesised from oxalic acid presented very low surface areas of 5  $\text{m}^2 \text{g}^{-1}$  or less. Upon calcination, the surface areas of the

hydroxycarbonate-derived samples decreased to *ca.* 130 m<sup>2</sup> g<sup>-1</sup>. A large increase in surface area was observed for the oxalate-derived samples following calcination, which may be attributed to the formation of many small Co<sub>3</sub>O<sub>4</sub> particles from each oxalate particle<sup>14</sup>. However, at *ca.* 70 m<sup>2</sup> g<sup>-1</sup> the surface areas of these catalysts were approximately 50% lower than those of the hydroxycarbonate-derived catalysts.

Table 4.2 – Physicochemical characteristics of samples and catalytic activity

Sample	Surface area (m <sup>2</sup> g <sup>-1</sup> )		Co <sub>3</sub> O <sub>4</sub> crystallite size (nm)	T <sub>10</sub> (°C)	T <sub>50</sub> (°C)	T <sub>90</sub> (°C)
	precursor	catalyst				
CtoN	147	132	11	175	204	224
CtoA	155	129	10	170	200	223
OtoN	5	68	19	201	239	299
OtoA	2	71	18	190	226	268
NtoC	164	132	10	172	197	221
AtoC	166	127	9	175	199	221
NtoO	3	71	18	195	222	250
AtoO	2	65	19	197	229	252

Representative SEM micrographs of the precipitated catalysts are shown in Figure 4.8. No differences were apparent between the samples derived from cobalt acetate or cobalt nitrate. In addition, the morphology of each precursor was retained upon calcination. The samples prepared from sodium carbonate (e.g., CtoA catalyst – Figure 4.8 (a)) displayed morphologies and particle sizes similar to those of the samples synthesised by mechanochemical reactions (Chapter 3). The samples comprised irregularly shaped particles of a very broad range of sizes from 1-100 μm. In contrast, when oxalic acid was used as the precipitating agent, the samples presented a very different morphology (e.g., OtoN catalyst, Figure 4.8 (b) and (c)). The precursors and catalysts were comprised of needles 10–15 μm in length and 0.5–2 μm in diameter. Similar needle, rod or wire structures have been reported previously for cobalt oxalate samples<sup>3, 4, 15</sup>. A TEM study of cobalt oxide nanorods found that each

rod was composed of many irregularly shaped smaller  $\text{Co}_3\text{O}_4$  nanoparticles<sup>16</sup>. The needles shown in Figure 4.8 may also be made up of smaller  $\text{Co}_3\text{O}_4$  particles. This would correlate with the both the average crystallite size of the catalyst, which is much smaller than the particle sizes observed by SEM, and the large increase in surface area seen upon calcination of the precursor. The difference in morphology between the cobalt oxalate samples prepared by precipitation and by mechanochemical reaction (Figure 3.33, Chapter 3) is interesting to note.

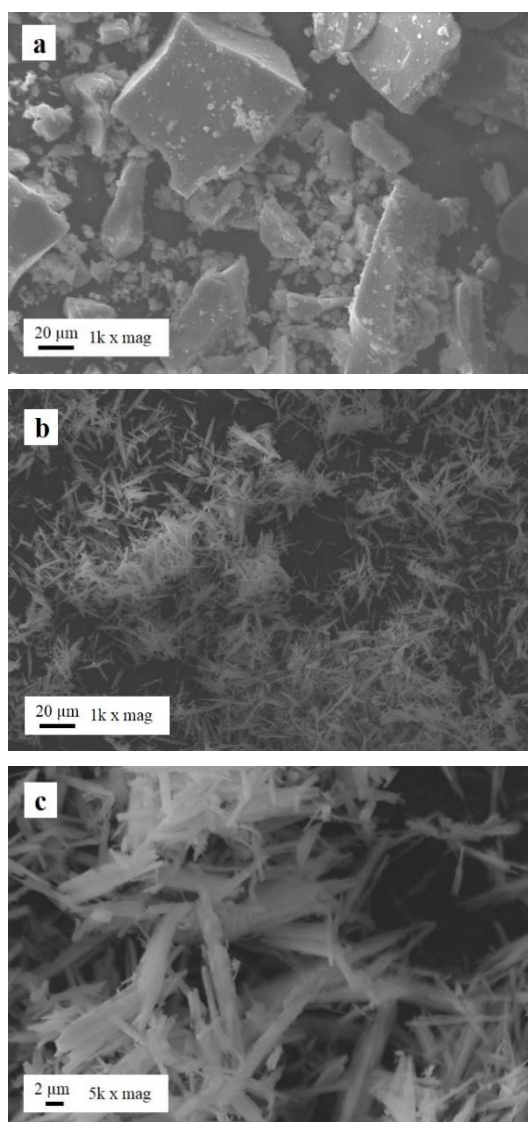


Figure 4.8 – SEM micrographs of (a) CtoA at 1k x mag, (b) OtoN at 1k x mag and (c) OtoN at 5k x mag

The activity of the catalysts for the total oxidation of propane is shown in Figure 4.9 (i) (a) and (b) and the temperatures required for 10, 50 and 90% conversion are reported in Table 4.2. The sodium carbonate-derived catalysts were more active than the oxalic acid-derived catalysts.

Similar activities were observed for all catalysts prepared from sodium carbonate irrespective of the order of addition of the starting materials or the identity of the cobalt salt. For these catalysts, conversions of 10, 50 and 90% propane were attained at *ca.* 173, 200 and 222°C, respectively, and 100% conversion was achieved by 275°C. The catalysts prepared by Co to PA precipitation demonstrated slightly higher propane conversions at 225°C.

Of the oxalic acid-derived catalysts, those prepared by Co to PA precipitation (NtoO and AtoO) were the most active but required temperatures approximately 25°C higher than the sodium carbonate-derived catalysts for similar levels of propane conversion: 10, 50 and 90% conversions were achieved at *ca.* 196, 226 and 251°C, respectively. The OtoA catalyst, prepared by PA to Co precipitation, displayed similar low temperature activity to the Co to PA catalysts, but was less active at higher temperatures, attaining 90% conversion at 268°C. The OtoN catalyst displayed the lowest activity at all temperatures and did not achieve 100% propane conversion by 325°C.

The selectivity of the catalysts towards CO<sub>2</sub> is shown in Figure 4.9 (ii). Propene was produced over the catalysts at low propane conversions, and selectivity to CO<sub>2</sub> increased with conversion. No other reaction products were observed.

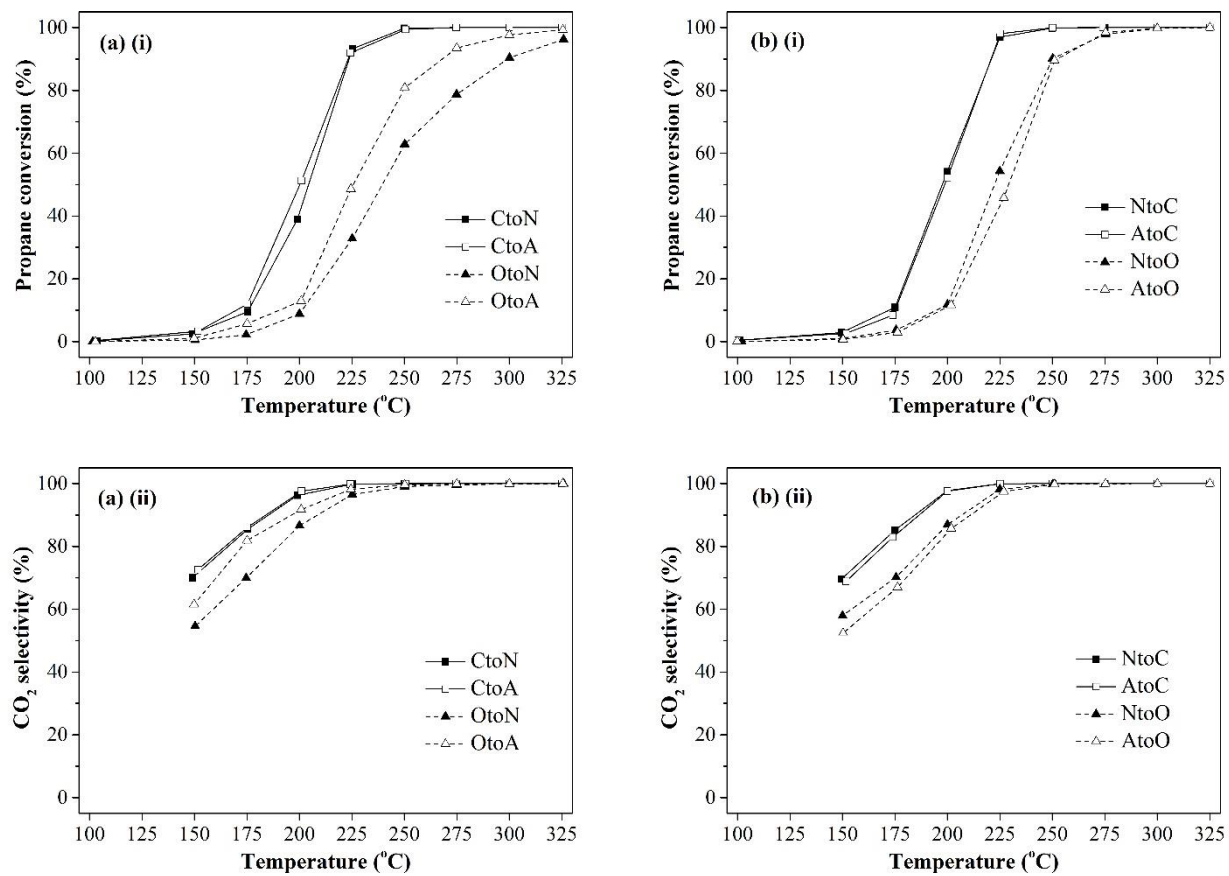


Figure 4.9 – (i) Propane conversion and (ii) CO<sub>2</sub> selectivity over Co<sub>3</sub>O<sub>4</sub> catalysts: (a) PA to Co catalysts and (b) Co to PA catalysts

Precipitation involves three main steps<sup>17</sup>: nucleation (defined as the “formation of the smallest elementary particles of the new phase which are stable under the precipitation conditions”<sup>18</sup>), particle growth and aging. A number of precipitation parameters may influence the processes occurring during these steps and hence affect the final precipitate<sup>19</sup>.

Four starting materials were investigated for the precipitation of  $\text{Co}_3\text{O}_4$  precursors. Different cobalt salts have previously been observed to give rise to precipitates with different morphologies, such as needles from cobalt nitrate but hexagonal plates from cobalt chloride upon precipitation with urea<sup>9</sup>. Nonetheless, the samples prepared with nitrate or acetate counter ions in this work were very similar. The pH at which the precipitates formed by the reaction of oxalic acid were aged was dependent upon the cobalt salt used in the reaction, with cobalt nitrate giving rise to a more acidic solution than cobalt acetate, but this did not alter the properties of the resultant samples.

The identity of the precipitating agent was found to have a much stronger influence on the properties of the precursors and catalysts, with sodium carbonate generating far more active catalysts than oxalic acid. This is in contrast to the similar activities observed for the cobalt hydroxycarbonate- and cobalt oxalate-derived catalysts prepared by mechanochemical reaction in Chapter 3. The differences in activity are likely due to the lower surface area and larger crystallite size of the catalysts from precipitated cobalt oxalate, which could have arisen due to the different morphology of these samples. Irregular agglomerated particles were observed for the oxalate samples produced by grinding, but anisotropic crystallite growth of the oxalate occurred in solution to give needle-shaped particles. Anisotropic growth of the

mechanochemically produced oxalate may have been impeded by the lack of solvent or fragmentation of the growing crystals may have occurred during repeated collisions between the pestle, mortar and reaction mixture<sup>19</sup>. Calcination of the oxalate precursors is believed to produce smaller  $\text{Co}_3\text{O}_4$  particles, but for the creation of catalysts with the desired high surface area and small crystallite size, precipitated cobalt oxalate does not seem to be a suitable precursor.

The order of addition of the starting materials was also investigated as differences in morphology, crystallite size, surface area and surface chemistry have been reported upon changing this parameter, such as in the precipitation of cerium oxide precursors from cerium nitrate and ammonia<sup>20</sup>. For PA to Co experiments the cobalt salt was in excess until complete addition of the precipitating agent, whilst the precipitating agent was in excess during Co to PA experiments. The initial pH of the reaction solution depended on the reagent which was initially in excess, but as each set of starting materials was reacted on a 1:1 molar ratio, the pH achieved upon total addition of the two solutions was similar irrespective of the order of addition. The resulting precursors and catalysts could not be distinguished by TGA-DTA, XRD, FT-IR, SEM or surface area analysis, however the catalysts prepared by Co to PA precipitation were more active than those prepared by PA to Co precipitation. Other characteristics may be responsible for differences in activity – these are discussed in more detail in *Section 4.3*. As the main focus of this chapter was the synthesis of catalyst precursors, fewer techniques were utilised for characterisation of the catalysts.

### 4.2.3 Conclusions

Precipitation was found to give cobalt hydroxycarbonate hydrate and cobalt oxalate hydrate precursors in high purity. Thermal decomposition of the precursors gave rise to  $\text{Co}_3\text{O}_4$  catalysts which demonstrated good propane total oxidation activity. The identity of the cobalt salt used in precipitation was not found to influence activity but less active catalysts resulted from PA to Co precipitation compared to Co to PA precipitation. No differences in the properties of the precursors or catalysts were found to explain these differences. The lower activity of the catalysts derived from cobalt oxalate precursors was attributed to the lower surface area and larger crystallite size of these samples compared to the cobalt hydroxycarbonate-derived samples.

### 4.3 Investigation of variables in the precipitation of cobalt hydroxycarbonate hydrate from cobalt acetate

In *Section 4.2* little difference in activity was observed between the catalysts synthesised by the reaction of sodium carbonate with different cobalt salts. Nitrate-free synthesis routes are desirable as they avoid environmentally harmful wastewater streams<sup>21</sup>. On the basis of this, and the higher activity observed for Co to PA catalysts at elevated temperatures, further experiments have been performed to investigate the influence of precipitation variables on samples synthesised by the addition of cobalt acetate solutions to carbonate solutions. Molar ratio, solution concentration, precipitate aging time and the counter ion of the carbonate have been investigated, as these factors may influence the morphology, texture or structure of precipitates<sup>18</sup>. Throughout this section, the prepared samples are compared to AtoC from *Section 4.2*, which was synthesised by the addition of an aqueous solution of cobalt acetate

(0.25 M) to an aqueous solution of sodium carbonate (0.25 M) with an aging time of 2 h.

#### **4.3.1 Preparation**

In the preparation of all samples, aqueous solutions of cobalt acetate were added to aqueous carbonate solutions according to the method described in *Section 2.1.1.2*.

To investigate the effect of molar ratio, the concentration of the cobalt acetate solution was kept constant at 0.25 M and the concentration of the sodium carbonate solution was changed to 0.5 or 1 M to give molar ratios of 1:2 or 1:4, respectively. The precipitates were aged for 2 h.

To investigate the effect of solution concentration, the molar ratio of cobalt acetate to sodium carbonate was kept constant at 1:1 and the solutions were prepared with concentrations of 0.1 or 1 M. The precipitates were aged for 2 h.

To investigate the effect of aging time, the concentrations of the cobalt acetate and sodium carbonate solutions were kept constant at 0.25 M and the molar ratio was kept constant at 1:1. The precipitates were aged for 0.25 or 6 h.

To investigate the effect of the carbonate counter ion, the cobalt acetate solution (0.25 M) was reacted with solutions of potassium carbonate or ammonium carbonate (0.25 M) in a 1:1 molar ratio. The precipitates were aged for 2 h.

In all cases, the precursors were calcined for 2 h at 300°C with a heating rate of 10°C min<sup>-1</sup> in open air. This information and the nomenclature of the prepared samples are summarised in Table 4.3.

The pH values of the starting solutions and the reaction solutions before and after aging are also reported in Table 4.3. With the exception of the molar ratio experiments, no significant differences in pH were observed between the reaction solutions of AtoC and those prepared under different conditions. Each solution presented a value of *ca.* pH.7.3 before aging, which rose to *ca.* pH 7.7 after aging. For AtoC-1:2 and AtoC-1:4 the excess carbonate resulted in more basic reaction solutions of *ca.* pH 9 and 10, respectively, which did not alter considerably with aging.

Table 4.3 – Sample nomenclature and pH values

Sample	Order of addition	Cobalt acetate solution		Precipitating agent solution			Molar ratio	Aging time (h)	Reaction solution pH	
		conc (M)	initial pH	agent	conc (M)	initial pH			before aging	after aging
AtoC	Co to PA	0.25	7.3	Na <sub>2</sub> CO <sub>3</sub>	0.25	11.6	1:1	2	7.2	7.7
AtoC-1:2	Co to PA	0.25	7.2	Na <sub>2</sub> CO <sub>3</sub>	0.5	11.7	1:2	2	9.3	9.4
AtoC-1:4	Co to PA	0.25	7.3	Na <sub>2</sub> CO <sub>3</sub>	1	11.8	1:4	2	10.0	10.0
AtoC-0.1M	Co to PA	0.1	7.6	Na <sub>2</sub> CO <sub>3</sub>	0.1	11.6	1:1	2	7.5	7.7
AtoC-1M	Co to PA	1	6.5	Na <sub>2</sub> CO <sub>3</sub>	1	11.9	1:1	2	7.4	7.5
AtoC-15min	Co to PA	0.25	7.4	Na <sub>2</sub> CO <sub>3</sub>	0.25	11.6	1:1	0.25	7.2	7.4
AtoC-6h	Co to PA	0.25	7.4	Na <sub>2</sub> CO <sub>3</sub>	0.25	11.6	1:1	6	7.3	8.0
AtoPC	Co to PA	0.25	7.3	K <sub>2</sub> CO <sub>3</sub>	0.25	11.8	1:1	2	7.3	7.9
AtoAC	Co to PA	0.25	7.3	(NH <sub>4</sub> ) <sub>2</sub> CO <sub>3</sub>	0.25	9.3	1:1	2	7.2	7.5

### 4.3.2 Results and Discussion

The XRD patterns and FT-IR spectra of the precursors are shown in Figure 4.10. The patterns and spectra of the precursors precipitated under different conditions were very similar to those of AtoC. Each precursor could be assigned as poorly crystalline hydrated cobalt hydroxycarbonate,  $(\text{Co}(\text{OH})_x(\text{CO}_3)_{0.5(2-x)} \cdot n\text{H}_2\text{O})$ .

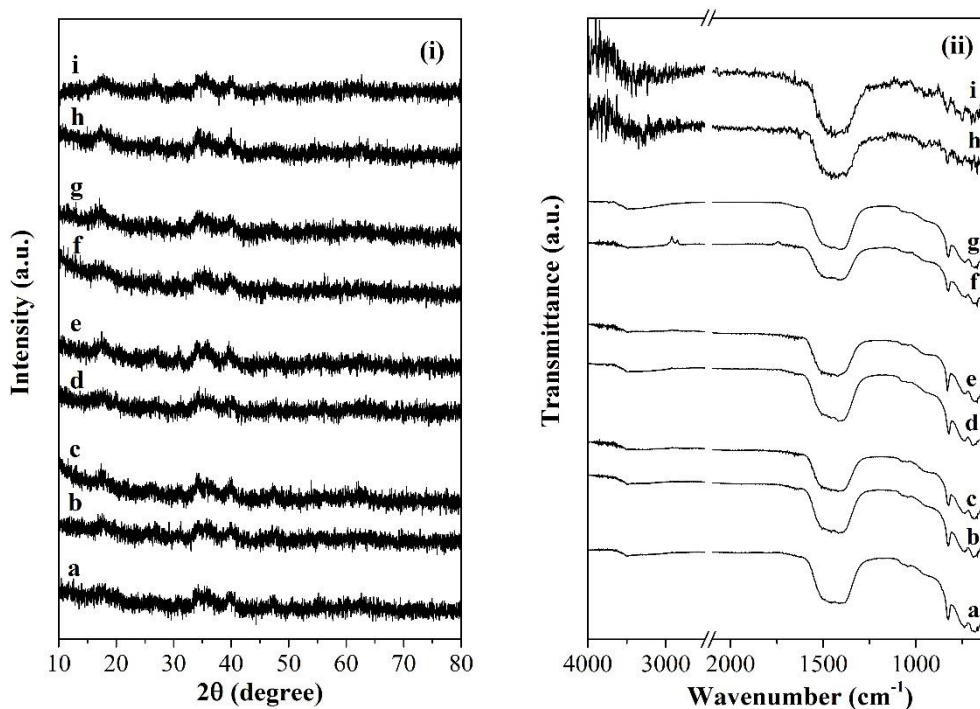


Figure 4.10 – (i) XRD patterns and (ii) FT-IR spectra of precursors  
 (a) AtoC, (b) AtoC-1:2, (c) AtoC-1:4, (d) AtoC-0.1M, (e) AtoC-1M, (f) AtoC-15min, (g) AtoC-6h,  
 (h) AtoPC and (i) AtoAC

The TGA-DTA curves of the precursors are shown in Figure 4.11. The profiles and observed total weight loss of 23.3-25.2% corresponded to the decomposition of hydrated cobalt hydroxycarbonate to  $\text{Co}_3\text{O}_4$ , as described for the AtoC precursor in Section 4.2. The two separate exothermic peaks associated with the main weight loss step at *ca.* 240°C were more clearly distinguished in the DTA curves of the AtoC-1M and AtoAC precursors but no other significant differences were observed between the curves.

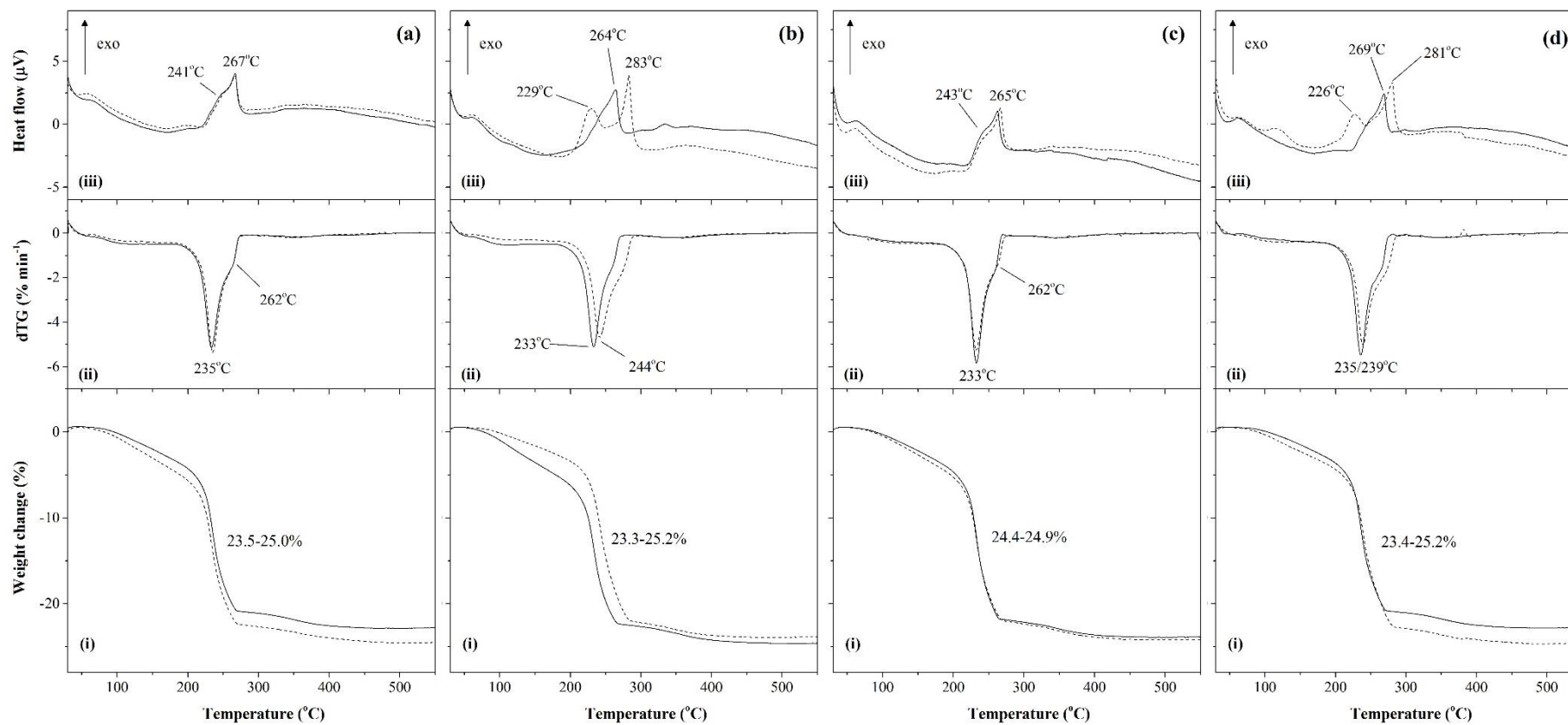


Figure 4.11 – (i) TGA, (ii) DTG and (iii) DTA curves of precursors  
 (a) AtoC-1:2 (solid line) and AtoC-1:4 (dashed line), (b) AtoC-0.1M (solid line) and AtoC-1M (dashed line),  
 (c) AtoC-15min (solid line) and AtoC-6h (dashed line), (d) AtoPC (solid line) and AtoAC (dashed line)

Based on the results of the TGA experiments, the precursors were calcined at 300°C for 2 hours with a heating rate of 10°C min<sup>-1</sup> and the XRD patterns of the resulting catalysts are shown in Figure 4.12. The pattern of each catalyst corresponded to the Co<sub>3</sub>O<sub>4</sub> phase of cobalt oxide and the average crystallite size of each catalyst was determined to be 9-11 nm (reported in Table 4.4).

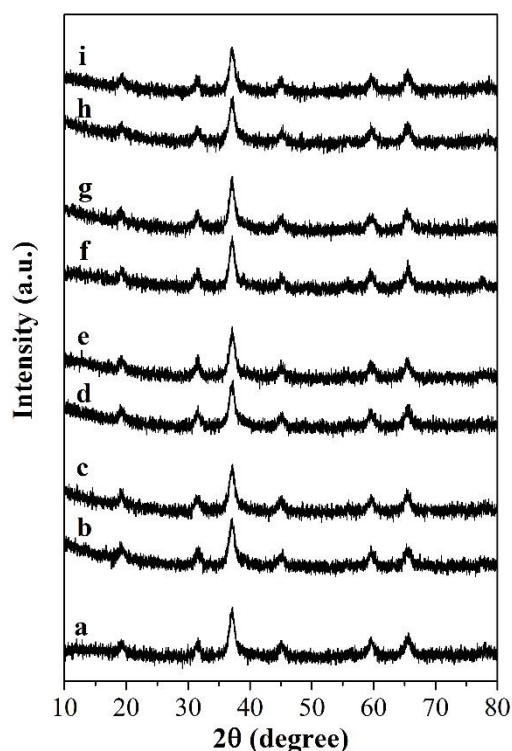


Figure 4.12 – XRD patterns of catalysts (a) AtoC, (b) AtoC-1:2, (c) AtoC-1:4, (d) AtoC-0.1M, (e) AtoC-1M, (f) AtoC-15min, (g) AtoC-6h, (h) AtoPC and (i) AtoAC

The BET surface areas of the precursors and catalysts are reported in Table 4.4. High surface areas of 147 m<sup>2</sup> g<sup>-1</sup> or above were observed for all precursors. The surface area of each calcined sample was observed to be *ca.* 130 m<sup>2</sup> g<sup>-1</sup>.

SEM analysis of the precursors and catalysts revealed that the morphologies and range of particle sizes of all of the samples were similar to those of AtoC, which was shown in Figure 4.8 (c).

Table 4.4 – Physicochemical characteristics of samples and catalytic activity

Sample	Surface area (m <sup>2</sup> g <sup>-1</sup> )		Co <sub>3</sub> O <sub>4</sub> crystallite size (nm)	T <sub>10</sub> (°C)	T <sub>50</sub> (°C)	T <sub>90</sub> (°C)
	precursor	catalyst				
AtoC	166	127	9	175	199	221
AtoC-1:2	166	135	9	176	205	242
AtoC-1:4	162	134	9	173	200	236
AtoC-0.1M	173	135	10	175	202	222
AtoC-1M	147	127	9	170	205	228
AtoC-15min	169	128	10	177	217	267
AtoC-6h	176	125	9	180	214	245
AtoPC	162	134	11	175	207	243
AtoAC	151	132	9	177	204	223

The activity of the catalysts for the total oxidation of propane is shown in Figures 4.13 and 4.14 (i) (a) and (b) and the temperatures required for 10, 50 and 90% conversion are reported in Table 4.4.

Each of the catalysts synthesised with different molar ratios of cobalt acetate to sodium carbonate (Figure 4.13 (i) (a)) initially demonstrated similar activities, achieving 10 and 50% propane conversions at *ca.* 175 and 201°C, respectively. However, the catalysts prepared with excess sodium carbonate were less active than the 1:1 AtoC catalyst at higher temperatures, reaching 90% conversion at a temperature approximately 20°C higher than AtoC (at *ca.* 240°C).

The catalysts prepared from solutions of different concentrations (Figure 4.13 (i) (b)) displayed similar activities at all temperatures, with little deviation from the activity observed for AtoC.

The greatest change in activity compared to AtoC was observed for the catalysts prepared from precipitates that were aged for different periods of time (Figure 4.14 (i) (a)). Both a reduced aging time of 15 minutes and an extended aging time of 6 hours resulted in less active catalysts than the standard 2 hour aging time utilised for the AtoC reference catalyst. These catalysts achieved 10% propane conversion at a similar temperature to AtoC (*ca.* 178°C), but for 50% conversion a temperature approximately 15°C higher (*ca.* 216°C) was required, and 90% conversion was obtained at temperatures approximately 25-45°C higher (245-267°C). The least active catalyst was prepared by aging for 15 minutes.

Of the samples prepared from different carbonates (Figure 4.14 (i) (b)), the catalyst synthesised from ammonium carbonate presented a similar activity to the catalyst synthesised from sodium carbonate at all temperatures. A lower activity was observed for the catalyst synthesised from potassium carbonate at higher temperatures: AtoPC achieved 90% propane conversion at a temperature approximately 20°C greater (243°C) than the other two catalysts.

The selectivity of the catalysts towards CO<sub>2</sub> is shown in Figures 4.13 and 4.14 (ii) (a) and (b). Propene was produced over the catalysts at low propane conversions, and selectivity to CO<sub>2</sub> increased with conversion. No other reaction products were observed.

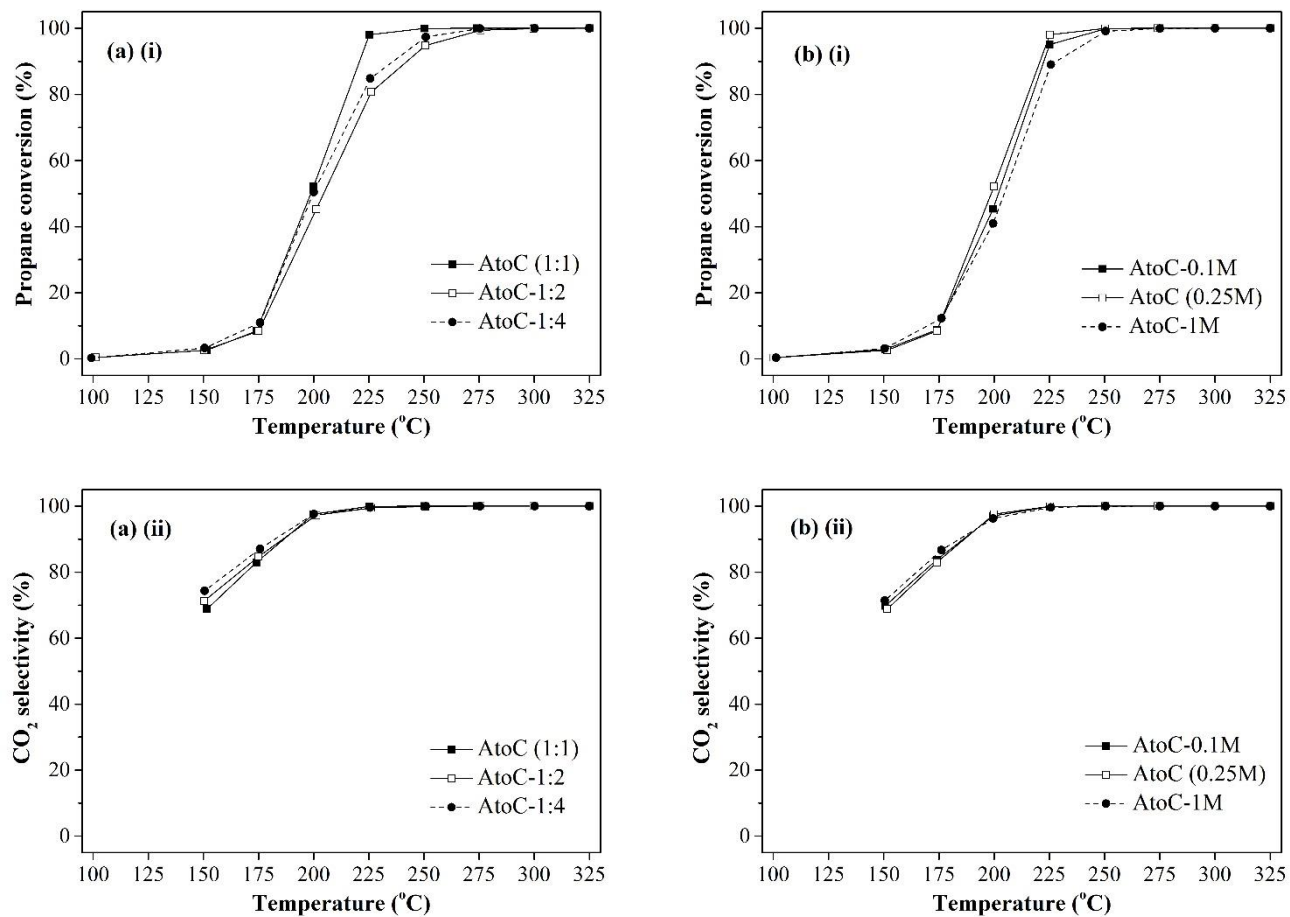


Figure 4.13 – (i) Propane conversion and (ii) CO<sub>2</sub> selectivity over Co<sub>3</sub>O<sub>4</sub> catalysts:  
 (a) molar ratio catalysts and (b) solution concentration catalysts

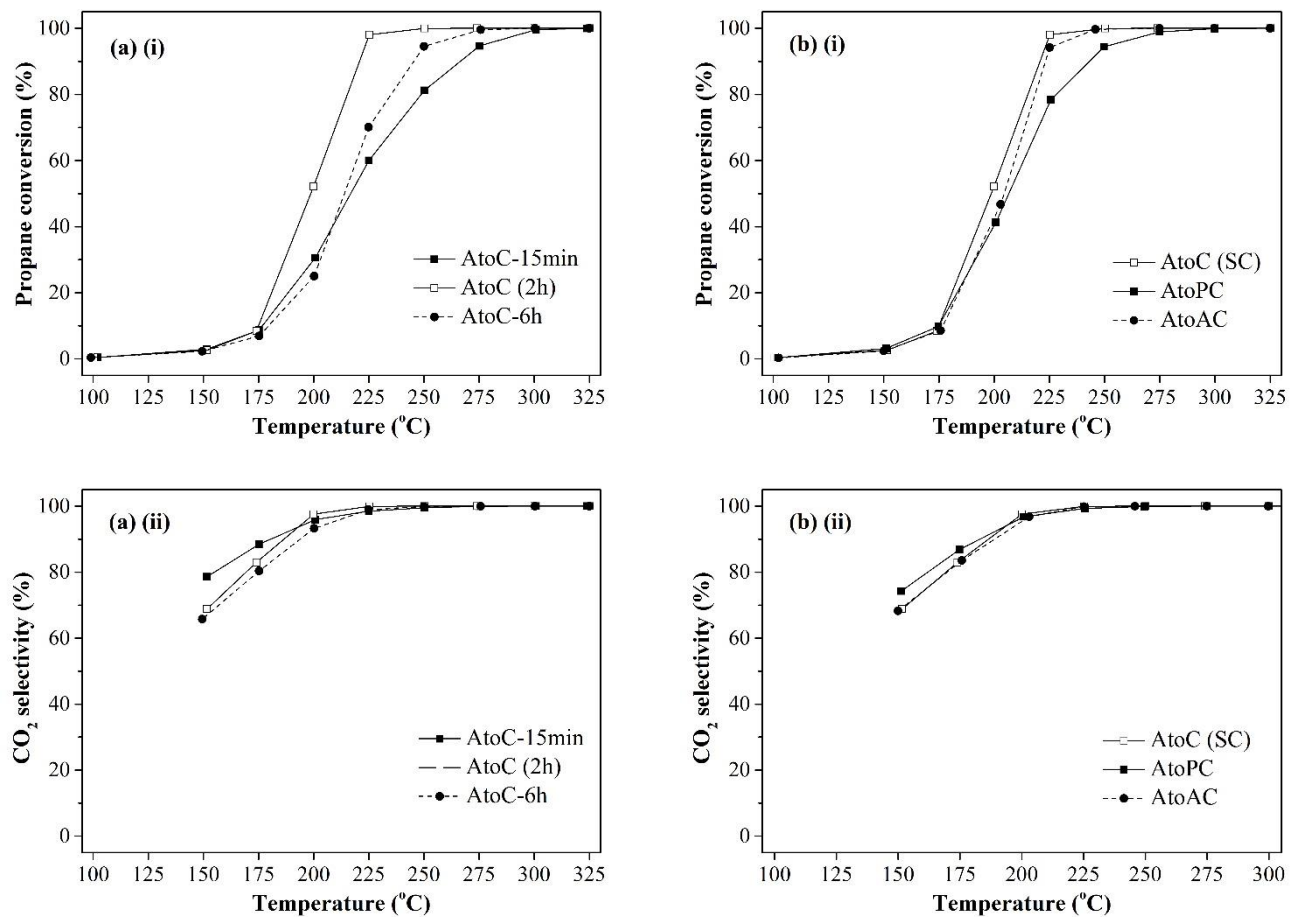


Figure 4.14 – (i) Propane conversion and (ii) CO<sub>2</sub> selectivity over Co<sub>3</sub>O<sub>4</sub> catalysts:  
 (a) aging time catalysts and (b) alternative carbonate catalysts

The activity of the most active of these precipitated catalysts was comparable to the activity of the mechanochemically-derived catalysts reported in Chapter 3. Precipitated cobalt hydroxycarbonate has previously been reported as a precursor for  $\text{Co}_3\text{O}_4$  catalysts utilised for the total oxidation of propane<sup>22, 23</sup>. The catalysts reported in the literature displayed lower activities than those reported herein, but as the precursors were calcined at different temperatures a direct comparison is not appropriate.

The stability of the AtoC catalyst with time-on-line was investigated at a reaction temperature of 215°C and the results are shown in Figure 4.15. Throughout the experiment the conversion of propane remained relatively constant at *ca.* 92% and the catalyst displayed a consistent selectivity to  $\text{CO}_2$  of greater than 99%. No deactivation was detected after 42.5 hours on-line.

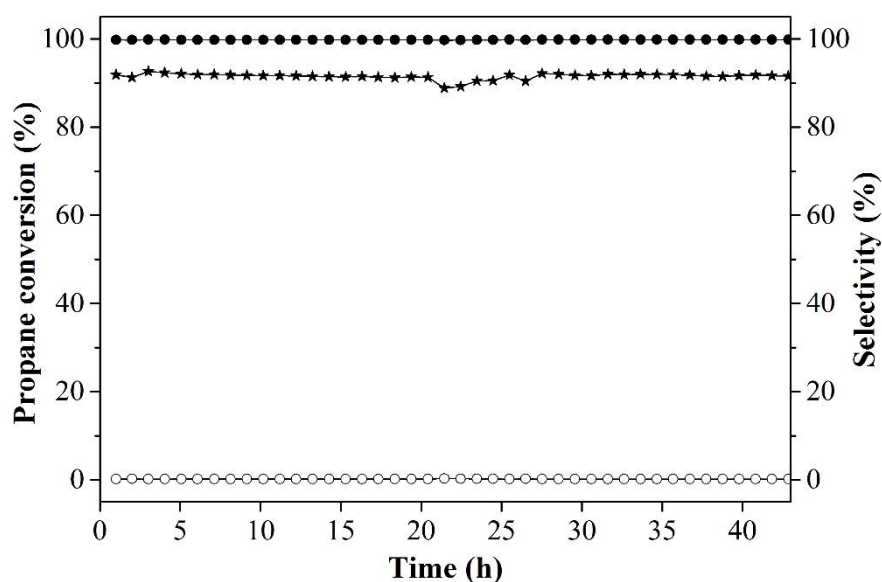


Figure 4.15 – Propane oxidation over AtoC with time-on-line at 215 °C. Star = propane conversion, filled circle = selectivity to  $\text{CO}_2$ , open circle = selectivity to propene.

It was anticipated that varying the molar ratio of the starting materials may lead to the precipitation of different phases such as cobalt hydroxide or cobalt carbonate.

Nevertheless, the formation of the hydroxycarbonate phase in all cases (AtoC (1:1), AtoC-1:2 and AtoC-1:4) fits with the report that precipitation of the hydroxycarbonate is thermodynamically more likely than precipitation of cobalt hydroxide<sup>24</sup>. Similarly, hydroxycarbonates have been reported to form preferentially over cobalt carbonate at room temperature<sup>25</sup>. During the molar ratio study, the initial pH of the sodium carbonate solution did not vary greatly with concentration, with all solutions presenting a value of *ca.* pH 11.7 (Table 4.3). Upon reaction with cobalt acetate, the excess carbonate in the 1:2 and 1:4 experiments resulted in more basic reaction solutions than observed for the 1:1 experiment by approximately 1.5 and 2.5 pH units. The pH of the solution during reaction and aging has been shown to influence the crystallinity of hydroxycarbonates, such as in the precipitation of Cu/Zn/Al oxide precursors where crystallinity increased with pH<sup>26</sup>. In this work, despite the differences in pH values, all three of the precipitated cobalt hydroxycarbonate hydrate precursors presented very similar XRD patterns (Figure 4.10) and no change in crystallinity was observed.

Precipitation from solutions of different concentrations was performed to investigate the influence of supersaturation. More concentrated solutions give rise to higher degrees of supersaturation. Typically under these conditions nucleation occurs at a faster rate than particle growth which results in the production of a greater number of smaller particles and a higher surface area<sup>19</sup>. Less concentrated solutions may give rise to larger particles and a lower surface area due to the faster rate of growth compared to nucleation. Nonetheless, no clear difference in crystallinity with changing concentration was observed between the XRD patterns (Figure 4.10) of the precursors prepared with different solution concentrations (AtoC-0.1 M, AtoC (0.25 M) and

AtoC-1 M). Likewise, the samples displayed similar surface areas, ranging only slightly outside the limits of experimental error (Table 4.4). Whilst the differences between the studied concentrations may have been too small to effect changes, the similarity between the precipitates could be attributed to a very small critical nucleation size for this compound<sup>18</sup>. The broad diffraction peaks observed in the XRD patterns of each of the precursors are in keeping with the precipitation of a poorly organised phase, which typically occurs for a small critical nucleus<sup>18</sup>. For each of the solution concentrations investigated, nucleation would have occurred at a faster rate than crystal growth.

The duration for which the precipitates were aged was investigated as processes that alter the nature of the precipitate, such as transformation of crystalline phases or Ostwald ripening, may occur during aging<sup>18, 19</sup>. In a study of the precipitation of zinc oxide precursors, the hydroxycarbonate was identified as the thermodynamically stable product and a different phase could only be identified by quenching the reaction mixture immediately after addition of the reactants<sup>27</sup>. The relatively fast formation of a stable phase would explain why only the cobalt hydroxycarbonate hydrate phase was observed in this work irrespective of the precipitate aging time (AtoC-15 min, AtoC (2 h) and AtoC-6 h). Based on the similar surface areas observed for the three precursors (Table 4.4), it appears that no Ostwald ripening occurred during aging. This process involves the dissolution of smaller crystals but the continued growth of larger crystals, and gives rise to a precipitate with a larger overall particle size<sup>18</sup>.

Precipitation from alternative carbonates was performed to determine the impact of the counter ion. Cobalt hydroxycarbonate hydrate was formed upon reaction of cobalt

acetate with all three of the carbonates (AtoC (SC), AtoPC and AtoAC). Whilst sodium or potassium impurities may have persisted following calcination, residual ammonium carbonate would have been removed during heat treatment as it decomposes to ammonia, carbon dioxide and water at temperatures of 100°C or lower<sup>28</sup>. Based on the comparable surface areas observed for each of the precursors (and catalysts), impurities from the reaction solution did not appear to be present on the samples to any great extent.

As expected from the similarity of the precipitates formed under each of the different reaction conditions, the catalysts formed upon calcination of the precursors presented similar surface areas and crystallite sizes and hence comparable catalytic activity was observed for the majority of the samples. The lack of variation between the samples could be attributed to the limited number of variables investigated for each given parameter, but overall suggests that the precipitation of cobalt hydroxycarbonate hydrate is very robust.

Where variation in catalytic activity was observed (in particular for the hydroxycarbonate samples prepared with different aging times and the oxalate samples from *Section 4.2*), a number of other features may account for the differences. Surface modifications have been reported to occur during aging<sup>29</sup> so XPS and FT-IR studies may show differences in the surface chemistry of the samples, such as the strength of the Co-O bond or the presence of impurities. TEM may indicate differences in morphology or agglomeration which could not be observed with low magnification SEM. Measuring the particle size distribution by laser diffraction may demonstrate variations between the samples. In the case of the hydroxycarbonate precursors, CHN

analysis could indicate if the proportions of carbonate and hydroxyl groups present in the precipitates altered with reaction conditions. Such a change has previously been reported for hydroxycarbonates aged for different lengths of time<sup>1</sup>.

### **4.3.3 Conclusions**

The propane total oxidation activity of the AtoC catalyst (prepared from cobalt acetate and sodium carbonate) could be equalled but not improved by altering the conditions of precipitation. The precipitation of cobalt hydroxycarbonate hydrate was found to be very robust, with similar precursors and catalysts resulting despite variations in a number of parameters. Under the experimental conditions considered, the molar ratio of reactants, the solution concentrations and the identity of the carbonate counter ion were discovered to have little effect on the final products. The duration for which the precipitates were aged was determined to have the greatest influence on catalytic activity, but further characterisation of the samples would be required to account for these differences.

## **4.4 Chapter conclusions**

A range of precipitation parameters were studied in the synthesis of cobalt oxide precursors. High purity precipitates were synthesised in all cases and stable  $\text{Co}_3\text{O}_4$  catalysts were formed upon thermal decomposition. Cobalt hydroxycarbonate hydrate was found to be the most suitable  $\text{Co}_3\text{O}_4$ -precursor due to the higher surface areas and smaller crystallite sizes of the final catalysts compared to the cobalt oxalate hydrate-derived catalysts. The precipitation of cobalt hydroxycarbonate hydrate was found to be very robust. As observed in Chapter 3, surface area and crystallite size are

important parameters in determining the activity of  $\text{Co}_3\text{O}_4$  catalysts, but other features must be considered to account for variations in activity.

#### 4.5 References

1. P. Kowalik, M. Konkol, K. Antoniak, W. Prochniak and P. Wiercioch, *J. Mol. Catal. A-Chem.*, 2014, **392**, 127-133.
2. B. X. Li, Y. Xie, C. Z. Wu, Z. Q. Li and J. Zhang, *Mater. Chem. Phys.*, 2006, **99**, 479-486.
3. W. A. Ang, Y. L. Cheah, C. L. Wong, R. Prasanth, H. H. Hng and S. Madhavi, *J. Phys. Chem. C*, 2013, **117**, 16316-16325.
4. J. Ahmed, T. Ahmad, K. V. Ramanujachary, S. E. Lofland and A. K. Ganguli, *Journal of Colloid and Interface Science*, 2008, **321**, 434-441.
5. R. Xu and H. C. Zeng, *J. Phys. Chem. B*, 2003, **107**, 12643-12649.
6. M. A. Gabal, A. A. El-Bellihi and S. S. Ata-Allah, *Mater. Chem. Phys.*, 2003, **81**, 84-92.
7. P. Román, C. Guzmán-Miralles, A. Luque, J. I. Beitia, J. Cano, F. Lloret, M. Julve and S. Alvarez, *Inorg. Chem.*, 1996, **35**, 3741-3751.
8. H. Luo, D. B. Zou, L. G. Zhou and T. K. Ying, *J. Alloy. Compd.*, 2009, **481**, L12-L14.
9. T. Ishikawa and E. Matijevic, *Colloid Polym. Sci.*, 1991, **269**, 179-186.
10. M. Behrens, F. Girgsdies, A. Trunschke and R. Schlögl, *Eur. J. Inorg. Chem.*, 2009, 1347-1357.
11. G. Salek, P. Alphonse, P. Dufour, S. Guillemet-Fritsch and C. Tenailleau, *Appl. Catal. B-Environ.*, 2014, **147**, 1-7.
12. M. C. Lopez, J. L. Tirado and C. P. Vicente, *J. Power Sources*, 2013, **227**, 65-71.
13. P. Dutta, M. S. Seehra, S. Thota and J. Kumar, *J. Phys.-Condes. Matter*, 2008, **20**, 8.
14. D. Dollimore and D. Nicholson, *Journal of the Chemical Society*, 1962, 960-&.
15. B. de Rivas, R. Lopez-Fonseca, C. Jimenez-Gonzalez and J. I. Gutierrez-Ortiz, *Chem. Eng. J.*, 2012, **184**, 184-192.
16. D. W. Wang, Q. H. Wang and T. M. Wang, *Inorg. Chem.*, 2011, **50**, 6482-6492.
17. C. P. M. Roelands, J. H. ter Horst, H. J. M. Kramer and P. J. Jansens, *Cryst. Growth Des.*, 2006, **6**, 1380-1392.
18. J. A. Schwarz, C. Contescu and A. Contescu, *Chem. Rev.*, 1995, **95**, 477-510.
19. *Handbook of Heterogeneous Catalysis*, Wiley-VCH, Weinheim, 2008.
20. V. Morris, P. G. Fleming, J. D. Holmes and M. A. Morris, *Chem. Eng. Sci.*, 2013, **91**, 102-110.
21. M. Behrens, S. Kissner, F. Girgsdies, I. Kasatkin, F. Hermerschmidt, K. Mette, H. Ruland, M. Muhler and R. Schlögl, *Chem. Commun.*, 2011, **47**, 1701-1703.
22. Q. Liu, L. C. Wang, M. Chen, Y. Cao, H. Y. He and K. N. Fan, *Journal of Catalysis*, 2009, **263**, 104-113.

23. B. Solsona, T. Garcia, G. J. Hutchings, S. H. Taylor and M. Makkee, *Appl. Catal. A-Gen.*, 2009, **365**, 222-230.
24. G. L. Bezemer, P. B. Radstake, V. Koot, A. J. van Dillen, J. W. Geus and K. P. de Jong, *Journal of Catalysis*, 2006, **237**, 291-302.
25. S. Lacour, R. P. Van Hille, K. Peterson and A. E. Lewis, *Aiche J.*, 2005, **51**, 2358-2368.
26. G. Simson, E. Prasetyo, S. Reiner and O. Hinrichsen, *Appl. Catal. A-Gen.*, 2013, **450**, 1-12.
27. S. Kaluza and M. Muhler, *Catalysis Letters*, 2009, **129**, 287-292.
28. A. K. Galwey and M. E. Brown, *Thermal Decomposition of Ionic Solids*, Elsevier Science, Amsterdam, 1999.
29. T. Baird, K. C. Campbell, P. J. Holliman, R. W. Hoyle, D. Stirling, B. P. Williams and M. Morris, *J. Mater. Chem.*, 1997, **7**, 319-330.

# Chapter 5

## Silica supported cobalt catalysts for the total oxidation of propane

### 5.1 Introduction

In this chapter fumed silica ( $\text{SiO}_2$ ) is utilised as a catalyst support. Deposition precipitation, wet impregnation, and powder blending techniques are initially investigated to find a suitable method for supporting  $\text{Co}_3\text{O}_4$ . As wet impregnation from cobalt nitrate is found to give the most active supported catalyst, the influence of weight loading is then studied for catalysts prepared by this method. The catalysts are characterised by a range of techniques and tested for the total oxidation of propane.

### 5.2 Investigation of preparation methods for supporting $\text{Co}_3\text{O}_4$ on silica

#### 5.2.1 Preparation

Initial experiments investigated the suitability of different preparation methods to yield active catalysts composed of 5 wt%  $\text{Co}_3\text{O}_4$  supported on  $\text{SiO}_2$  (equivalent to 3.7 wt%  $\text{Co}/\text{SiO}_2$ ). Deposition precipitation (DP), wet impregnation (Imp) and powder blending (PB) experiments were performed according to the methods described in *Section 2.1.2*. In all cases the precursors were calcined for 2 h at  $300^\circ\text{C}$  with a heating rate of  $10^\circ\text{C min}^{-1}$  in open air (no gas flow through an open tubular furnace). The nomenclature and preparation methods of the samples are summarised in Table 5.1.

*N.B.* In contrast to Chapter 3, the uncalcined catalyst precursors and the catalysts have not been named separately in this chapter.

Table 5.1 – Sample nomenclature and preparation methods

Sample	Preparation method	Reaction mixture
DP-hydroxycarbonate	Deposition precipitation	SiO <sub>2</sub> (1 g) + water (200 mL) + cobalt acetate (0.164 g) + sodium carbonate (0.070 g)
DP-oxalate	Deposition precipitation	SiO <sub>2</sub> (1 g) + water (200 mL) + cobalt acetate (0.164 g) + oxalic acid (0.083 g)
Imp-acetate	Wet impregnation	SiO <sub>2</sub> (1 g) + water (50 mL) + cobalt acetate (0.164 g)
Imp-nitrate	Wet impregnation	SiO <sub>2</sub> (1 g) + water (50 mL) + cobalt nitrate (0.192 g)
PB-hydroxycarbonate	Powder blending	SiO <sub>2</sub> (1 g) + water (50 mL) + cobalt hydroxycarbonate hydrate (AtoC precursor) (0.071 g)
PB-Co <sub>3</sub> O <sub>4</sub>	Powder blending	SiO <sub>2</sub> (1 g) + water (50 mL) + cobalt oxide (AtoC catalyst) (0.053 g)
Co <sub>3</sub> O <sub>4</sub> -SiO <sub>2</sub> -mix	Shaking	SiO <sub>2</sub> (1 g) + cobalt oxide (AtoC catalyst) (0.053 g)

Wet impregnation is typically utilised in the synthesis of silica-supported catalysts<sup>1</sup>. Deposition precipitation and powder blending were investigated to determine if the active catalysts prepared by precipitation in Chapter 4 could be supported. Deposition precipitation experiments involved performing precipitation in the presence of the SiO<sub>2</sub> support. The variables utilised in the synthesis of DP-hydroxycarbonate and DP-oxalate were based on the synthesis of the CtoA and OtoA bulk precipitated catalysts, respectively. Powder blending experiments involved mixing the SiO<sub>2</sub> support with pre-made cobalt hydroxycarbonate hydrate or Co<sub>3</sub>O<sub>4</sub>. For the PB-hydroxycarbonate sample, the mass of AtoC precursor required to yield 5 wt% Co<sub>3</sub>O<sub>4</sub>/SiO<sub>2</sub> was calculated from the weight change observed in TGA experiments relating to the transformation of the cobalt hydroxycarbonate hydrate to Co<sub>3</sub>O<sub>4</sub>.

An unsupported sample with a cobalt oxide loading equivalent to 5 wt%  $\text{Co}_3\text{O}_4/\text{SiO}_2$  was prepared by simply shaking together  $\text{Co}_3\text{O}_4$  and silica. Prior to mixing, the cobalt oxide and support were separately subjected to powder blending conditions: the powders were separately stirred in water, dried and calcined. After calcination the two powders were shaken together in a glass vial. The powder mixture was not subjected to any thermal treatment.

### 5.2.2 Results and Discussion

The TGA-DTG-DTA curves of fresh  $\text{SiO}_2$  and the  $\text{Co}/\text{SiO}_2$  precursors heated in an air atmosphere at  $10^\circ\text{C min}^{-1}$  are shown in Figure 5.1. For all of the samples studied an initial increase in weight, which was an artefact caused by the onset of the heating ramp, was followed by a small weight loss until *ca.*  $110^\circ\text{C}$  due to the loss of surface-adsorbed water. The fresh  $\text{SiO}_2$  sample displayed a gradual weight gain of *ca.* 2% with increasing temperature which could be attributed to baseline drift.

The curves of the DP-hydroxycarbonate precursor (Figure 5.1 (a), dashed lines) were in general very similar to those of fresh  $\text{SiO}_2$  (dotted lines), but a greater weight loss was observed at temperatures below  $110^\circ\text{C}$  for DP-hydroxycarbonate due to the loss of a greater amount of water. The conditions used in the synthesis of this sample (cobalt salt to precipitating agent molar ratio, aging time, etc.) were based on the precipitation of the CtoA cobalt hydroxycarbonate hydrate from Chapter 4, but scaled down to give the appropriate cobalt weight loading. In the TGA of bulk CtoA (Figure 4.5 (a)), a weight loss of *ca.* 26% centred at  $250^\circ\text{C}$  was observed. If the same cobalt hydroxycarbonate hydrate species were formed during the preparation of DP-hydroxycarbonate, a weight loss of *ca.* 1.7% would be expected upon

decomposition to  $\text{Co}_3\text{O}_4/\text{SiO}_2$ . Several factors may be responsible for the absence of this decomposition step: Little or no hydroxycarbonate may have formed from the reaction solution. Alternatively, the rising background may have concealed the decomposition. A third possibility is the production of cobalt silicate phases during the initial synthesis which did not undergo thermal decomposition (discussed in more detail below).

The conditions used in the preparation of DP-oxalate were based on the precipitation of bulk OtoA cobalt oxalate hydrate from Chapter 4. The curves of the DP-oxalate precursor (Figure 5.1 (a), solid lines) could be more easily related to those of bulk OtoA (Figure 4.5 (c)). The small weight loss step and weakly endothermic peak centred at  $168^\circ\text{C}$  represented the loss of water of crystallisation from cobalt oxalate hydrate, whilst the larger weight loss step and associated exothermic peak at  $312^\circ\text{C}$  corresponded to the transformation of anhydrous cobalt oxalate to  $\text{Co}_3\text{O}_4^2$ . The total observed weight loss of *ca.* 2% was lower than the theoretical value of 6% (based on the formation of  $\text{CoC}_2\text{O}_4 \cdot 2\text{H}_2\text{O}$ ), which may again be due to the rising background, incomplete precipitation of cobalt from solution or the formation of alternative phases.

In the decomposition of the Imp-acetate precursor (Figure 5.1 (b), dashed lines), the weight loss of *ca.* 1.8% centred at  $285^\circ\text{C}$  was ascribed to combustion of acetate ions and concurrent formation of  $\text{Co}_3\text{O}_4^3$ . The strongly exothermic peak associated with this step has been attributed to catalytic oxidation of the acetate ions by cobalt oxide formed in the decomposition<sup>4</sup>. The observed total weight loss of *ca.* 2% was considerably lower than the theoretical value of 9.5% (based on the formation of  $\text{Co}(\text{CH}_3\text{CO}_2)_2 \cdot 4\text{H}_2\text{O}$ ).

Decomposition of the Imp-nitrate precursor (Figure 5.1 (b), solid lines) proceeded in two main steps: Adsorbed water and water of crystallisation were lost until *ca.* 150°C. A weakly endothermic weight loss at 179°C corresponded to transformation of the nitrate ions to  $\text{Co}_3\text{O}_4$ <sup>5</sup>. The overall weight loss of *ca.* 7% was lower than the theoretical value of 11.7% (based on the formation of  $\text{Co}(\text{NO}_3)_2 \cdot 6\text{H}_2\text{O}$ ).

The cobalt hydroxycarbonate hydrate utilised in the synthesis of PB-hydroxycarbonate was equivalent to the AtoC precursor from Chapter 4. This precursor, which gave rise to one of the most active catalysts prepared by precipitation, presented a TGA weight loss of *ca.* 25% centred at 250°C (Figure 4.5 (b)). A weight loss of *ca.* 1.7% would therefore be expected upon decomposition of the PB-hydroxycarbonate precursor to  $\text{Co}_3\text{O}_4/\text{SiO}_2$ . The observed weight loss for this sample was only *ca.* 0.5% at 254°C (Figure 5.1 (c), solid lines), which indicated that species other than  $\text{Co}_3\text{O}_4$  were formed in this catalyst.

Overall, the results of the TGA-DTA experiments presented in Figure 5.1 indicated that calcination of the samples at 300°C at a rate of  $10^\circ\text{C min}^{-1}$  with a 2 h isotherm would be sufficient for thermal decomposition of the precursor species.

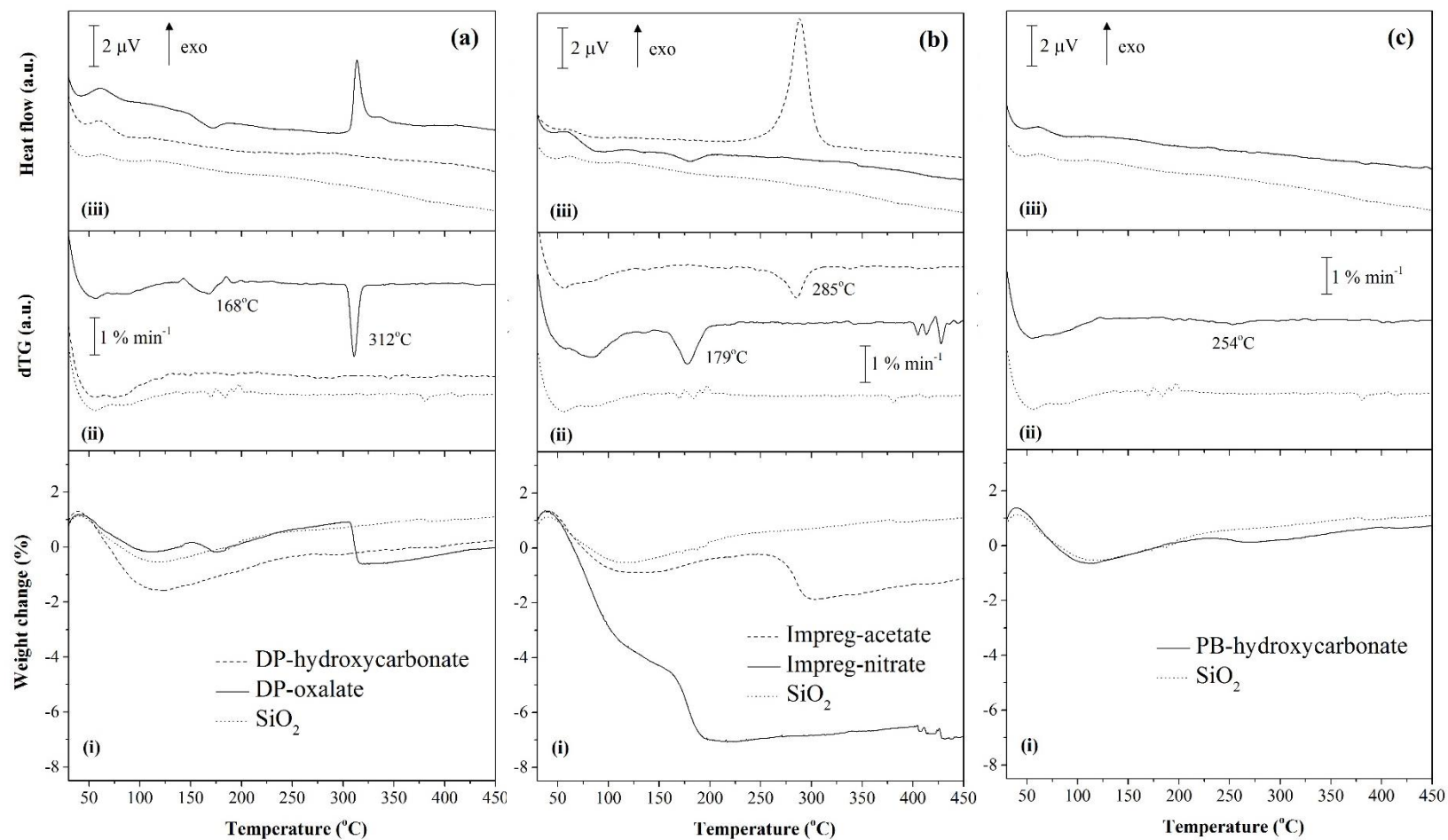


Figure 5.1 – (i) TGA, (ii) DTG and (iii) DTA curves of  
 (a) DP-hydroxycarbonate precursor (dashed line), DP-oxalate precursor (solid line) and SiO<sub>2</sub> (dotted line),  
 (b) Imp-acetate precursor (dashed line), Imp-nitrate precursor (solid line) and SiO<sub>2</sub> (dotted line),  
 (c) PB-hydroxycarbonate precursor (solid line) and SiO<sub>2</sub> (dotted line)

The XRD patterns of  $\text{SiO}_2$  and the catalysts formed upon calcination are shown in Figure 5.2. A broad diffraction peak between  $15$  and  $35^\circ 2\theta$  due to amorphous silica<sup>6</sup> was present in the diffraction pattern of each sample.

For the catalysts prepared by deposition precipitation, peaks relating to the  $\text{Co}_3\text{O}_4$  phase were absent in the pattern of DP-hydroxycarbonate but present for DP-oxalate (Figure 5.2 (b) and (c), respectively)<sup>7</sup>. These observations correlated with the results of TGA experiments, in which no transformation of the hydroxycarbonate was apparent but decomposition of the oxalate was detected (Figure 5.1 (a)). Two very weak, broad bands at  $35$  and  $60^\circ 2\theta$  in the XRD pattern of DP-hydroxycarbonate were assigned to a poorly crystalline cobalt phyllosilicate, which is a cobalt silicate compound consisting of alternative layers of linked tetrahedral  $\text{SiO}_4$  units and linked octahedral  $\text{CoO}_6$  units<sup>8</sup>.

For the catalysts prepared by impregnation, no phase other than  $\text{SiO}_2$  was detected for Imp-acetate but  $\text{Co}_3\text{O}_4$  was present in Imp-nitrate (Figure 5.2 (d) and (e), respectively). Although the TGA of Imp-acetate revealed a weight loss much lower than the theoretical value upon decomposition (Figure 5.1 (b)), it was anticipated that some  $\text{Co}_3\text{O}_4$  would be present in the calcined catalyst. The absence of peaks relating to this phase indicated that the cobalt was well dispersed and could be present as small oxide or silicate crystallites or as an amorphous silicate phase<sup>3, 9</sup>. The presence of  $\text{Co}_3\text{O}_4$  in the Imp-nitrate catalyst correlated with the observed decomposition of cobalt nitrate hydrate during TGA (Figure 5.1 (b)).

$\text{Co}_3\text{O}_4$  was the only additional phase detected in the XRD patterns of both catalysts prepared by powder blending, although the diffraction peaks were less intense for PB-hydroxycarbonate (Figure 5.2 (f)) compared to PB- $\text{Co}_3\text{O}_4$  (Figure 5.2 (g)). The low intensity of the peaks for PB-hydroxycarbonate correlated with the small weight loss observed for this sample during thermal decomposition (Figure 5.1 (c)). Peaks relating to  $\text{Co}_3\text{O}_4$  were also observed in the XRD pattern of  $\text{Co}_3\text{O}_4$ - $\text{SiO}_2$ -mix (Figure 5.2 (h)).

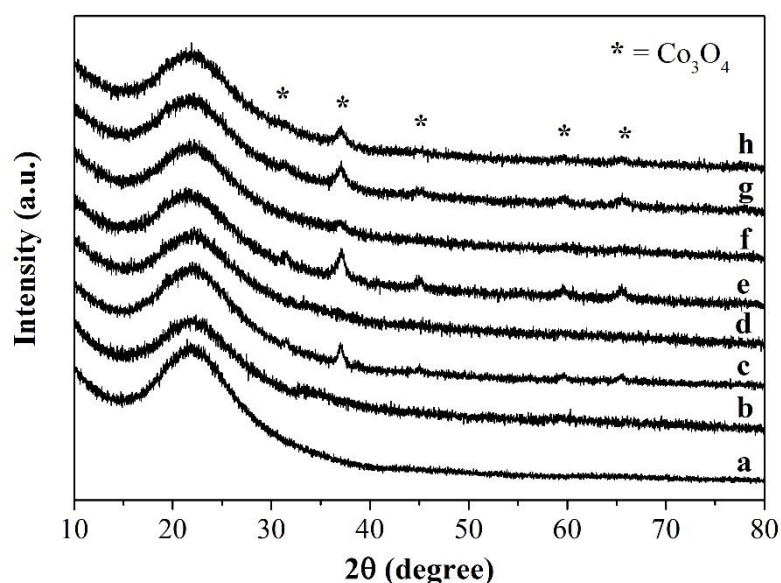


Figure 5.2 – XRD patterns of (a)  $\text{SiO}_2$ , (b) DP-hydroxycarbonate, (c) DP-oxalate, (d) Imp-acetate, (e) Imp-nitrate, (f) PB-hydroxycarbonate, (g) PB- $\text{Co}_3\text{O}_4$  and (h)  $\text{Co}_3\text{O}_4$ - $\text{SiO}_2$ -mix

The distribution of cobalt on the SiO<sub>2</sub> support was investigated using the backscattered detector (BSD) mode of SEM in conjunction with EDX mapping. The micrographs and their associated Co X-ray maps are shown in Figure 5.3. Quantitative EDX analysis was also performed over three larger areas of each catalyst and the averaged cobalt loading values are presented in Table 5.2.

Although TGA and XRD investigations did not reveal the presence of any cobalt-containing phases in DP-hydroxycarbonate (Figures 5.1 (a) and 5.2 (b), respectively), this catalyst was found to have a weight loading of 4.0% Co/SiO<sub>2</sub>. No compositional contrast between cobalt and the support was observed by SEM, but EDX indicated that the cobalt was distributed over the surface of the silica (Figure 5.3 (b)). The cobalt could be present as very small crystallites of oxide or silicate or as amorphous silicate.

The DP-oxalate presented a relatively low loading of 2 wt% Co/SiO<sub>2</sub>, which correlated with the smaller than expected TGA weight loss (Figure 5.1 (a)) and suggested that not all of the cobalt had precipitated from solution. The BSD micrograph indicated that the cobalt was mainly precipitated as unsupported needles (Figure 5.3 (c)). Based on XRD results (Figure 5.2 (c)), and with reference to the bulk OtoA catalyst described in Chapter 4, the needles were assigned as Co<sub>3</sub>O<sub>4</sub>.

A Co/SiO<sub>2</sub> weight loading of 4.3% was observed for the Imp-acetate catalyst, which was higher than expected based on TGA results (Figure 5.1 (b)). SEM did not reveal compositional contrast but cobalt was observed across the surface of the support by X-ray mapping (Figure 5.3 (d)). As discussed for the DP-hydroxycarbonate sample,

this could relate to oxide or silicate phases below the detection limits of XRD and SEM.

A greater than expected Co/SiO<sub>2</sub> weight loading (4.0%) was also observed for Imp-nitrate. However, in contrast to the other samples, a supported cobalt phase – likely the Co<sub>3</sub>O<sub>4</sub> seen by XRD in Figure 5.2 (e) – was observed in the BSD micrograph of this catalyst (Figure 5.3 (e)). EDX mapping revealed the presence of even more cobalt across the SiO<sub>2</sub> surface, which was again attributed to oxides or silicates.

A loading of 3.2 wt% Co/SiO<sub>2</sub> was measured for PB-hydroxycarbonate, which was higher than expected based on the low TGA weight loss and weak XRD peaks (Figures 5.1 (c) and 5.2 (f), respectively), suggesting that phases other than Co<sub>3</sub>O<sub>4</sub> were present in this catalyst. Large particles of a cobalt-containing phase – likely to be Co<sub>3</sub>O<sub>4</sub> – were observed by SEM, but these were not supported on the SiO<sub>2</sub> (Figure 5.3 (f)). Additional cobalt, attributed to oxides or silicates, was seen over the surface of the support in the X-ray map.

The PB-Co<sub>3</sub>O<sub>4</sub> catalyst presented a weight loading of 3.9% Co/SiO<sub>2</sub>. Large discrete particles of a cobalt-containing phase were observed by SEM (Figure 5.3 (g)), which can be assigned as Co<sub>3</sub>O<sub>4</sub> based on the results of XRD analysis (Figure 5.2 (g)). These particles did not appear to be supported. Large unsupported particles of Co<sub>3</sub>O<sub>4</sub> were also observed for the Co<sub>3</sub>O<sub>4</sub>-SiO<sub>2</sub>-mix sample (Figure 5.3 (h)).

The cobalt weight loadings were found to be greater than the desired loading of 3.7% for several of the catalysts. The values were outside the experimental error for EDX

and may have resulted from uneven distribution of cobalt throughout the catalysts or errors during synthesis.

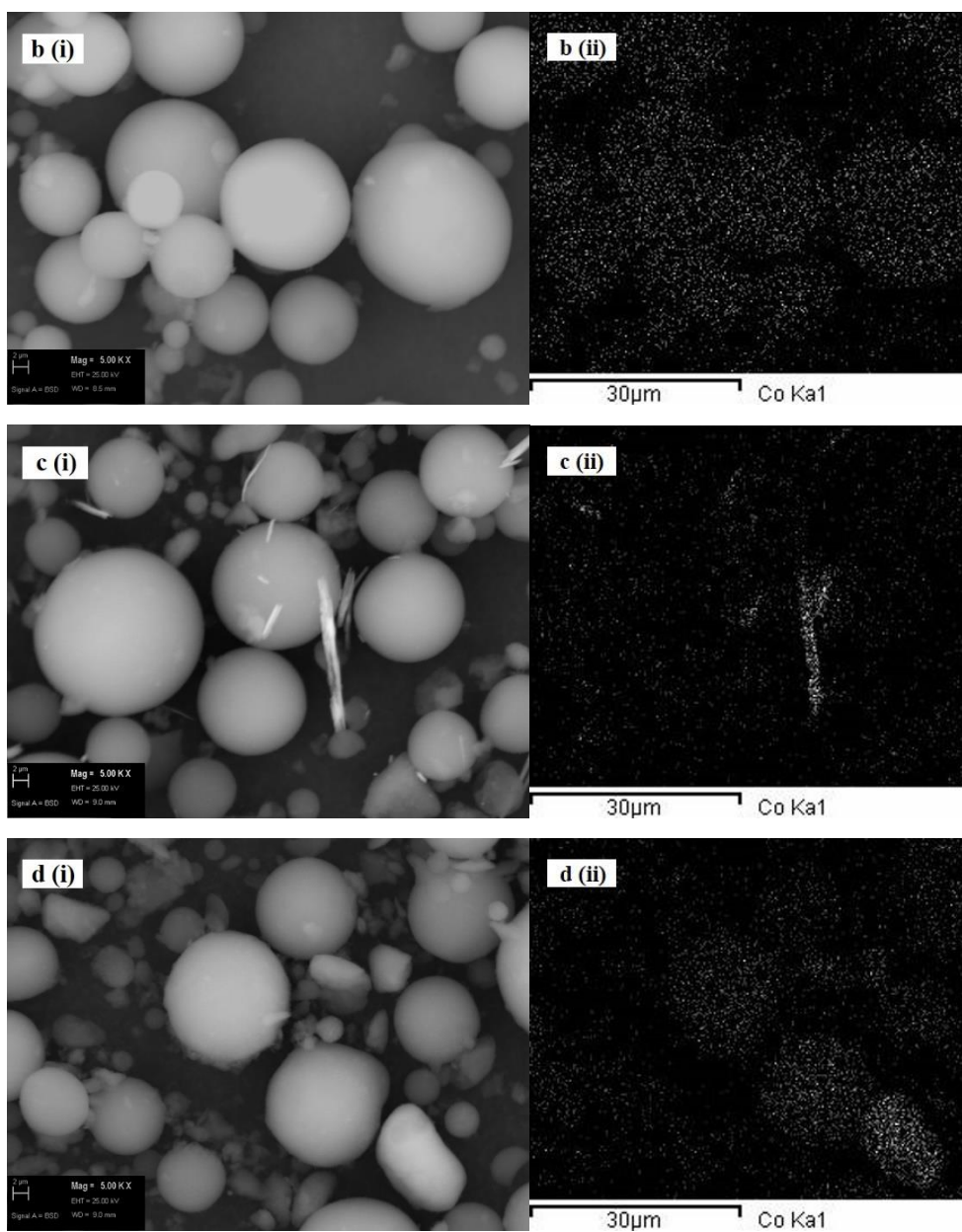


Figure 5.3 – (i) BSD SEM micrographs at 5k x mag and (ii) Co EDX maps of (b) DP-hydroxycarbonate, (c) DP-oxalate, (d) Imp-acetate

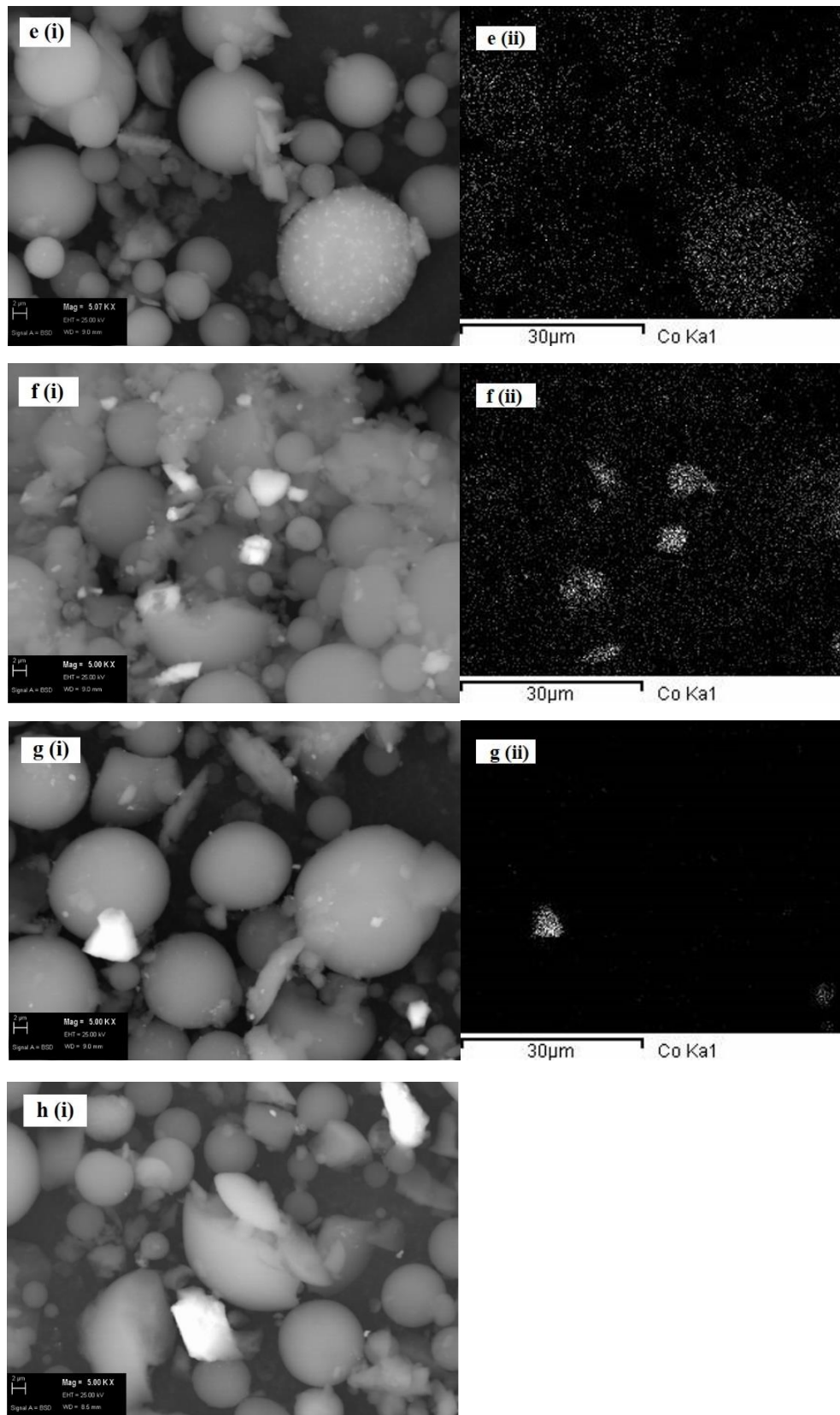


Figure 5.3 – (i) BSD SEM micrographs at 5k x mag and (ii) Co EDX maps of (e) Imp-nitrate, (f) PB-hydroxycarbonate, (g) PB-Co<sub>3</sub>O<sub>4</sub> and (h) Co<sub>3</sub>O<sub>4</sub>-SiO<sub>2</sub>-mix

Table 5.2 – Physicochemical characteristics of catalysts

Sample	Nominal Co loading (wt%)	Measured Co loading (wt%)	Surface area (m <sup>2</sup> g <sup>-1</sup> )
SiO <sub>2</sub>	-	-	223
DP-hydroxycarbonate	3.7	4.0	211
DP-oxalate	3.7	2.1	204
Imp-acetate	3.7	4.3	197
Imp-nitrate	3.7	4.0	210
PB-hydroxycarbonate	3.7	3.2	195
PB-Co <sub>3</sub> O <sub>4</sub>	3.7	3.9	182
Co <sub>3</sub> O <sub>4</sub> -SiO <sub>2</sub> -mix	3.7	not measured	185

The BET specific surface areas of the catalysts are reported in Table 5.2. Fresh SiO<sub>2</sub> presented a high surface area of 223 m<sup>2</sup> g<sup>-1</sup>. Lower surface areas of between 182 and 211 m<sup>2</sup> g<sup>-1</sup> were observed for each of the catalysts. No clear trend was apparent between surface area and cobalt content.

The catalysts were analysed using FT-IR spectroscopy but due to the low cobalt weight loading, only bands relating to SiO<sub>2</sub> could be distinguished (spectra not shown). UV-vis spectroscopy was therefore utilised to investigate the nature of the cobalt species in the catalysts. The spectra are shown in Figure 5.4. A band at 240 nm, which was present in the spectrum of every catalyst, was attributed to oxygen to metal charge transfer<sup>10</sup>. The noise observed in the spectra at 350 nm related to the changeover between the UV and visible light sources. Two broad bands centred at 411 and 700 nm were observed in the spectra of DP-oxalate (Figure 5.4 (c)), Imp-nitrate (Figure 5.4 (d)), PB-hydroxycarbonate (Figure 5.4 (f)), PB-Co<sub>3</sub>O<sub>4</sub> (Figure 5.4 (g)) and Co<sub>3</sub>O<sub>4</sub>-SiO<sub>2</sub>-mix (Figure 5.4 (h)). These bands revealed the presence of Co<sub>3</sub>O<sub>4</sub>, in agreement with the XRD results shown in Figure 5.2: the band at 411 nm was due to *d-d* electronic transitions of octahedrally coordinated Co<sup>3+</sup> ions in Co<sub>3</sub>O<sub>4</sub> whilst the band at 700 nm was due to transitions of tetrahedrally coordinated Co<sup>2+</sup> ions<sup>11</sup>. Also

in accordance with XRD results,  $\text{Co}_3\text{O}_4$  was not detected in the UV-vis spectra of DP-hydroxycarbonate or Imp-acetate (Figure 5.4 (b) and (d), respectively). A band observed for both catalysts at 364 nm was attributed to  $\text{Co}^{3+}$  ions in an octahedral environment<sup>8</sup>. Two further bands characteristic of  $\text{Co}^{2+}$  in an octahedral environment were present in the spectrum of DP-hydroxycarbonate at 533 and 654 nm, which suggested the presence of a cobalt phyllosilicate<sup>8</sup> (as observed by XRD in Figure 5.2 (b)). A triplet of bands at 522, 587 and 654 nm observed in the spectra of Imp-acetate revealed the presence of  $\text{Co}^{2+}$  ions in a tetrahedral environment, indicative of a cobalt silicate species<sup>8</sup>. Silicate species may also have been present in the other catalysts, but the high intensities of the bands due to  $\text{Co}_3\text{O}_4$  would have masked any silicate bands.

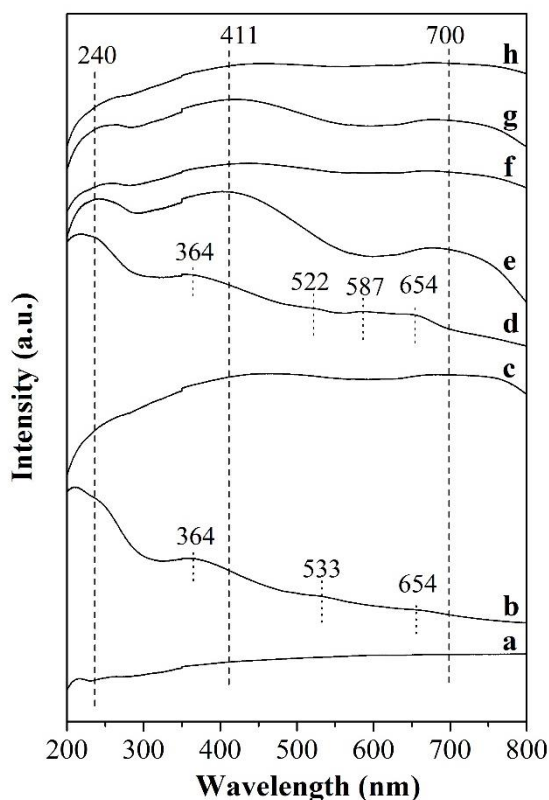


Figure 5.4 – UV-vis spectra of (a)  $\text{SiO}_2$ , (b) DP-hydroxycarbonate, (c) DP-oxalate, (d) Imp-acetate, (e) Imp-nitrate, (f) PB-hydroxycarbonate, (g) PB- $\text{Co}_3\text{O}_4$  and (h)  $\text{Co}_3\text{O}_4$ - $\text{SiO}_2$ -mix

The TPR profiles of the catalysts are presented in Figure 5.5. No reduction peaks were observed for the silica support within the studied temperature range of 30-910°C (Figure 5.5 (a)). As a reminder, in Chapter 3 the reduction of bulk unsupported cobalt oxide was reported to occur at temperatures between 200 and 400°C in two main steps:  $\text{Co}_3\text{O}_4$  was reduced to  $\text{CoO}$ , then  $\text{CoO}$  to metallic  $\text{Co}$ . The presence of multiple peaks for the second step was attributed to the reduction of particles of a range of sizes.

No reduction peaks relating to  $\text{Co}_3\text{O}_4$  were observed for DP-hydroxycarbonate (Figure 5.5 (b)), as expected from XRD and UV-vis results (Figures 5.2 (b) and 5.4 (b), respectively). Reduction of the catalyst began at 730°C and continued beyond the maximum investigated temperature of 910°C. Cobalt phyllosilicates, which were observed in this catalyst by XRD and UV-vis, have previously been reported to undergo reduction at these high temperatures<sup>1</sup>.

The TPR profile of DP-oxalate (Figure 5.5 (c)) was similar to that of bulk  $\text{Co}_3\text{O}_4$ : a peak at 330°C was assigned to the  $\text{Co}_3\text{O}_4$  to  $\text{CoO}$  transformation whilst two subsequent peaks at 380 and 425°C were attributed to reduction to  $\text{Co}^0$ . No high temperature reduction peaks indicative of silicates were observed for this sample, which supported the conclusion drawn from EDX analysis (Table 5.2) that the lower than expected TGA weight loss (Figure 5.1 (a)) was due to incomplete precipitation from solution, rather than formation of silicates.

Imp-acetate displayed a minor reduction peak at 325°C (Figure 5.5 (d)). This revealed the presence of a small amount of  $\text{Co}_3\text{O}_4$  which was below the detection limits of XRD and UV-vis analysis (Figures 5.2 (d) and 5.4 (d), respectively), but was anticipated

based on TGA results (Figure 5.1 (b)). The majority of the sample was reduced at temperatures between 670 and 900°C, which was attributed to the reduction of cobalt silicate species<sup>9</sup> observed by UV-vis analysis.

Two low temperature peaks were observed for Imp-nitrate at 330 and 360°C, which were assigned to the reduction of  $\text{Co}_3\text{O}_4$  and  $\text{CoO}$ , respectively (Figure 5.5 (e)). A series of broad peaks was also observed between temperatures of 400 and 900°C, which indicated the presence of multiple cobalt species interacting with the silica support to different extents<sup>9</sup>. In contrast to the Imp-acetate catalyst, for which reduction of the silicates began at 670°C, it has been suggested that continuous peaks across a broad temperature range are due to silicates formed in-situ during the reduction process by reaction between  $\text{CoO}$  and the support<sup>9</sup>. Nonetheless, the discrepancy for the Imp-nitrate sample between the low weight loss observed by TGA (Figure 5.1 (b)) and the high cobalt weight loading determined by EDX (Table 5.2) suggested that at least some of the silicate species were formed in the reaction solution during the initial impregnation synthesis.

A similar reduction profile to that of Imp-nitrate was observed for PB-hydroxycarbonate (Figure 5.5 (f)). A small, broad peak at 360°C was assigned to the reduction of  $\text{Co}_3\text{O}_4$  and major reduction peaks between 470 and 900°C indicated the presence of cobalt silicates. As for Imp-nitrate, the small TGA weight loss (Figure 5.1 (c)) contrasted against the high cobalt weight loading observed by EDX (Table 5.2) indicated that some silicate species were formed during the initial powder blending synthesis before calcination.

The PB- $\text{Co}_3\text{O}_4$  and  $\text{Co}_3\text{O}_4$ - $\text{SiO}_2$ -mix catalysts displayed similar reduction profiles to each other (Figure 5.5 (g) and (h), respectively) which consisted of a small peak at  $305^\circ\text{C}$  (attributed to the reduction of  $\text{Co}_3\text{O}_4$  to  $\text{CoO}$ ) followed by a more intense asymmetric peak at  $350^\circ\text{C}$  (attributed to the reduction of  $\text{CoO}$  to metallic cobalt). Neither of the catalysts presented high temperature peaks relating to cobalt silicates. The similarity between the two profiles supported the conclusion that the  $\text{Co}_3\text{O}_4$  particles observed in the PB- $\text{Co}_3\text{O}_4$  catalyst by SEM were not supported on the silica.

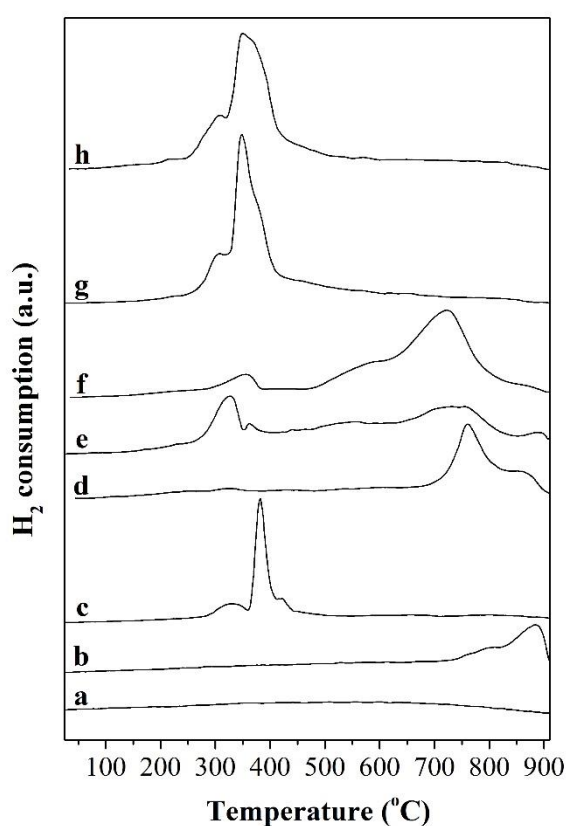


Figure 5.5 – TPR profiles of (a)  $\text{SiO}_2$ , (b) DP-hydroxycarbonate, (c) DP-oxalate, (d) Imp-acetate, (e) Imp-nitrate, (f) PB-hydroxycarbonate, (g) PB- $\text{Co}_3\text{O}_4$  and (h)  $\text{Co}_3\text{O}_4$ - $\text{SiO}_2$ -mix. 90 mg of each sample was analysed.

The activity of the catalysts for the total oxidation of propane is shown in Figure 5.6 and the temperatures required for 10, 50 and 90% conversion are reported in Table 5.3. Comparison of the activity of fresh SiO<sub>2</sub> with conversion due to homogeneous gas phase reactions in a blank reactor tube indicated that the support was not active for propane oxidation as a conversion of *ca.* 4% was observed at 350°C in both cases.

The cobalt containing catalysts could be split into two main groups depending on their activity at a reaction temperature of 350°C – those which achieved less than 50% propane conversion and those which achieved greater than 50% conversion. For the less active group of catalysts, activity increased in the order DP-hydroxycarbonate < Imp-acetate < PB-hydroxycarbonate < DP-oxalate based on the temperatures required for 10% propane conversion, which decreased from 332 to 310 to 297 to 292°C, respectively. For the more active catalysts, lower T<sub>10</sub> temperatures of 260, 255 and 252°C were observed for Imp-nitrate, Co<sub>3</sub>O<sub>4</sub>-SiO<sub>2</sub>-mix and PB-Co<sub>3</sub>O<sub>4</sub>, respectively. The same order of activity was observed for these catalysts at 50% propane conversion: Imp-nitrate (T<sub>50</sub> = 324°C) < Co<sub>3</sub>O<sub>4</sub>-SiO<sub>2</sub>-mix (T<sub>50</sub> = 303°C) < PB-Co<sub>3</sub>O<sub>4</sub> (T<sub>50</sub> = 292°C). The conversion of 90% propane was only observed for the Co<sub>3</sub>O<sub>4</sub>-SiO<sub>2</sub>-mix and PB-Co<sub>3</sub>O<sub>4</sub> catalysts at temperatures of 345 and 342°C, respectively. None of the catalysts achieved 100% propane conversion by 350°C.

The selectivity of the catalysts towards CO<sub>2</sub> is shown in Figure 5.7. Propene was produced over the catalysts at low propane conversions. Selectivity to CO<sub>2</sub> increased with conversion and the catalysts displayed 100% selectivity to CO<sub>2</sub> at propane conversions of *ca.* 30% and above.

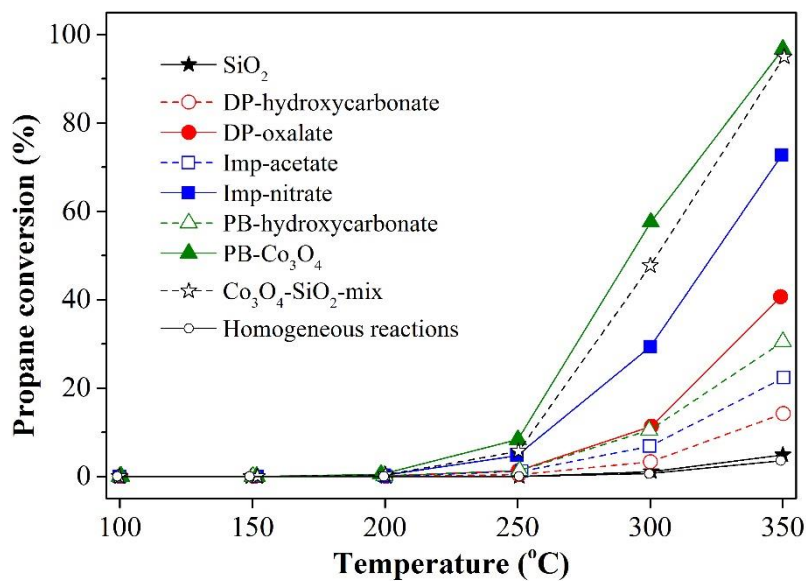
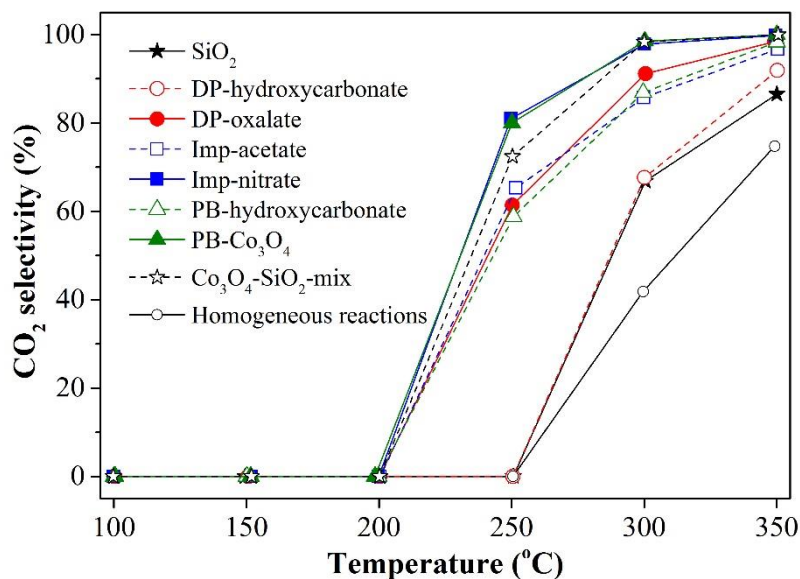
Figure 5.6 – Propane conversion over Co/SiO<sub>2</sub> catalystsFigure 5.7 – CO<sub>2</sub> selectivity over Co/SiO<sub>2</sub> catalysts

Table 5.3 – Catalytic activity

Sample	T <sub>10</sub> (°C)	T <sub>50</sub> (°C)	T <sub>90</sub> (°C)
SiO <sub>2</sub>	>350	>350	>350
DP-hydroxycarbonate	332	>350	>350
DP-oxalate	295	>350	>350
Imp-acetate	310	>350	>350
Imp-nitrate	260	324	>350
PB-hydroxycarbonate	297	>350	>350
PB-CO <sub>3</sub> O <sub>4</sub>	252	292	342
CO <sub>3</sub> O <sub>4</sub> -SiO <sub>2</sub> -mix	255	303	345

The six preparation methods investigated for the synthesis of 5 wt% Co<sub>3</sub>O<sub>4</sub>/SiO<sub>2</sub> gave rise to catalysts with different characteristics and different activities for the total oxidation of propane. The observed differences can be rationalised by considering the processes which occurred between the silica and the cobalt species during each of the syntheses.

Silanol groups (Si-OH) are found on the surface of fumed silica<sup>12</sup> and the extent of protonation or deprotonation of these groups in aqueous solution varies with pH, as shown in Figure 5.8<sup>13</sup>. The point of zero charge (PZC) indicates the pH at which the fraction of positive and negative sites on the silica surface are equal<sup>13</sup>.

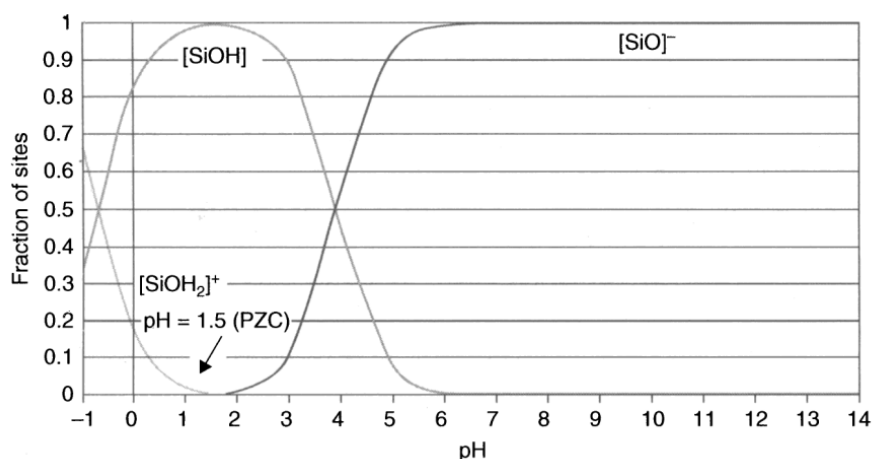


Figure 5.8 – Fraction of positive, negative and neutral sites on a SiO<sub>2</sub> surface immersed in water at various pH values. Reproduced from reference<sup>13</sup>.



have been reported previously for a number of transition metals, including cobalt<sup>8</sup> and nickel<sup>15</sup>. Burattin *et al.*<sup>15</sup> proposed a formation mechanism: Electrostatic interactions between deprotonated silanol groups and the hexaaqua complex ( $[\text{Co}(\text{H}_2\text{O})_6]^{2+}$  in this case) lead to adsorption of the metal complex onto the support surface. Hydroxoqua complexes ( $[\text{Co}(\text{OH})(\text{H}_2\text{O})_5]^+$  or  $[\text{Co}(\text{OH})_2(\text{H}_2\text{O})_4]$ ), which are in equilibrium with the hexaaqua complex, can then react with silanol groups by heterocondensation. Concurrently, silicic acid and cobalt complexes in solution undergo heterocondensation reactions. The cobalt-silica surface species act as nucleation sites for the species formed in solution and continued growth gives rise to supported phyllosilicates. The DP-hydroxycarbonate catalyst displayed the lowest catalytic activity for propane oxidation of all the prepared catalysts in spite of its high cobalt loading, achieving only 14% conversion at 350°C (Figure 5.6). It was concluded that cobalt phyllosilicate was not a desirable phase for the total oxidation of propane, which is likely due to the inability of the phyllosilicate to undergo reduction and partake in the Mars-van Krevelen catalytic cycle (discussed in *Section 3.2.1.2*).

The DP-oxalate catalyst, formed by the addition of oxalic acid to cobalt acetate and silica, contained 2.1% cobalt, *ca.* 50% less than DP-hydroxycarbonate. Nonetheless, DP-oxalate displayed considerably higher activity for propane total oxidation, achieving 40% conversion at 350°C (Figure 5.6). The difference in activity between the two catalysts prepared by deposition precipitation can be attributed to the presence of  $\text{Co}_3\text{O}_4$  in the DP-oxalate sample, as observed by XRD, UV-vis and TPR analysis (Figures 5.2 (c), 5.4 (c) and 5.5 (c), respectively). However, SEM-EDX revealed the cobalt oxide was present as a discrete, unsupported phase (Figure 5.3 (c)). The pH of the reaction solution reduced from pH 6.4 (cobalt acetate/silica) to pH 3.4 upon

addition of oxalic acid. From Figure 5.8 it can be seen that SiOH would be the predominant species present on the surface of the silica at this lower pH value. This would have resulted in limited electrostatic attraction between the silica and either the  $[\text{Co}(\text{H}_2\text{O})_6]^{2+}$  complex or the precipitated cobalt oxalate. Furthermore, local supersaturation of oxalic acid upon its addition to the reaction solution would cause precipitation of bulk oxalate in solution rather than onto the silica surface<sup>16</sup>.

Imp-acetate, prepared by wet impregnation of silica with a cobalt acetate solution, was found to have a high cobalt loading (4.3 wt%) but displayed poor activity for propane oxidation, achieving only 22% conversion at 350°C (Figure 5.6). The low activity of this catalyst can be attributed to the presence of only a small amount of  $\text{Co}_3\text{O}_4$ , with the majority of the cobalt present as cobalt silicates, as observed by TPR (Figure 5.5 (d)). The formation of the silicates is thought to occur during calcination due to the strongly exothermic decomposition of the acetate precursor (Figure 5.1 (b) (iii)) facilitating reaction between cobalt and the silica<sup>3</sup>. Only a small proportion of the precursor was converted to  $\text{Co}_3\text{O}_4$  during calcination. It is likely that some silicate species were also formed in the initial reaction solution, as the TGA weight loss was considerably lower than the theoretical value for decomposition of cobalt acetate (Figure 5.1 (b)). The cobalt acetate-silica suspension presented a pH of 6.8. The majority of the silanol groups on the silica surface would have been deprotonated at this pH (Figure 5.8), leading to electrostatic interactions between the cobalt species and the support. Subsequent heterocondensation reactions between silanol groups and cobalt can lead to cobalt silicate formation<sup>17</sup>. In contrast to the DP-hydroxycarbonate catalyst, formation of cobalt phyllosilicate was not observed for Imp-acetate. Silica would have been dissolved to a lesser extent in the Imp-acetate

reaction solution due to the lower pH (Imp-acetate = pH 6.8; DP-hydroxycarbonate = pH 8.0), so heterocondensation between silicic acid and cobalt complexes in solution would be a minor reaction<sup>15</sup>.

Imp-nitrate, prepared by wet impregnation of silica with a cobalt nitrate solution, was found to have a similarly high cobalt content (4%) to Imp-acetate. TPR analysis (Figure 5.5) showed that the cobalt was present as  $\text{Co}_3\text{O}_4$  and cobalt silicates in both catalysts but the greater proportion of  $\text{Co}_3\text{O}_4$  in Imp-nitrate resulted in considerably higher activity (73% conversion at 350°C, Figure 5.6). The generation of more  $\text{Co}_3\text{O}_4$  in Imp-nitrate could be attributed to several factors: Firstly, as the nitrate suspension presented a lower pH than the acetate suspension (Imp-nitrate = pH 5.2; Imp-acetate = pH 6.8), fewer deprotonated silanol groups would be present on the silica surface (Figure 5.8), resulting in fewer electrostatic interactions and, hence, hindering the formation of silicates. It has been suggested that hexaaquacobalt preferentially bonds to cobalt complexes already bonded to the support rather than to the support itself under these conditions, which facilitates the formation of larger  $\text{Co}_3\text{O}_4$  crystallites<sup>18</sup>. Finally, the endothermic decomposition of cobalt nitrate (Figure 5.1 (b) (iii)) would not facilitate formation of silicate species during calcination in contrast to the exothermic decomposition of cobalt acetate. It is interesting to note that the choice of cobalt salt had very little influence on the products of precipitation in Chapter 4 but led to significant differences for the catalysts formed by impregnation.

PB- $\text{Co}_3\text{O}_4$ , formed by stirring together silica and pre-made  $\text{Co}_3\text{O}_4$  in water, was found to contain 3.9 wt% cobalt. All of the cobalt was present as  $\text{Co}_3\text{O}_4$  according to TPR analysis (Figure 5.5 (g)), which accounted for the high propane oxidation activity

exhibited by this catalyst (96% conversion at 350°C, Figure 5.6). A very similar activity of 95% propane conversion at 350°C was observed for the  $\text{Co}_3\text{O}_4\text{-SiO}_2$ -mix sample, which was simply a physical mixture of the two powders. None of the applied characterisation techniques revealed differences between these two samples, which indicated that  $\text{Co}_3\text{O}_4$  in PB- $\text{Co}_3\text{O}_4$  was present as a discrete phase and was not supported on the silica. Pre-made nanoparticles of  $\text{Fe}_3\text{O}_4$  have been supported on MgO by sonication of the two powders in water<sup>19</sup>. The Lewis basicity of the MgO surface led to interactions between the two compounds<sup>19</sup>. In contrast, the Lewis acidity of the silica surface<sup>16</sup> did not facilitate bonding between  $\text{Co}_3\text{O}_4$  and  $\text{SiO}_2$ . In addition, the relatively low temperature of 300°C utilised during calcination did not cause interdiffusion or solid state reactions between the two oxides – such reactions are observed during the ‘ceramic method’, in which mixed powders are heated at temperatures of 1000°C or higher to form a mixed oxide phase<sup>20</sup>.

The PB-hydroxycarbonate method, which comprised stirring together silica and pre-made cobalt hydroxycarbonate hydrate in water, was investigated as an alternative to the PB- $\text{Co}_3\text{O}_4$  method. It was anticipated that bonds may form between two compounds during calcination to anchor the formed  $\text{Co}_3\text{O}_4$  onto the silica support. Although the catalyst contained 3.2 wt% cobalt, it displayed poor activity for propane oxidation, achieving only 30% conversion at 350°C (Figure 5.6). Based on TPR analysis (Figure 5.5 (f)), the poor activity can be attributed to the formation of only a small amount of  $\text{Co}_3\text{O}_4$ , with a large proportion of the cobalt present as silicate species. The low TGA weight loss (Figure 5.1 (c)) indicated that silicates were formed before calcination. Heterocondensation reactions between silanol groups of silica and

hydroxyl groups of the cobalt hydroxycarbonate hydrate  $(\text{Co}(\text{OH})_x(\text{CO}_3)_{0.5(2-x)} \cdot n\text{H}_2\text{O})$  appeared to occur to a large extent to give cobalt silicates.

### 5.2.3 Conclusions

A variety of methods were investigated for the preparation of 5 wt%  $\text{Co}_3\text{O}_4/\text{SiO}_2$ . The distribution of cobalt in the catalyst samples was dependent upon the synthesis conditions. Deposition precipitation and powder blending were found to be ineffective synthesis methods due to the formation of inactive cobalt silicates or unsupported  $\text{Co}_3\text{O}_4$ . The wet impregnation technique gave rise to supported  $\text{Co}_3\text{O}_4$ , although cobalt silicates were also formed. Impregnation from cobalt nitrate led to a greater proportion of  $\text{Co}_3\text{O}_4$  compared to impregnation from cobalt acetate.

## 5.3 Wet impregnation from cobalt nitrate: investigation of $\text{Co}_3\text{O}_4$ loading

### 5.3.1 Preparation

In *Section 5.2*, the most active catalyst consisting of  $\text{Co}_3\text{O}_4$  supported on silica was prepared by wet impregnation from cobalt nitrate. To study the influence of  $\text{Co}_3\text{O}_4$  weight loading, catalysts consisting of 10, 25 and 50 wt%  $\text{Co}_3\text{O}_4/\text{SiO}_2$  were prepared using the same wet impregnation method described in *Section 5.2.1*. Only the mass of cobalt nitrate was altered and these values are reported in Table 5.4 along with the sample nomenclature. The cobalt nitrate was dissolved in 50 mL of water and impregnated onto 1 g of  $\text{SiO}_2$  in each experiment. The precursors were calcined for 2 h at 300°C with a heating rate of 10°C min<sup>-1</sup> in open air. A bulk  $\text{Co}_3\text{O}_4$  sample prepared in the same way, but in the absence of silica, was termed Imp-nitrate-100. Throughout this section these samples are compared to Imp-nitrate from *Section 5.2*, which was prepared with a nominal cobalt oxide loading of 5 wt%.

Table 5.4 – Sample nomenclature

Sample	Nominal Co <sub>3</sub> O <sub>4</sub> weight loading (%)	Cobalt nitrate mass (g)
Imp-nitrate (5)	5	0.192
Imp-nitrate-10	10	0.402
Imp-nitrate-25	25	1.205
Imp-nitrate-50	50	3.623
Imp-nitrate-100	100	8.926

### 5.3.2 Results and Discussion

The TGA-DTA curves of the precursors heated in an air atmosphere at 10°C min<sup>-1</sup> are shown in Figure 5.10. Based on the conversion of Co(NO<sub>3</sub>)<sub>2</sub>·6H<sub>2</sub>O to Co<sub>3</sub>O<sub>4</sub>, the observed weight loss for every precursor was lower than the theoretical weight loss: Imp-nitrate (5) displayed a 7% loss compared to the expected 12% a weight; Imp-nitrate-10 displayed a 5% loss compared to the expected 21%; Imp-nitrate-25 displayed a 25% loss compared to the expected 40%; Imp-nitrate-50 displayed a 35% loss compared to the expected 57%; and Imp-nitrate-100 displayed a 63% loss compared to the expected 72%. These results suggested either that the cobalt nitrate was present in a less hydrated state than the assumed hexahydrate, that not all of the cobalt in solution had impregnated onto the support or that silicates (which did not undergo thermal decomposition) had formed on the surface of the silica. Decomposition was endothermic in all cases, as expected for the formation of Co<sub>3</sub>O<sub>4</sub> from cobalt nitrate<sup>5</sup>. All of the precursors decomposed at temperatures below 300°C, which indicated that calcination at 300°C would be sufficient to form the active catalysts.

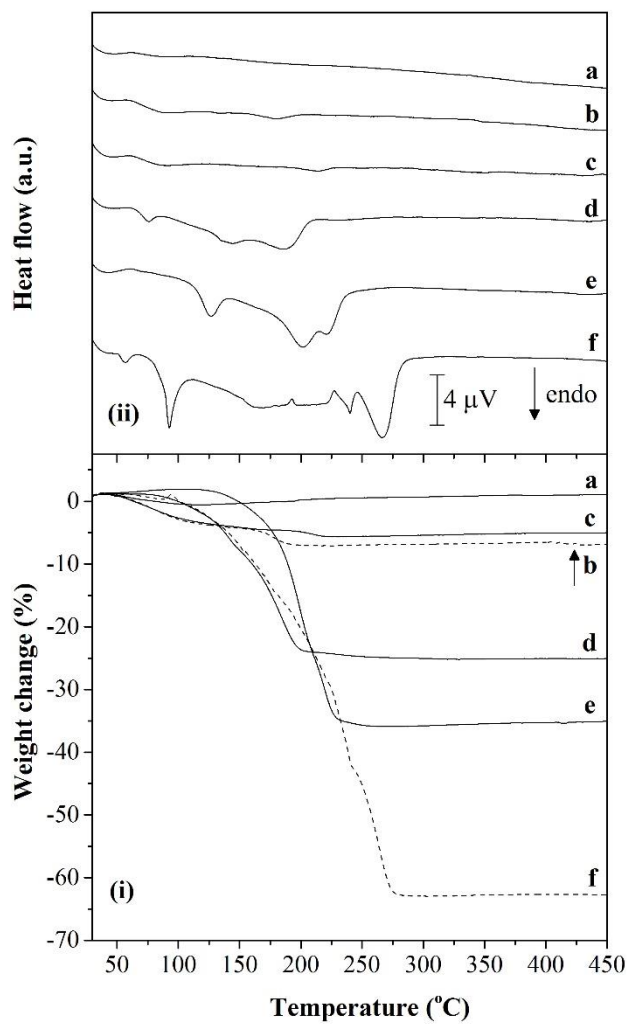


Figure 5.10 – (i) TGA and (ii) DTA curves of (a) SiO<sub>2</sub>, (b) Imp-nitrate (5), (c) Imp-nitrate-10, (d) Imp-nitrate-25, (e) Imp-nitrate-50 and (f) Imp-nitrate-100

The XRD patterns of the calcined samples are presented in Figure 5.11.  $\text{Co}_3\text{O}_4$  was the only cobalt containing phase observed for each of the catalysts. The diffraction peaks became less broad and more intense with increased cobalt oxide weight loading, which indicated that larger crystallites were produced at higher loadings. The average crystallite sizes are reported in Table 5.5. Weight loadings of 5, 10, 25 and 50 wt% gave rise to average crystallite sizes of 11, 15, 20 and 30 nm, respectively. The unsupported catalyst (Imp-nitrate-100) displayed a much greater crystallite size of 147 nm. The intensity of the peak between  $15$  and  $35^\circ 2\theta$  due to silica reduced as the cobalt oxide weight loading increased.

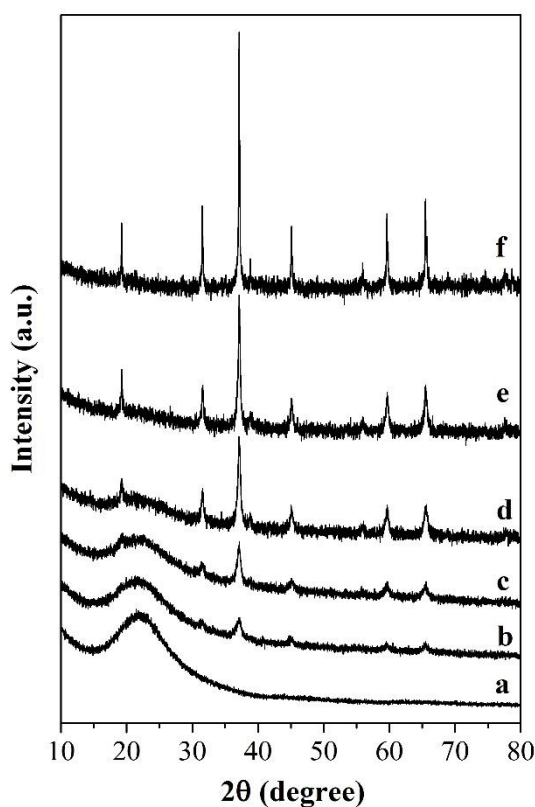


Figure 5.11 – XRD patterns of (a)  $\text{SiO}_2$ , (b) Imp-nitrate (5), (c) Imp-nitrate-10, (d) Imp-nitrate-25, (e) Imp-nitrate-50 and (f) Imp-nitrate-100

Table 5.5 – Physicochemical characteristics of catalysts

Sample	Co <sub>3</sub> O <sub>4</sub> crystallite size (nm)	Nominal Co loading (wt%)	Measured Co loading (wt%)	Surface area (m <sup>2</sup> g <sup>-1</sup> )
SiO <sub>2</sub>	-	-	-	223
Imp-nitrate (5)	11	3.7	4.0	210
Imp-nitrate-10	15	7.5	7.9	202
Imp-nitrate-25	20	19.6	18.0	166
Imp-nitrate-50	30	42.3	34.5	126
Imp-nitrate-100	147	-	-	43

Figure 5.12 shows the BSD SEM micrographs and Co and Si X-ray maps of the catalysts. Particles of a supported cobalt phase were observed in the BSD micrographs of Imp-nitrate (5), Imp-nitrate-10 and Imp-nitrate-50 but EDX mapping revealed the presence of cobalt across the silica surface of all of the supported catalysts. The brightness of the Co X-ray maps increased with nominal cobalt loading, indicating that more cobalt had been deposited on the silica as desired. The results of quantitative EDX analysis are shown in Table 5.5. The measured cobalt loading increased from 4.0 wt% for Imp-nitrate (5) to 42.3 wt% for Imp-nitrate-50. A slightly greater than expected cobalt loading was observed for Imp-nitrate (5) and Imp-nitrate-10, which suggested the cobalt was not evenly distributed throughout the sample. In addition, lower cobalt loadings were expected for these samples based on TGA analysis (Figure 5.10 (b) and (c)), indicating that some of the cobalt was present as silicates. For the catalysts with higher cobalt loadings (Imp-nitrate-25 and Imp-nitrate-50), the measured cobalt loading was lower than the nominal loading, in agreement with TGA results (Figure 5.10 (d) and (e)). This could again be attributed to uneven cobalt distribution or may indicate that total adsorption of cobalt from solution onto the support was not achieved for the samples with higher nominal loadings.

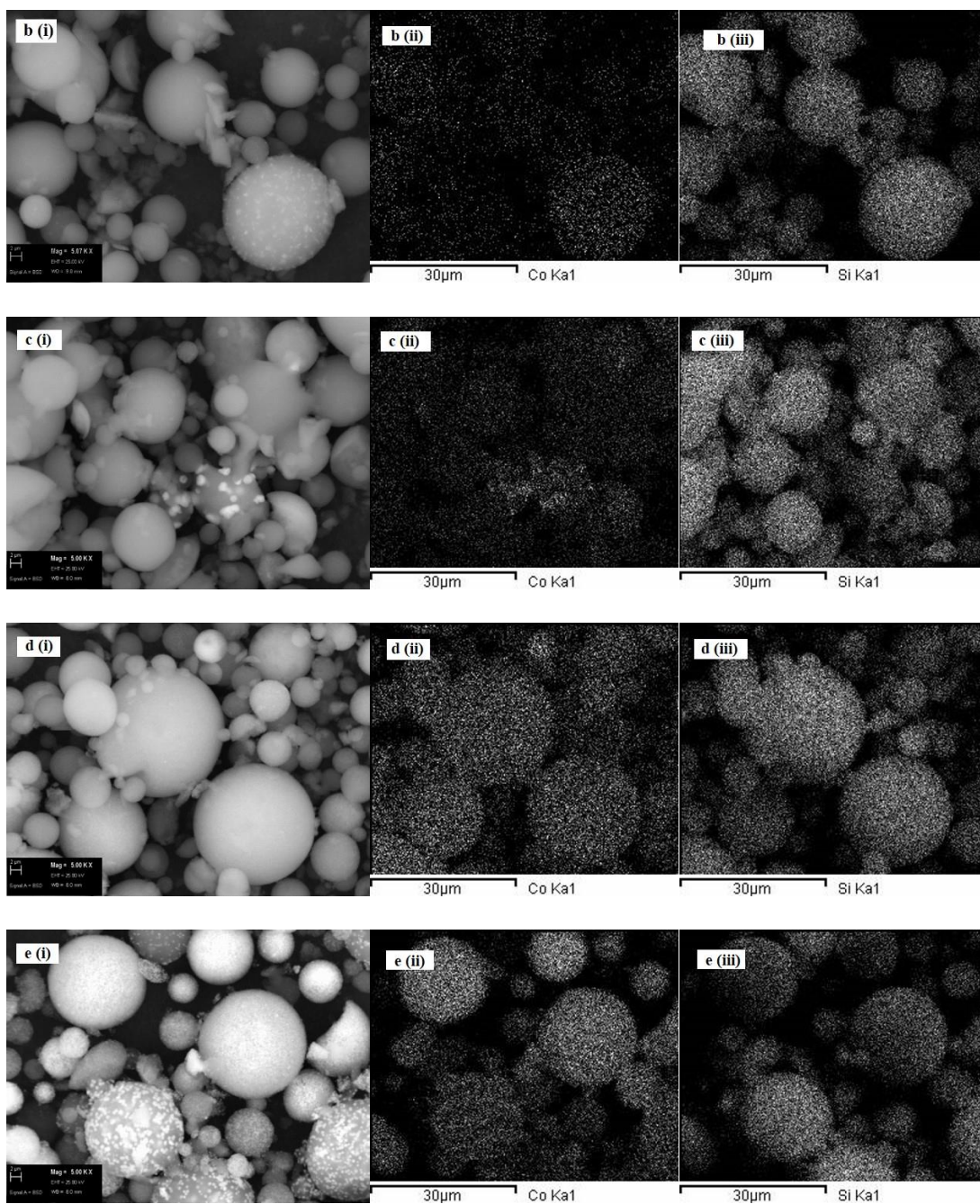


Figure 5.12 – (i) BSD SEM micrographs at 5k x mag, (ii) Co EDX maps and (iii) Si EDX maps of (b) Imp-nitrate (5), (c) Imp-nitrate-10, (d) Imp-nitrate-25 and (e) Imp-nitrate-50

The surface areas of the catalysts are reported in Table 5.5. Every catalyst displayed a lower surface area than the silica support and surface area decreased as cobalt loading increased, reducing from  $210 \text{ m}^2 \text{ g}^{-1}$  for Imp-nitrate (5) to  $126 \text{ m}^2 \text{ g}^{-1}$  for Imp-nitrate-50. The lowest surface area was observed for unsupported Imp-nitrate-100.

The UV-vis spectra of the catalysts are shown in Figure 5.13. Each of the catalysts displayed an oxygen to metal charge transfer band at 240 nm and two broad bands at *ca.* 400 and 700 nm indicative of  $\text{Co}_3\text{O}_4$ , as discussed in Section 5.2.

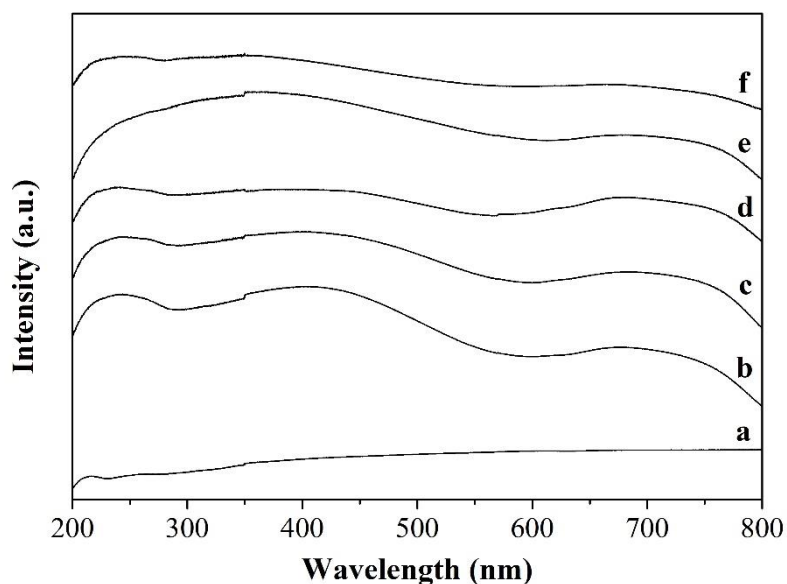


Figure 5.13 – UV-vis spectra of  
(a)  $\text{SiO}_2$ , (b) Imp-nitrate (5), (c) Imp-nitrate-10, (d) Imp-nitrate-25,  
(e) Imp-nitrate-50 and (f) Imp-nitrate-100

The TPR profiles of the catalysts are presented in Figure 5.14. The mass of each catalyst analysed is reported in the figure caption; larger masses were utilised for the samples with lower cobalt weight loadings to ensure the reduction processes were detected by the TCD, but the maximum mass was limited by the capacity of the TPR U-tube. As described in *Section 5.2*, reduction of Imp-nitrate (5) revealed the presence of  $\text{Co}_3\text{O}_4$  and cobalt silicates (Figure 5.14 (b)). For Imp-nitrate-10 (Figure 5.14 (c)), the peak at *ca.* 300°C was assigned to the reduction of  $\text{Co}_3\text{O}_4$  to CoO. A broad peak ranging from 340 to 700°C was attributed to the overlapping reduction of CoO and cobalt silicates. Whilst some silicates may have formed in-situ during the TPR experiment, the very low TGA weight loss for Imp-nitrate-10 (Figure 5.10 (b)) indicated that silicates had already formed in the initial reaction solution. Complete reduction of the silicates at lower temperatures for this catalyst compared to Imp-nitrate (5) suggested that the cobalt interacted less strongly with the silica support for the catalyst with the higher loading<sup>9</sup>. The catalysts with 25 and 50% nominal  $\text{Co}_3\text{O}_4$  weight loadings (Figure 5.14 (d) and (e), respectively) displayed two main peaks at low temperatures (between 220 and 450°C) which were attributed to the reduction of  $\text{Co}_3\text{O}_4$  and CoO. Peaks corresponding to cobalt silicates were not observed for these samples, again indicating that interaction between cobalt species and the support decreased with increasing loading. The profile of unsupported Imp-nitrate-100 (Figure 5.14 (f)) corresponded to the two-step reduction of  $\text{Co}_3\text{O}_4$  to metallic cobalt previously observed for bulk catalysts in Chapter 3.

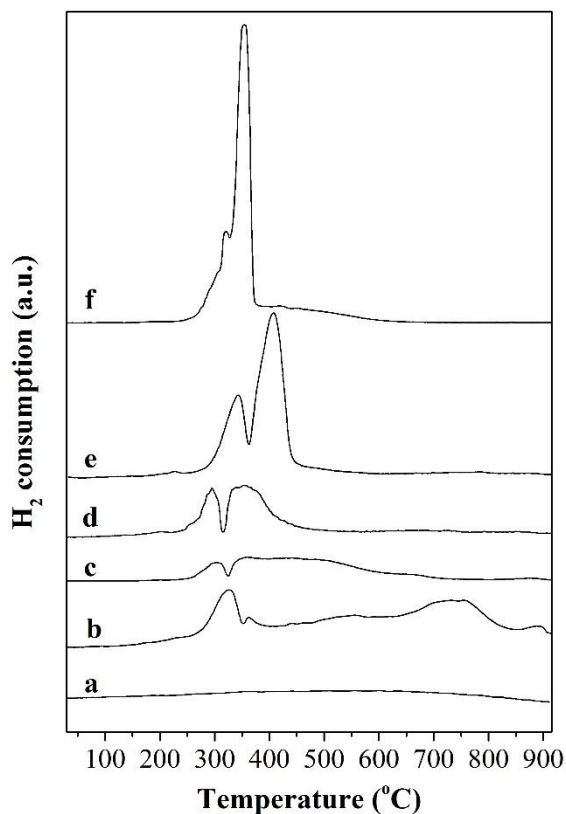


Figure 5.14 – TPR profiles of (a) SiO<sub>2</sub> (90 mg), (b) Imp-nitrate (5) (90 mg), (c) Imp-nitrate-10 (45 mg), (d) Imp-nitrate-25 (30 mg), (e) Imp-nitrate-50 (30 mg) and (f) Imp-nitrate-100 (15 mg)

The propane oxidation activity of the catalysts is shown in Figure 5.15. Comparison of the temperatures required for 10, 50 and 90% conversion (reported in Table 5.6) revealed that activity increased with increased weight loading. All of the catalysts attained 50% propane conversion by 350°C but 100% conversion at this temperature was achieved only for the catalysts with weight loadings of 25% or greater. Imp-nitrate-100 was found to be more active than any of the supported catalysts. The activity of the catalysts prepared by the wet impregnation method was compared to that of AtoC, the most active precipitated catalyst from Chapter 4. AtoC was found to be more active than the wet impregnation catalysts at all temperatures: the activity of the catalysts based on the  $T_{10}$ ,  $T_{50}$  and  $T_{90}$  temperatures increased in the order

Imp-nitrate (5) < Imp-nitrate-10 < Imp-nitrate-25 < Imp-nitrate- 50 < Imp-nitrate-100  
< AtoC.

The selectivity of the catalysts towards CO<sub>2</sub> is shown in Figure 5.16. Propene was produced over the catalysts at low propane conversions, but CO<sub>2</sub> was the predominant reaction product following catalyst light off.

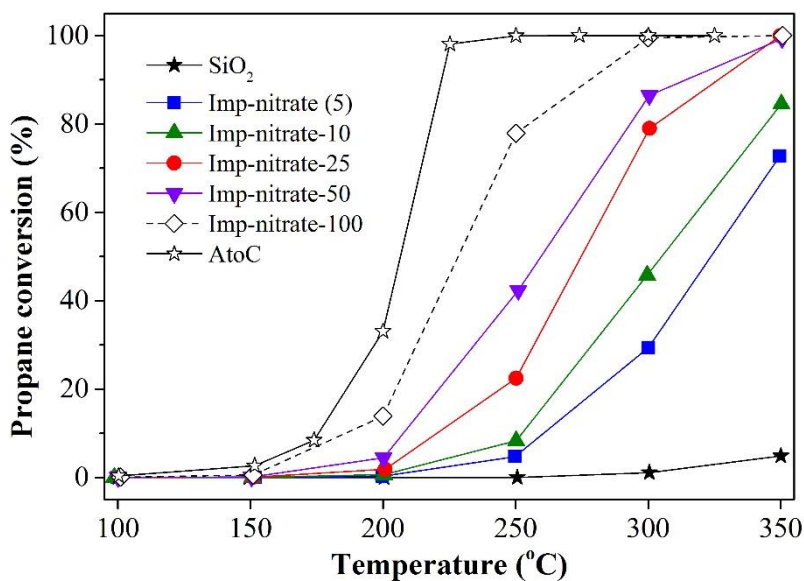


Figure 5.15 – Propane conversion over Co<sub>3</sub>O<sub>4</sub>/SiO<sub>2</sub> catalysts

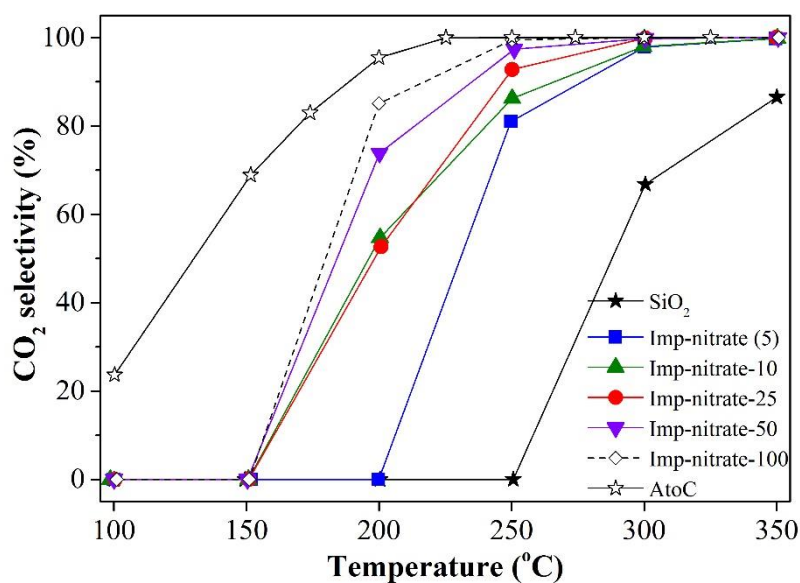


Figure 5.16 – CO<sub>2</sub> selectivity over Co<sub>3</sub>O<sub>4</sub>/SiO<sub>2</sub> catalysts

Table 5.6 – Catalytic activity

Sample	T <sub>10</sub> (°C)	T <sub>50</sub> (°C)	T <sub>90</sub> (°C)
SiO <sub>2</sub>	>350	>350	>350
Imp-nitrate (5)	260	324	>350
Imp-nitrate-10	252	306	>350
Imp-nitrate-25	220	274	328
Imp-nitrate-50	208	260	315
Imp-nitrate-100	186	228	279
AtoC	175	199	221

Wet impregnation of silica with cobalt nitrate gave rise to supported cobalt catalysts at all loading levels investigated in this work, as evidenced by EDX (Figure 5.12). XRD and UV-vis spectroscopy (Figures 5.11 and 5.13, respectively) showed that Co<sub>3</sub>O<sub>4</sub> was present in each of the catalysts. For catalysts with loadings below 25 wt% Co<sub>3</sub>O<sub>4</sub>, cobalt silicates were also detected by TPR analysis (Figure 5.14). The activity of the catalysts was found to increase with increased cobalt weight loading (Figure 5.15).

The only variable altered in the preparation of the wet impregnation series of catalysts was the mass of cobalt nitrate. With increased mass, the concentration of the cobalt nitrate solution increased and the pH values of the cobalt nitrate-silica suspensions become more acidic as catalysts with higher nominal Co<sub>3</sub>O<sub>4</sub> weight loadings were synthesised (exact values not measured). As discussed in *Section 5.2* when comparing the preparation of Imp-acetate and Imp-nitrate, fewer deprotonated silanol groups would be present on the silica surface at lower pH values (Figure 5.8). This would lead to fewer electrostatic interactions between the silica surface and dissolved cobalt species and hinder the formation of cobalt silicates. In addition, preferential bonding

of hexaaquacobalt to pre-bonded cobalt complexes rather than to the support itself under these conditions would facilitate the formation of larger  $\text{Co}_3\text{O}_4$  crystallites<sup>18</sup>.

The greater activity of the catalysts with higher cobalt loadings can therefore be attributed to both the presence of more cobalt and the availability of a greater proportion of the cobalt to partake in the total oxidation reaction as  $\text{Co}_3\text{O}_4$ . The difference in the correlation between crystallite size and total oxidation activity for bulk and supported  $\text{Co}_3\text{O}_4$  catalysts has previously been highlighted for alumina-supported cobalt oxide: activity increases with decreasing crystallite size for bulk catalysts, but decreasing activity with decreasing crystallite size is observed for supported catalysts<sup>21</sup>. In the case of silica-supported  $\text{Co}_3\text{O}_4$  prepared by wet impregnation, cobalt silicates which do not contribute to catalytic activity are more likely to be present in catalysts which contain small  $\text{Co}_3\text{O}_4$  crystallites.

Although wet impregnation was found to be the most suitable method for preparing silica-supported cobalt oxide catalysts in *Section 5.2*, comparison of the activity of unsupported Imp-nitrate-100 with AtoC, one of the most active precipitated bulk catalysts from Chapter 4, demonstrated that precipitation was a superior method for the synthesis of bulk catalysts (Figure 5.15). The higher activity of AtoC can be attributed to the higher surface area and smaller crystallite size of this catalyst compared to Imp-nitrate-100 ( $127 \text{ m}^2 \text{ g}^{-1}$  and 9 nm, compared to  $43 \text{ m}^2 \text{ g}^{-1}$  and 147 nm).

The stability of Imp-nitrate-25 with time-on-line was investigated at a temperature of  $315^\circ\text{C}$  and the results are shown in Figure 5.17. A steady decrease in propane

conversion from *ca.* 70% to *ca.* 60% was observed for the catalyst over the 44 h test but selectivity to CO<sub>2</sub> remained high at greater than 98%. Sintering of the Co<sub>3</sub>O<sub>4</sub> particles or formation of cobalt silicates may account for the decreased activity; characterisation of the used catalyst may reveal changes in the catalyst structure. It should be noted that this time-on-line experiment was performed at a temperature 100°C greater than the time-on-line experiments performed for the bulk Co<sub>3</sub>O<sub>4</sub> catalysts in Chapters 3 and 4.

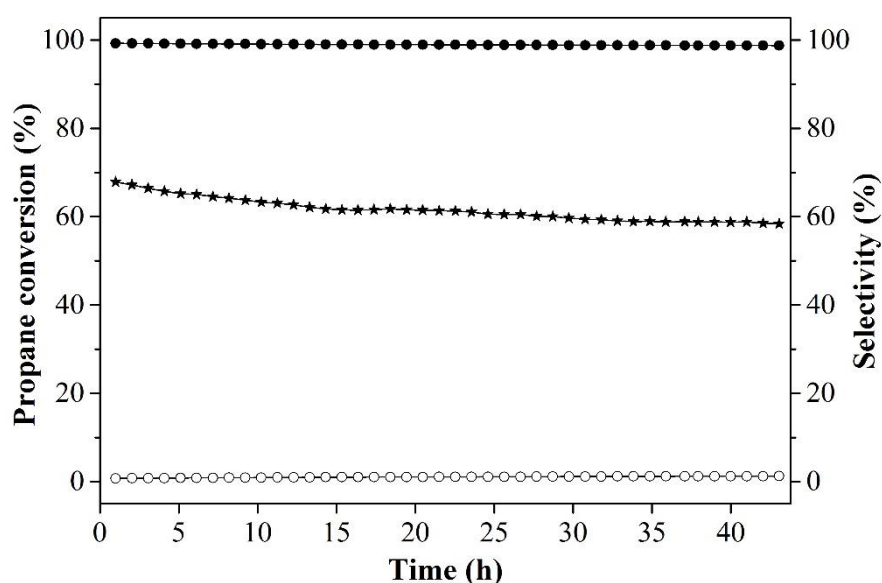


Figure 5.17 – Propane oxidation over Imp-nitrate-25 with time-on-line at 315 °C. Star = propane conversion, filled circle = selectivity to CO<sub>2</sub>, open circle = selectivity to propene.

### 5.3.3 Conclusions

Co<sub>3</sub>O<sub>4</sub>/SiO<sub>2</sub> catalysts with different weight loadings were prepared by wet impregnation of silica with cobalt nitrate. At low weight loadings both cobalt silicates and Co<sub>3</sub>O<sub>4</sub> were formed, but the proportion of silicates reduced as loading increased and could not be detected at higher loadings, which was attributed to a reduction in interaction between the cobalt species and the silica surface. Catalytic activity for the total oxidation of propane increased with weight loading.

## 5.4 Chapter conclusions

The preparation of silica-supported cobalt catalysts has been studied. For the investigated methods of deposition precipitation, wet impregnation and powder blending, the nature of cobalt phase formed was found to depend on the interactions taking place between the silica and the cobalt species. The formation of silicate phases resulted in reduced catalytic activity. Wet impregnation from cobalt nitrate was determined to be the most successful method for producing supported  $\text{Co}_3\text{O}_4$  catalysts, and activity increased with increased cobalt loading. In contrast to the bulk  $\text{Co}_3\text{O}_4$  catalysts prepared in Chapters 3 and 4, the most active supported catalysts exhibited the largest crystallite sizes.

## 5.5 References

1. A. Barbier, A. Hanif, J. A. Dalmon and G. A. Martin, *Appl. Catal. A-Gen.*, 1998, **168**, 333-343.
2. M. A. Gabal, A. A. El-Bellihi and S. S. Ata-Allah, *Mater. Chem. Phys.*, 2003, **81**, 84-92.
3. J.-S. Girardon, A. S. Lermontov, L. Gengembre, P. A. Chernavskii, A. Griboval-Constant and A. Y. Khodakov, *Journal of Catalysis*, 2005, **230**, 339-352.
4. L. Poul, N. Jouini and F. Fievet, *Chem. Mat.*, 2000, **12**, 3123-3132.
5. S. A. A. Mansour, *Mater. Chem. Phys.*, 1994, **36**, 317-323.
6. G. A. Santos, C. M. B. Santos, S. W. da Silva, E. A. Urquieta-Gonzalez and P. C. Sartoratto, *Colloid Surf. A-Physicochem. Eng. Asp.*, 2012, **395**, 217-224.
7. P. Dutta, M. S. Seehra, S. Thota and J. Kumar, *J. Phys.-Condes. Matter*, 2008, **20**, 8.
8. R. Trujillano, J.-F. Lambert and C. Louis, *The Journal of Physical Chemistry C*, 2008, **112**, 18551-18558.
9. A. Martinez, C. Lopez, F. Marquez and I. Diaz, *Journal of Catalysis*, 2003, **220**, 486-499.
10. A. V. Boix, S. G. Aspromonte and E. E. Miró, *Applied Catalysis A: General*, 2008, **341**, 26-34.
11. N. Osakoo, R. Henkel, S. Loiha, F. Roessner and J. Wittayakun, *Applied Catalysis A: General*, 2013, **464-465**, 269-280.
12. C. H. C. Liu and G. E. Maciel, *Journal of the American Chemical Society*, 1996, **118**, 5103-5119.
13. K. A. Reinhardt and R. F. Reidy, *Handbook for Cleaning for Semiconductor Manufacturing: Fundamentals and Applications*, Wiley, 2011.
14. J. P. Brunelle, *Pure Appl. Chem.*, 1978, **50**, 1211-1229.
15. P. Burattin, M. Che and C. Louis, *J. Phys. Chem. B*, 1998, **102**, 2722-2732.

16. *Handbook of Heterogeneous Catalysis*, Wiley-VCH, Weinheim, 2008.
17. E. vanSteen, G. S. Sewell, R. A. Makhothe, C. Micklethwaite, H. Manstein, M. deLange and C. T. Oconnor, *Journal of Catalysis*, 1996, **162**, 220-229.
18. T. Tsoncheva, A. Gallo, N. Scotti, M. Dimitrov, R. Delaigle, E. M. Gaigneaux, D. Kovacheva, V. Dal Santo and N. Ravasio, *Applied Catalysis A: General*, 2012, **417–418**, 209-219.
19. W. W. Liu, A. Aziz, S. P. Chai, A. R. Mohamed and C. T. Tye, *New Carbon Mater.*, 2011, **26**, 255-261.
20. J. A. Schwarz, C. Contescu and A. Contescu, *Chem. Rev.*, 1995, **95**, 477-510.
21. B. Solsona, T. E. Davies, T. Garcia, I. Vazquez, A. Dejoz and S. H. Taylor, *Appl. Catal. B-Environ.*, 2008, **84**, 176-184.

# Chapter 6

## Conclusions and future work

### 6.1 Conclusions

A detailed study of the synthesis of  $\text{Co}_3\text{O}_4$  catalysts for propane total oxidation was performed. Variables in the mechanochemical synthesis and precipitation of  $\text{Co}_3\text{O}_4$  were investigated and the characteristics of the prepared precursors and catalysts were linked to the activity of the catalysts in the oxidation reaction.

For the cobalt hydroxycarbonate hydrate precursor prepared mechanochemically from cobalt nitrate and ammonium hydrogen carbonate, a longer duration of grinding, a lower calcination temperature and calcination in a non-flowing air atmosphere were found to give to the most active  $\text{Co}_3\text{O}_4$  catalysts. The cobalt hydroxycarbonate hydrate precursor was successfully synthesised by reaction of cobalt nitrate with alternative bases. The total oxidation of propane over  $\text{Co}_3\text{O}_4$  catalysts derived from mechanochemically synthesised cobalt oxalate was reported for the first time. Reaction of cobalt acetate and oxalic acid led to catalysts with comparable activity to that of the hydroxycarbonate hydrate-derived catalysts. It was found that heating rate during calcination had little influence on the catalysts.

For the precursors prepared by precipitation, cobalt hydroxycarbonate hydrate was found to give more active  $\text{Co}_3\text{O}_4$  catalysts than cobalt oxalate. Further investigation revealed that precipitation of the cobalt hydroxycarbonate hydrate precursor was very

robust, with molar ratio of reactants, solution concentrations and identity of the carbonate counter ion having little effect on the products. Further characterisation would be required to account for the differences observed between precipitates aged for different times.

Small  $\text{Co}_3\text{O}_4$  crystallites, high surface areas, weak  $\text{Co}^{3+}$ -O bonds, and the absence of contaminants were found to be required for high propane oxidation activity for bulk  $\text{Co}_3\text{O}_4$  catalysts. The catalysts displayed stable activity with time on line at  $215^\circ\text{C}$  for over 40 h.

A study of silica-supported  $\text{Co}_3\text{O}_4$  catalysts was also performed. Methods of precipitation which gave active bulk catalysts were not successfully transferred to give  $\text{Co}_3\text{O}_4/\text{SiO}_2$  by deposition precipitation due to the formation of cobalt silicates or unsupported  $\text{Co}_3\text{O}_4$ . Likewise, powder blending of pre-formed cobalt hydroxycarbonate hydrate or  $\text{Co}_3\text{O}_4$  with silica gave rise to silicates or unsupported oxide particles. Wet impregnation from cobalt acetate gave primarily cobalt silicates, but supported  $\text{Co}_3\text{O}_4/\text{SiO}_2$  with a lower proportion of silicates was formed by wet impregnation from cobalt nitrate. With increased cobalt weight loading by nitrate wet impregnation, activity was found to increase and less silicates were formed.

In contrast to bulk  $\text{Co}_3\text{O}_4$  catalysts, the most active supported catalysts exhibited the largest crystallite sizes. This discrepancy may be due to silica acting as a diluent in the supported catalysts with low weight loadings and small crystallite sizes; if two supported catalysts of a given weight loading were prepared with different  $\text{Co}_3\text{O}_4$

crystallite sizes, it is postulated that higher activity would be achieved for the catalyst with smaller crystallites.

## 6.2 Future work

- For the preparation of bulk  $\text{Co}_3\text{O}_4$ , the addition of a chelating agent, which is removed either by decomposition during calcination or by washing after calcination, could be investigated to minimise crystallite growth or particle agglomeration and maximise catalyst surface area. This could be investigated for both the cobalt hydroxycarbonate hydrate and cobalt oxalate hydrate precursors prepared by mechanochemistry or precipitation. Addition of sucrose during precipitation of cobalt hydroxide has previously been shown to reduce  $\text{Co}_3\text{O}_4$  crystallite size from 54 nm to 19 nm<sup>1</sup>.
- Cobalt hydroxycarbonate hydrate was found to give rise to more active  $\text{Co}_3\text{O}_4$  catalysts than cobalt oxalate hydrate. The mechanochemical synthesis or precipitation of alternative precursors, such as cobalt hydroxide, may yield catalysts with even greater activity.
- Wet impregnation from cobalt nitrate was found to be the most effective method of supporting  $\text{Co}_3\text{O}_4$  on silica, but cobalt silicates were also formed. Reducing the pH of the cobalt nitrate impregnation solution by the addition of nitric acid may give rise to a lower number of deprotonated silanol groups on the silica surface, impeding the formation of silicates and giving rise to larger  $\text{Co}_3\text{O}_4$  crystallites.
- Undesirable metal-support interactions have been reported to occur to a lesser extent for lower surface area supports compared to supports with higher

surface areas<sup>2</sup>. Performing wet impregnation with a lower surface area silica support may give rise to a greater proportion of  $\text{Co}_3\text{O}_4$  and less silicates.

- To more accurately assess the suitability of the cobalt oxides for use as cold-start abatement catalysts, activity testing should be performed using a mixture representative of exhaust gases:  $\text{NO}_x$ , CO,  $\text{CO}_2$ ,  $\text{H}_2\text{O}$  and oxygen (<20%) are present in gasoline exhaust in addition to hydrocarbons<sup>3</sup>.

### 6.3 References

1. R. J. S. Lima, K. O. Moura, P. P. Pedra, J. G. S. Duque and C. T. Meneses, *Physica B: Condensed Matter*, 2012, **407**, 3196-3198.
2. B. Solsona, T. E. Davies, T. Garcia, I. Vazquez, A. Dejoz and S. H. Taylor, *Appl. Catal. B-Environ.*, 2008, **84**, 176-184.
3. R. Stone, *Introduction to Internal Combustion Engines*, Society of Automotive Engineers, 1999.

# Chapter 7

## Appendix

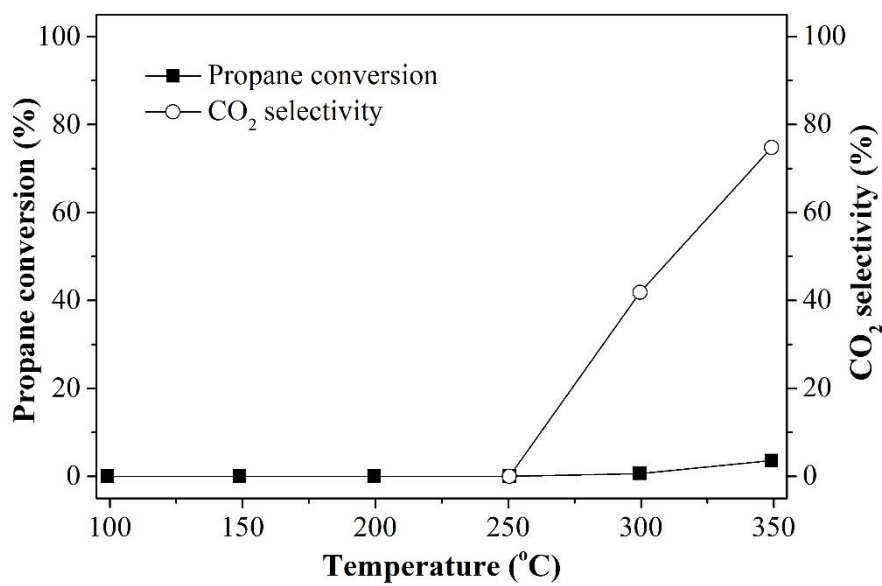


Figure A1 – Propane conversion in reactor tube without catalyst (quartz wool only)